FOCUS

CIVIL ENGINEERING AND GEOMECHANICS SERIES

Electrohydraulic Fracturing of Rocks

Gilles Pijaudier-Cabot, Christian La Borderie
Thierry Reess, Wen Chen, Olivier Maurel
Franck Rey-Bethbeder and Antoine de Ferron

ISTE

WILEY

Table of Contents

List of Illustrations

Electrohydraulic Fracturing of Rocks

Gilles Pijaudier-Cabot

Christian La Borderie

Thierry Reess

Wen Chen

Olivier Maurel

Franck Rey-Berbeder

Antoine de Ferron

FOCUS SERIES

Series Editor Gilles Pijaudier-Cabot

ISTE WILEY

First published 2016 in Great Britain and the United States by ISTE Ltd and John Wiley & Sons, Inc.

ISTE Ltd

27-37 St George's Road

London SW19 4EU

UK

www.iste.co.uk

John Wiley & Sons, Inc.

111 River Street

Hoboken, NJ 07030

USA

www.wiley.com

Library of Congress Control Number: 2015959670

British Library Cataloguing-in-Publication Data

A CIP record for this book is available from the British Library

ISSN 2051-2481 (Print)

ISSN 2051-249X (Online)

ISBN 978-1-84821-710-2

Preface

Early in 2005, Total Exploration Production issued a call in France for "Blue Sky" research proposals dedicated to stimulation techniques for tight gas reservoirs. In such very tight formations, the permeability being in the sub milli-Darcy range, hydraulic fracturing was found to be inefficient. After fracturing, a rapid decay of gas production was observed. The general understanding was – and still is – that in a tight formation, hydraulic fracturing produces drains with high permeability but they are connected to a tight formation. Once gas has been expulsed from the neighborhood of the fracture, the flow decreases dramatically and it is still the tighter part of the formation that controls the production.

Some solutions for circumventing this problem were known, one being to drill closely-spaced wells so that after hydraulic fracture, the neighborhood of the cracks from which gas can be extracted overlap, ensuring that as many hydrocarbons as possible are produced. Obviously, this solution is expensive, since the number of wells to be drilled increases and it is also a bit risky. During hydraulic fracture, we should avoid directly connecting one well to another by a fracture.

Through its call for proposals, Total Exploration Production was looking for alternatives, hoping that they would be more cost-effective than classical hydraulic fracturing.

At that time, only one of the authors of this book was involved in petroleum engineering. Our backgrounds were in electrical, civil and mechanical engineering. It is most probably because of this diversity that we collectively answered this call with a project on electrohydraulic fracturing. It was a mix of our respective backgrounds on pulsed arc electrical discharges (e.g. for material recycling purposes), dynamic analysis of structures, failure of civil engineering structures and assessment of tightness of

nuclear vessels. We felt that one possible answer to the problem would be to generate a dense distribution of connected microcracks in rocks instead of a few large fractures. In other words, we thought that fragmentation of rock was more appropriate than fracture of rocks in such a problem. Dense and connected microcracking was expected to increase the permeability in the volume of the rock, and therefore would be more effective for gas production than a few drains (fractures) in a tight formation.

This proposal received support and enthusiasm from Total Exploration Production and a feasibility study started in 2007, followed after that by more comprehensive research spanning from 2008 to 2012. The research project was placed under the umbrella of the federation of research laboratories dedicated to petroleum engineering at the University of Pau, in connection with the Institute of Civil and Mechanical Engineering at Centrale Nantes. It also received the support from the Région Aquitaine, which helped with a doctoral fellowship and with additional support for the setting up of a comprehensive laboratory facility in Pau and Anglet.

The experimental program was probably the most demanding part of the project, but soon it revealed that our initial idea was correct. Over 300 specimens were tested under various conditions, each one following a specific workflow combining different testing techniques aimed at the characterization of dynamic loading, of the microstructure of the specimens and their permeability. Specimens were carried back and forth between the two sites in Pau and Anglet and also between the Total Exploration Production scientific and technical research center in Pau, where part of the study was performed, and our facilities at the university. Overall, the project involved over 10 people.

With positive results, the limits of the technique also emerged. With the first computations on representative reservoir geometries performed, we soon found that the damage zone around the well was too small because of the attenuation of the pressure waves generated by the electrical

discharges. Therefore, we tried to investigate some optimization directions. There was also the frustration of not being able to carry out *in situ* experiments in order to check the feasibility of electrohydraulic fracturing in a real environment, or at least in a calibration chamber.

This book collects the various results obtained in the course of this project in a single monography. It is based on a compilation of several technical papers published from 2010 to 2015 [MAU 10, CHE 11, CHE 12, CHE 14b, CHE 14a, KHA 15]. The final chapter, however, is entirely original as the results have not been published.

At the time we started this project, unconventional resources, and more specifically shale gas, were not on the front pages of newspapers. Very soon, we thought about the implementation of the electrohydraulic technique to horizontal wells and shale gas production and two international patents were filled [REY 12, REY 12]. In 2011, the debate about the dangers of hydraulic fracturing developed in France, before and after it was banned, and unexpectedly electrohydraulic fracturing came to the forefront of discussions, being considered a potential alternative to hydraulic fracturing.

A lot has been written in the media about the promises of electrohydraulic fracturing, sometimes in a quite optimistic way. The critical approach, which ought to be that of scientists, pushes us to underline the limitations of this new technique, which would not be effective without a complementarity with hydraulic fracturing, as well as its potential provided that additional research and development can be carried out – not so easy a task in the French context. It is also the purpose of this book to collect results together so that readers can develop their own point of view about electrohydraulic fracturing.

Gilles PIJAUDIER-CABOT
December 2015

Introduction

I.1. Context

Hydraulic fracturing is used not only for the production of hydrocarbons, but also for geothermal energy production or fresh water production. It was implemented for the first time in 1947 in Kansas. Two years later, the first commercial fracturing treatments were conducted in oil wells in Oklahoma; but, it was only with the massive exploitation of shale gas, during the last decade, that the process became popular in the media outside the circle of experts. In 2008, over 50,000 well fractures were carried out around the world and it is estimated that over one in every two wells drilled today undergoes a fracturing treatment.

Hydraulic fracturing involves the high pressure injection of a fluid in a wellbore, at a specified depth. When the pressure applied by the fluid is greater than the lithostatic gradient (weight of the rock above the place where the pressure is applied) and the local resistance of the rock, a fracture is created that can extend over several hundred meters, provided that enough fluid is injected to maintain a sufficient pressure. During the process, a *proppant* (generally grains of sand or ceramic) is injected to prevent the crack from closing. Drilling water contains additives suited to the type of rock encountered, to facilitate the fracturing operation and to prevent the closure of the cracks created. These cracks act as drains, granting access to volumes of rock located a long way from the wellbore, but close enough to the created drain.

Hydraulic fracturing was first applied to conventional geological reservoirs. However, its use in low-permeability formations called tight gas reservoirs (TGRs), which are a thousand times less permeable than conventional reservoirs, has meant overcoming severe problems. Tight gas reservoirs and shale gas reservoirs contain gas mainly, stored in low-permeability rocks (0.1 mD). Hydraulic

fracturing generates a few large cracks and gas may migrate toward these cracks and bubbles be produced. The extracted gas originates from a volume of rock near the surface of the fracture, through which the gas migrates due to the difference in pressure. Gas production consists of draining this zone where permeability is low. The gas trapped between the drained areas remains inaccessible. Once drainage is carried out, the production undergoes a very rapid decline.

The questions raised by hydraulic fracturing in the context of unconventional resources concern several issues. First, the rise of methane to the ground surface or to water tables has fueled public debate, although the extent of the phenomenon is still being discussed. The second issue concerns the water used during the fracturing process. It contains chemical elements that have been used for the fracturing process or dissolved from the underground host rock. This water ought to be stored safely on the surface and subsequently treated. Third, hydraulic fracturing may induce seismicity. The injection of water has reactivated existing faults in some cases in Switzerland and Great Britain. Finally, and probably more importantly, extracting gas with a sufficiently attractive economical benefit calls for a large number of wells that are closely spaced, and thus for a concentration of infrastructures within a dense logistic network is required to provide water and drilling equipment. Therefore, the environmental impact may be severe, particularly in protected or densely inhabited areas.

Under these circumstances and while waiting for the necessary feedback from experience, some European countries have banned hydraulic fracturing, opening the path to research on potential alternatives.

A first option is to change the fracturing fluid. The penetration of the fracturing fluid in the porous host rock depends directly on its viscosity. By reducing this parameter, the fluids more easily penetrate the porous rock and then if we apply enough pressure, induce a dense crack system. This principle being set, the problem resolves around finding the “right” fluid. There are many candidates

such as propane, nitrogen, carbon dioxide, etc. In its liquid state, carbon dioxide has a viscosity 10 times lower than water; in the supercritical state (normal conditions of deposit), its viscosity is even lower. Each solution has benefits, beyond the simple fact that the fracturing fluid is no longer water and that, strictly speaking, we can no longer call it "hydraulic fracturing". Nitrogen is not harmful for the environment, and using carbon dioxide can help store it at the same time. There are also disadvantages: replacement fluids are more compressible than water, which makes the process less efficient; carbon dioxide can recombine with water and form a corrosive acid that may corrode the surrounding carbonate rocks.

The second approach is dynamic loading. In statics, the surface of a crack created in a material is proportional to the energy transferred to the volume of material that will break. Dynamic loading, however, forces, a large amount of energy into a small volume of material. In this volume, and because there is such a large amount of energy, a large area of cracks will be created, inducing a dense fracture network. As the loading wave spreads inside the material, it will therefore cause fragmentation, thereby connecting the initial and newly-created network of cracks. In quasi-brittle materials such as rocks, damage generated by dynamic loads results in distributed microcracking compared to damage generated by static loads, which is localized and consists of large cracks. On the basis of this observation, the objective is to use dynamic loads to generate distributed damage around a borehole, i.e. dense microcracking which should subsequently increase the rock permeability [CAO 01a, CAO 01b, DEN 02].

Dynamic loading can be induced, for example, by explosives placed in the wells. There is another possibility, on which we will focus in this book: dynamic loads generated by pulsed arc electrohydraulic discharges (PAEDs).

I.2. Principle of the technique and illustrative experiments

There is considerable interest in the use of PAEDs in engineering practice. They can be used for several purposes, for instance treating water to remove organic chemical impurities, as acoustic sources in medical or sonar applications, selective separation of solids or plasma blasting in the mining industry. In plasma blasting, there are two different technologies: the first one consists of placing the electrodes directly on the rock. The electrical arc is generated inside the rock. It produces a spall and drilling consists of generating successive spalls. The second technology involves generating the electrical arc in a liquid. The electrical discharge induces a shock wave, which is subsequently transmitted to the rock.

As we will see in the following chapters, the load applied to the rock in the proximity of the drilling site is a pressure wave generated by an electrical discharge between two electrodes placed in a wellbore filled with water. The amplitude of this pressure wave can reach up to 200 MPa, while its duration is about 100 microseconds. This pressure wave is transmitted to the rock by the fluid inside the wellbore, and creates microcracks of decreasing density with increasing the distance from the well.

In order to study the feasibility of PAEDs for fracturing rocks, preliminary experiments have been carried out [MAU 10]. The objective was to investigate the experimental correlation between cracking and damage due to a compression shock wave with the intrinsic permeability of the material and with its microstructure characteristics. The wave was generated under water and then transmitted to a cylindrical specimen 100 mm diameter and 125 mm in height (see Figure I.1). The amplitude of the compressive shock wave was prescribed by the amount of energy that is involved in the PAED. Microcracking and compression damage were due to local extensions induced by the Poisson's effect developed in the course of loading. Single and repeated shocks were considered.

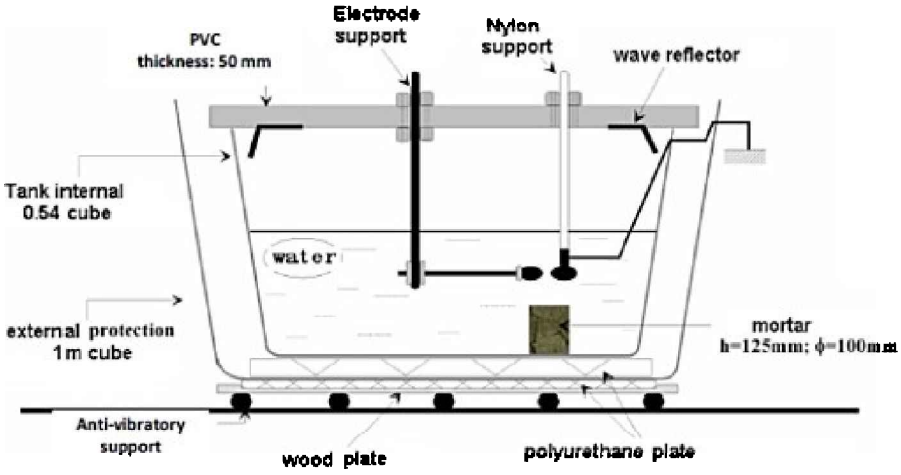

Figure I.1. *Experimental set-up for PAED on mortar samples*

Then, the cylindrical specimens tested in the above apparatus were cut into disks that were 50 mm thick and their permeability to nitrogen was measured (flow in the axial direction). The intrinsic permeability of the specimen was obtained according to Klinkenberg's model which relates the apparent gas permeability of the material to its intrinsic permeability and to the inverse of the gas pressure [KLI 41]:

$$K_a = K\left(1+\frac{\beta}{P}\right) \qquad [I.1]$$

where (K, K_a) are the intrinsic and the apparent permeability, respectively.

Two sequences of tests have been carried out. In the first one, the specimens were subjected to a single shock wave under variable pressure levels. The peak pressure ranged from 0 to 250 MPa (0, 15, 30, 45; 60 90, 180 and 250 MPa). The variation of the intrinsic permeability with the peak pressure is shown in Figure I.2. Two distinct zones were observed. If the peak pressure was below 90 MPa, no significant change in permeability was observed. The experimental data in this range spaned from 2.10^{-17} to 6.

10^{-17} m^2, which was a rather usual scattered for the intrinsic permeability of mortar measured on various samples of the same mix. Then, permeability increased almost linearly in a semi-log plot when the peak pressure increased from 90 to 250 MPa.

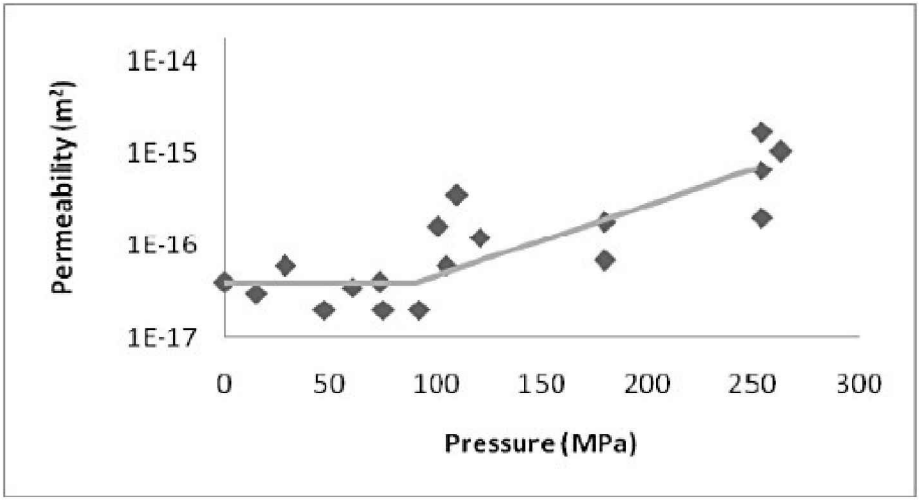

Figure I.2. *Evolution of the permeability with applied pressure*

In the second sequence, the specimens were subjected to repeated shocks at a constant pressure level, equal to 90 MPa. The number of shock waves applied on a single specimen varied from 1 to 10. The test results are shown in Figure I.3. The permeability increased with the number of shocks. This increase spaned over an order of magnitude, which is above the scattering of data. Above eight shocks, some specimens exhibited macrocracks and it was not possible to measure the overall permeability as it was above the range of measurement of our apparatus. The out-coming fluid flow was outside the range of the flow-meters used. The data point for 10 shocks is probably an underestimation of the average permeability (since it is much higher when the specimen is cracked).

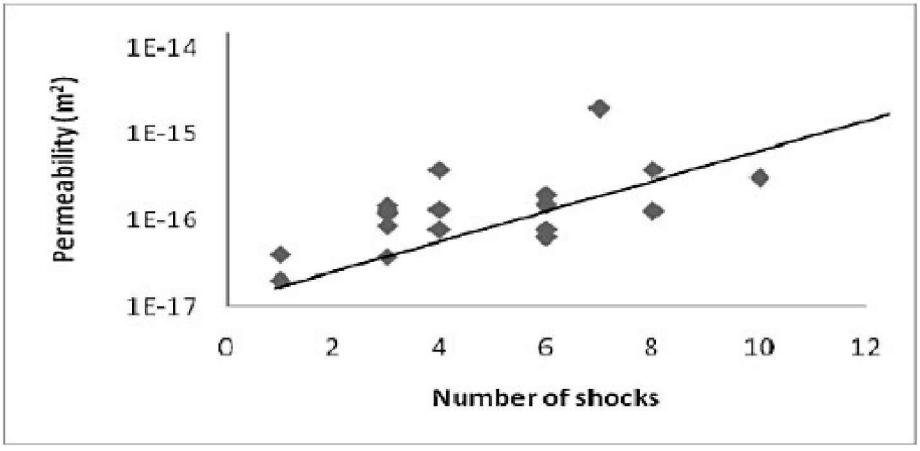

Figure I.3. *Evolution of permeability with the number of shocks, under a peak pressure equal to 90 MPa*

These data clearly show that the foreseen principles of electrohydraulic fracturing are correct and that the technique deserves some close scrutiny. In the following chapters, we are going to investigate electrohydraulic fracturing. In Chapter 1, we will start with the description of experiments that are more representative of the actual state of stress of typical formations containing gas, and of the process used in order to produce the electrical discharge. Chapter 2 will be devoted to the theoretical and numerical modeling of the process. In Chapter 3, we will perform the calculations of the experiments and examine the validity of the computational model. Chapter 4 is devoted to computations on representative configurations and directions for the optimization of the process.

Most of the work performed in the following relies on experiments performed on model materials designed in order to mimic tight rocks. A cement-based mortar has been developed for this purpose, with elastic and hydraulic development that are quite similar to tight rocks. The development of this mortar was indeed necessary in view of the large number of experiments, which were performed prior to achieving a reliable testing procedure, and also to obtain first experimental data on which theoretical models were developed and validated.

1
Experiments in a Representative Environment

The experimental program presented in this chapter included several distinct phases:

– mechanical experiments in which specimens were subjected to representative confinement stresses and to pulsed arc electrohydraulic discharges (PAEDs);

– permeability tests performed before and after the mechanical experiments in order to quantify the increase in permeability upon electrohydraulic fracturing;

– X-ray scanning tomography before and after the mechanical experiments in order to visualize the crack network generated by the mechanical loads.

We are going to detail the experiments and discuss the results obtained on a model material (mortar), and on sandstone.

1.1. Mechanical set-up

Our aim is to design experiments that implement conditions that are that are as close as possible to real ones.

It means that specimens ought to be subjected to the triaxial confinement experienced underground at several different depths, and that the pulse applied should be generated in a specimen geometry that is close to a real well bore.

The shock wave is generated in a hollow cylinder (mortar or rock) filled with water. The radial confinement pressure is applied with three stacked steel rings (600 mm in diameter, 60 mm in height and 30 mm thick) tightened with the help of a beam wrench. The steel rings were equipped with strain gauges to check the confining pressure during the tightening phase. Three confining blocks made of ultra high-

performance concrete reinforced with metallic fibers are placed between the specimen and the steel rings in order to absorb the shock wave and to homogenize the radial pressure on the external face of the specimen. The high-performance concrete used to confine the specimen has approximately the same dynamic impedance characteristics as the specimen in order to avoid wave reflections at the boundary. This set-up is shown in Figure 1.1.

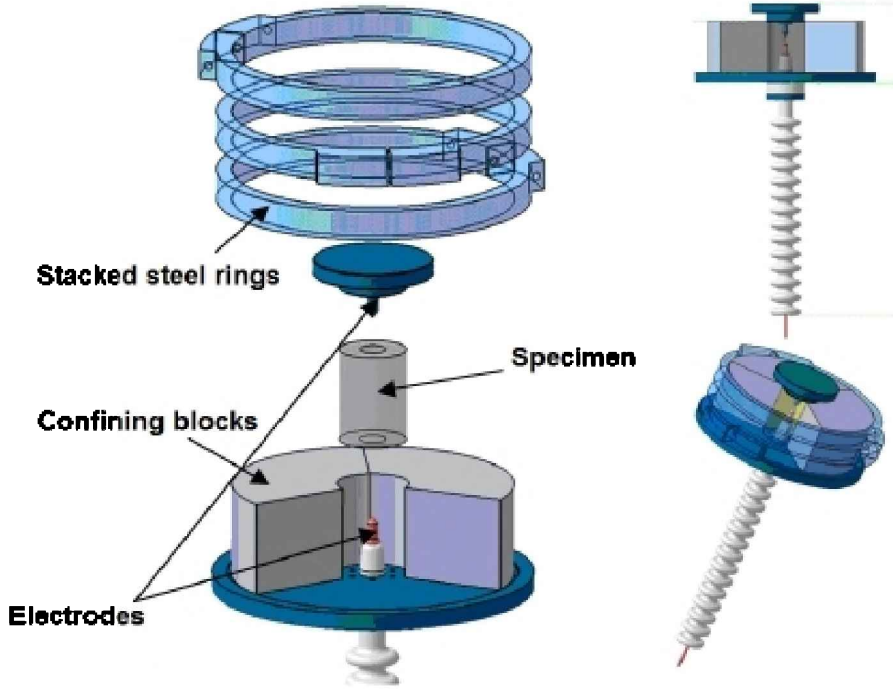

Figure 1.1. *Overall view of the triaxial cell*

The vertical load is applied with a 2,000 kN hydraulic jack (Figure 1.2), which is placed in a protected environment with respect to electromagnetic radiations and electrical surges.

Figure 1.2. *Hydraulic frame hosting the triaxial cell*

Due to the radiations generated by the electrical discharges, it was not possible to use the displaced transducers or electronic equipment for load control or resistive gauge measurements. For this reason, the frame is a pneumatic one, the confinement is applied in a passive way and no transducers were able to be placed in order to record loads or deformations.

Specimens are confined according to three levels of radial stresses and vertical loads corresponding to three depths: low confinement (depth = 0 m), medium confinement (depth equal to 1,500 m and Biot factor equal to 1) and high confinement (depth equal to 2,250 m and Biot factor equal to 0.5 or depth equal to 3,000 m and Biot factor equal to 1). Vertical and lateral stresses are detailed in Table 1.1.

Table 1.1. *Vertical and lateral stresses of the mortar*

	Vertical loads (MPa)	Lateral stresses (MPa)	Depth (m)
Low confinement	2	2	0
Medium confinement	19.5	9.1	1,500
High confinement	40	25	2,250

1.2. Pulsed arc electric generator

The electrodes are placed inside the hollow part of the specimen which is immersed in water (Figure I.1). The electrodes are made up of two vertical cylindrical tubes, on the lower ends of which are screwed two stainless steel electrodes (5 mm diameter). The gap between the two electrodes is equal to 5 mm. The positive impulse voltage is obtained by charging storage capacitors in the C = 300 nF to 21 μF range, depending on the electrical energy to be released during the electric discharge. A triggered spark-gap allows the switching of energy of up to 20 kJ in water. The maximum charging voltage of the capacitors is 40 kV. The voltage impulse and the current are monitored with a North Star probe (100 kV–90 MHz) and a Pearson current monitor (50 kA–4 MHz), respectively.

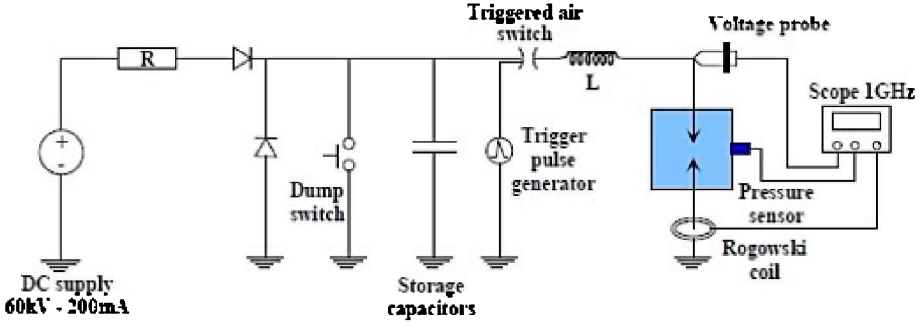

Figure 1.3. *Experimental set-up – electrical part*

Figure 1.3 shows the schematic organization of the electrical

set-up. During the tests, the pressure sensor is removed. It is used for the calibration of the energy–pressure relationship only. According to previous investigations [TOU 06], the dynamic pressures generated by subsonic water discharges present in bi-exponential form and are characterized by a rise time of about 500 ns and a pulse width of a few microseconds. The associated frequency spectrum reaches 200 kHz at –20 dB.

The general form of the pressure pulse applied can be written using the following relationship:

$$P(t) = P_0\left[e^{-at} - e^{-bt}\right] \qquad [1.1]$$

where P is the pressure at time t, P_O denotes the peak pressure value and a and b are the constants in our experimental conditions. Previous works [TOU 06] have pointed out that the peak pressure P_O the depends on the energy E_B remaining at breakdown time (point at which liquid water in between the electrodes breaks down) and can be approximated by:

$$P_0 = \frac{k}{d}\left(\frac{E_B}{E}\right)^{\alpha} \qquad [1.2]$$

where $E_B = 1/2.C.U_B^2$. U_B is the breakdown voltage value, C is the storage capacity, $_k$, α and E are the parameters that depend on the interelectrode geometry and d is the distance between the specimen and the plasma channel. In the same experimental conditions (where the distance between the electrodes is 5 mm, and the radius of the electrodes is 15 mm), Touya has shown that $\alpha = 0.35$ and $k = 9000 / d$. Thus, it is possible to control the peak pressure value P_O applied to mortar specimens using the following relation:

$$P_0 = \frac{9000}{d}.E_B^{0.35} \qquad [1.3]$$

with P_O in bar, E_B in kJ and d in mm. Consequently, the applied peak pressure can be adjusted by changing the value of the remaining energy E_B or by modifying the charging voltage and capacity.

1.3 Material properties

The specimens are hollow cylinders with internal diameter, external diameter and height equal to 50, 125, and 180 mm, respectively, as shown in Figure 1.4. Two materials have been considered: mortar and sandstone.

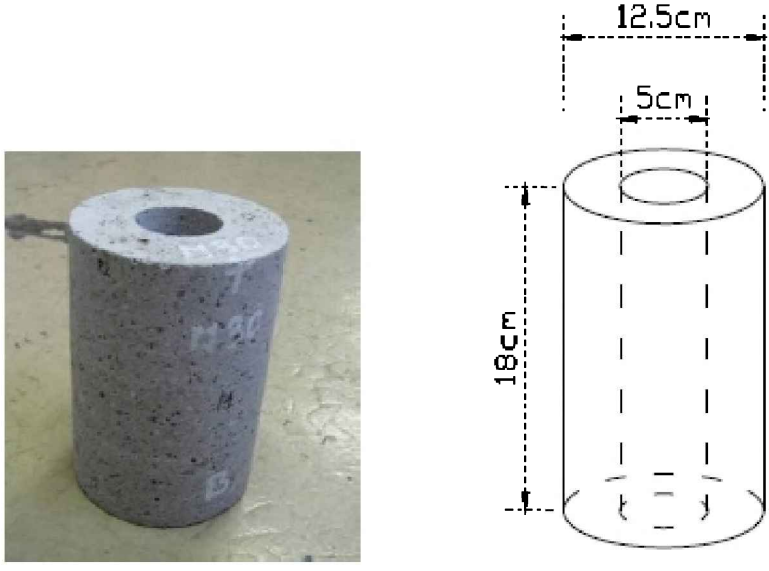

Figure 1.4. *Specimen characteristics*

For the cement-based specimens, mortar was made with a maximal grain size of 2 mm and with a water-to-cement ratio equal to 0.6. It is a model material designed in such a way that its initial permeability is close to that of tight rocks. The properties of this mortar are given in Table 1.2. Sandstone specimens were machined to the same geometry as mortar ones. Mortar specimens are machined too in order to avoid the effects of segregation that naturally exist at the mould boundaries.

Table 1.2. *Average mechanical properties of mortar and sandstone*

	f_c (MPa)	f_t (MPa)	E (MPa)	K_v (m^2)
Mortar	19.6	4.9	17,300	4. $10^{-}17$
Molière sandstone	49	6.35	19,000	1.$10^{-}17$ to 2.10^{-} 16

1.4. Measurements of radial permeability

Radial permeability tests are performed in isothermal (ambient) conditions. An inert gas (nitrogen) is injected into the cylindrical borehole through a perforated bottom platen and flows radially through the specimen (Figure 1.5). In order to achieve radial flow of the gas, the top and bottom faces of the cylindrical specimen are covered with an aluminum foil and with silicone grease in order to prevent leakage. In addition, the platens placed on the upper and lower faces have two cylindrical rubber joints. The measurement of the intrinsic permeability of mortar is performed at 20°C, under an axial compressive load of 4 kN, resulting in the compressive stress of 0.4 MPa, a negligible stress for such a specimen. This load ensures contact between the specimen and the load platens, and therefore the tightness of the permeability cell. A relative pressure ΔP (difference between the injection pressure P_i and the atmospheric pressure P_{atm}) is applied and maintained until gas flow is stationary. The relative pressure and mass flow rate are measured upstream of the specimen with a set of mass flow meters that converts the mass flow rate into an equivalent volumetric gas flow rate. Each flow meter has a different range, starting from 10–150 ml/min, via 50–1,500 ml/min, to 300–15,000 ml/min, allowing us to scan intrinsic permeabilities from $10^{-18}$to 10^{-10} m^2.

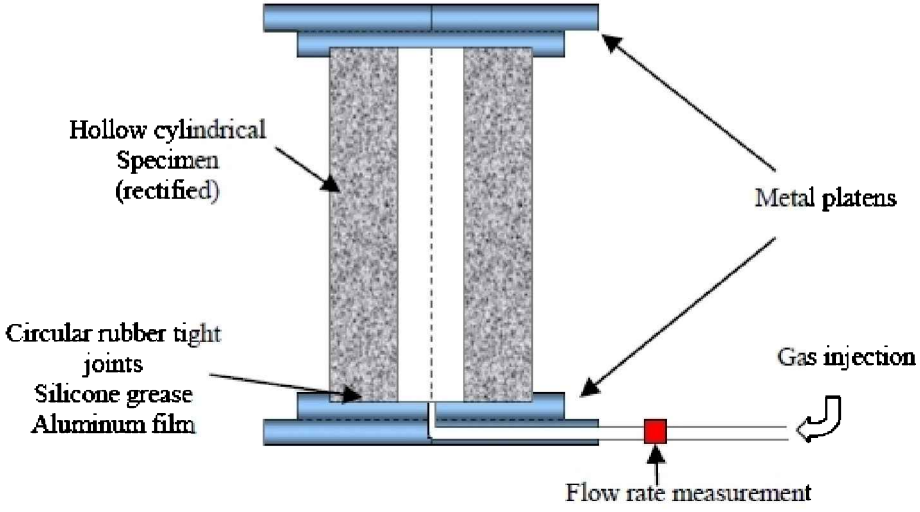

Figure 1.5. *Schematic representation of the permeability cell*

Darcy's law and mass balance equation enable an apparent permeability K_a [m^2] to be calculated from the injection flow rate Q_i [m^3/s]:

$$k_a = \frac{Q_i \cdot P_i \cdot \mu \cdot \ln\left(\frac{r2}{r1}\right)}{\pi \cdot h \cdot \left(P_i^2 - P_{atm}^2\right)} \qquad [1.4]$$

where μ [Pa.s] is the dynamic viscosity of the inert gas used (nitrogen) and r_1 [m], r_2 [m], and h [m] are the inner radius, outer radius and the height of the cylindrical specimen, respectively.

This permeability is relative to the overall gas flow through the material, consisting of the viscous flow and the slip flow. Viscous flow corresponds to the classical laminar configuration. The slip flow appears when the average diameter of the pores is the size of the mean free path of the gas molecules (average distance between collisions). In this case, there is an interaction between the gas and the pore walls that cannot be neglected.

In order to obtain the intrinsic permeability related to

viscous laminar flow, a characteristic of the sole porous medium, the relationship due to the Klinkenberg model is used, as in the experiments reported in the introduction (equation [I.1]). The intrinsic permeability K [m^2] is obtained by extrapolating the apparent gas permeability measured at various pressures to the case of infinite pressure. The measurements of the apparent permeability are performed for five relative pressures: 0.3, 0.25, 0.20, 0.15 and 0.10 MPa. The accuracy of measurement of the apparent permeability is approximately 2%. The permeability is measured on each specimen prior to mechanical testing and serves as a reference value in forthcoming comparisons.

The permeability after mechanical testing was measured without confinement stresses and also checked on representative specimens with confinement stresses applied. As expected, the permeability measured under confinement was lower than the one measured without confinement. The ratio between permeability measured under medium confinement and without confinement is approximately equal to one order of magnitude. We will see that the variation of permeability due to electrohydraulic fracturing is much larger than that.

1.5. X-ray tomography

Each specimen was scanned in an X-ray tomography facility prior to and after testing. The specimens were marked so that the three-dimensional (3D) images could be superimposed and then relative permanent displacements between the two images could be recovered. These residual displacements are due to cracks that stay open after testing. The technique is such that residual crack opening of a few tenths of a micron can be obtained from images with an accuracy of 250 μm corresponding to a medical X-ray tomographic device.

1.6. Results on model materials

Two sequences of tests have been carried out. In the first one, the mortar specimens were subjected to a single shock under a variable injected electrical energy, for each of the three confinement levels considered. For the tests under low confinement, the injected electrical energy ranges up to 680 J; for the tests under medium confinement, it ranged up to 1.15 kJ and the injected energy reached 17 kJ in the tests under high confinement.

In the second sequence, the specimens were subjected to repeated shocks (up to nine shocks) with a constant injected energy. Note that the time between each shock is in the order of several minutes in order to avoid any possible effects relating to fatigue.

1.6.1. *Influence of injected electrical energy on permeability*

The variation of intrinsic permeability of mortar specimens with injected electrical energy E_B at different confinement levels is shown in Figure 1.6.

If the injected electrical energy is below a threshold, the intrinsic permeability does not increase regardless of the level of confinement. This threshold increases with increased confinement. Permeability sharply increases with the injected energy.

When the permeability became greater than 1.00 10–14 m^2, it was not possible to measure it. Specimens were so damaged that macrocracks were observed throughout the thickness of the hollow cylinders, resulting in a very large apparent permeability that could not be measured accurately with our equipment.

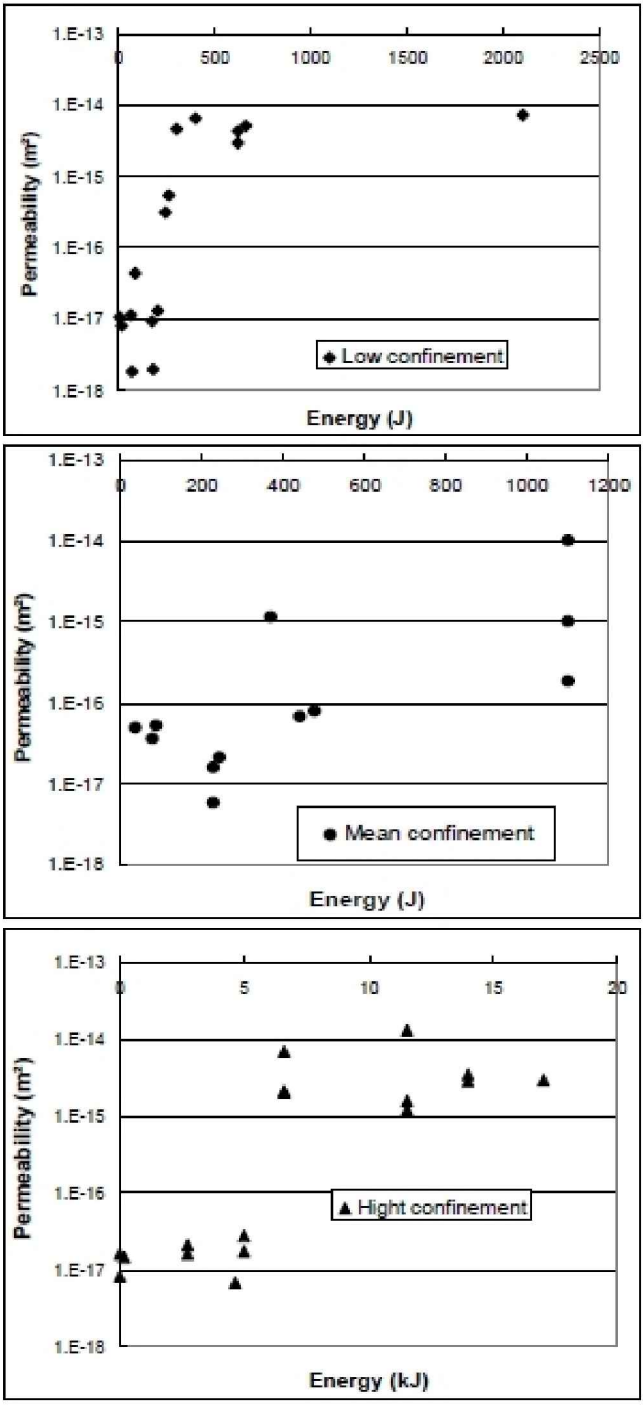

Figure 1.6. *Evolution of following a permeability with injected electrical energy, single shock on mortar specimens*

Under low confinement, a damage threshold of 190 J characterizes the onset of microcrack propagation. When the injected energy is below this threshold, microcracks do not develop; when the injected energy is greater than this threshold, microcracks with an opening in the range of 0.02 mm are observed. This phenomenon will be illustrated with tomography X-Ray scans later. Under medium and high confinements, the same trend is observed, with different damaging energy thresholds of 500 J and 5.11 kJ, respectively.

1.6.2. *Influence of the number of shocks on permeability*

Tests with repeated shocks have been performed in the case of high confinement only.

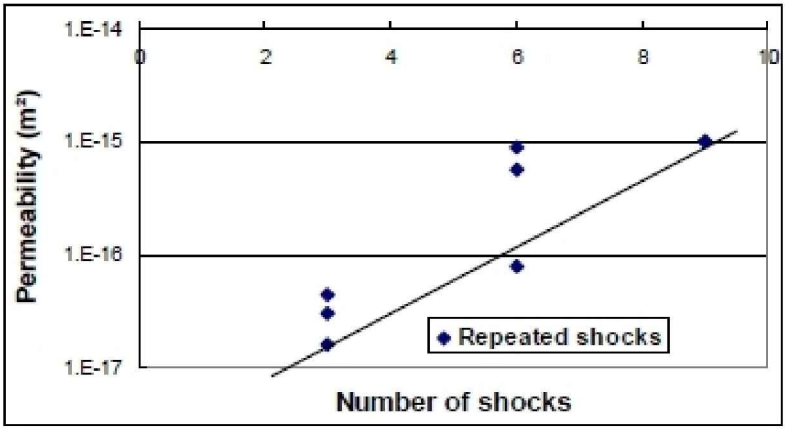

Figure 1.7. *Evolution of the permeability of mortar specimens with the number of shocks, under an injected energy equal to 2.7 kJ and high confinement*

The tests were carried out with two energy levels. The first level corresponded to 60% of the threshold of damage. Sixty and 90% shocks were applied. No significant changes in permeability were observed. This energy level was too low to damage the material significantly. The second energy level was at 85% of the threshold of damage. The number of shocks applied on each specimen ranged from 3 to 6 and 9 shocks.

The test results are shown in Figure 1.7. In a semi-log plot, the permeability increases almost linearly with the number of shocks. This increase spans over a range of almost two orders of magnitude, which is above the scattering of data.

1.6.3. *X-ray scans*

The correlations between the dynamic load applied on the specimens, their microstructure, material damage and the permeability can be visualized qualitatively with X-ray tomography. Figure 1.8 shows an example of the cross-section after scanning the specimen before and after shock, and the difference between the two scans. The level of gray varies linearly with the material density. White zones are related to pores and cracks. The resolution of the scan is approximately 0.25 mm. Taking the difference between the two scans provides an increase in resolution to about 0.02 mm. Large cracks with opening above 0.02 mm can be observed only. The darkest zones in the specimen represent the virgin material with density close to 2.5 kg/dm^3.

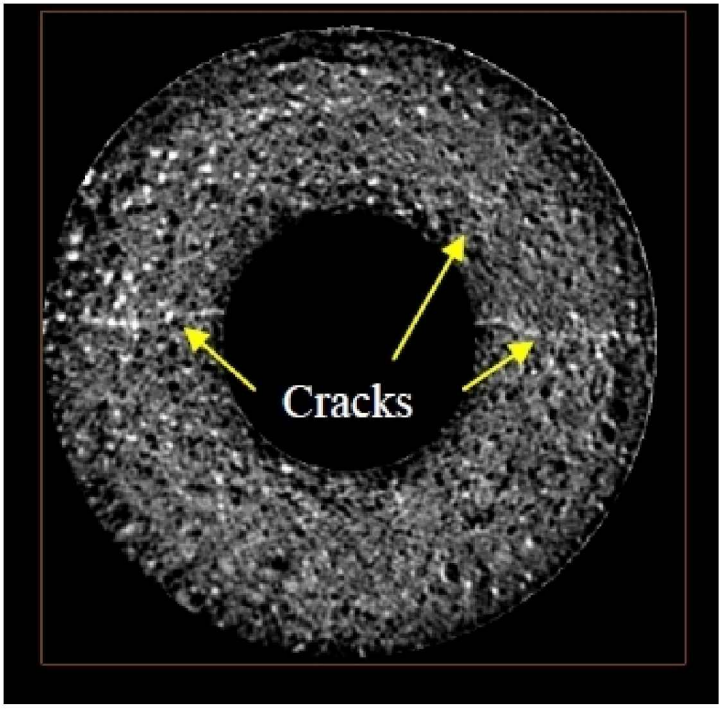

Figure 1.8. *Cross-section after computed tomography scanning of a mortar specimen*

Three-dimensional scans are shown in Figures 1.9 and 1.10. In these photos, the dark zones show macrocracks with an opening greater than 0.02 mm. Figure 1.9 shows the effect of the level of electrical energy injected in the case of high confinement.

Quantitatively, the crack surface area generated may be used to analyze the effectiveness of the process. The specimens denoted as M08, T03 and M11 in Figure 1.9 had fracture surfaces of 63 cm^2, 439 cm^2 and 351 cm^2, respectively. This evolution correlates quite well with the specimens' evolution of permeability. Nevertheless, without a complete statistical analysis, which was not performed in the present study in view of the limited number of tests for each energy and confinement configuration, no robust quantitative correlation can be determined. Scans also show that several macrocracks had developed, which is at variance with a static (e.g. hydraulic-driven) process in which only a single macrocrack would propagate.

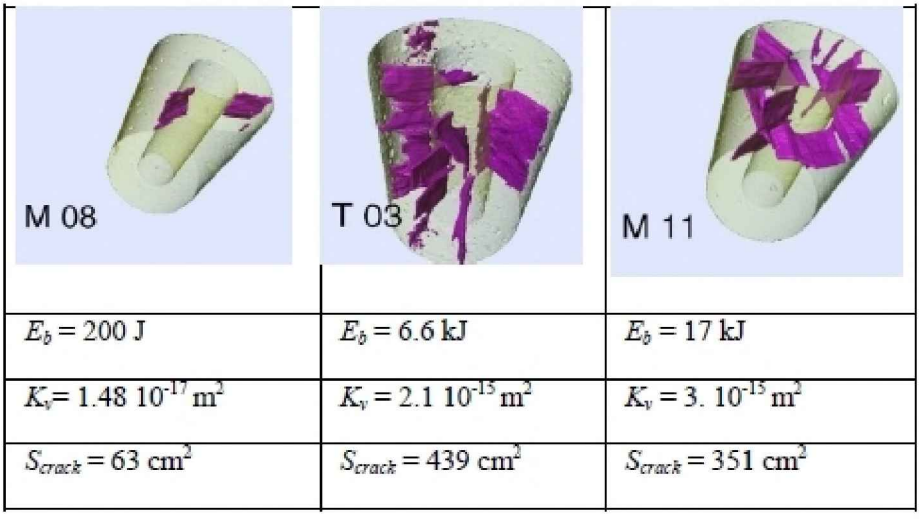

Figure 1.9. *Three-dimensional tomography scans after one shock under high confinement. For a color version of the figure, see www.iste.co.uk/pijaudier/drystone.zip*

Figure 1.10 shows the effect of the number of repeated shocks with injected electrical energy equal to 2.7 kJ on the generation of macrocracks under high confinement. After three shocks cracking slightly evolves, with a crack surface equal to 26 cm^2. Macrocracking occurs inside the specimen after six shocks, and the crack surface increases to 238.5 cm^2. After nine shocks, severe cracking is observed and the crack surface is increased to 326.5 cm^2.

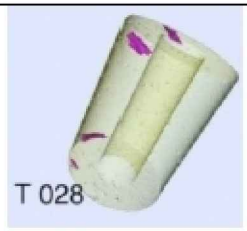	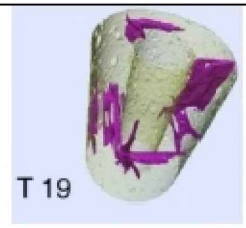	
$E_b = 2.7$ kJ	$E_b = 2.7$ kJ	$E_b = 2.7$ kJ
3 shocks	6 shocks	9 shocks
$K_v = 3.01\ 10^{-17}$ m^2	$K_v = 5.64\ 10^{-16}$ m^2	$K_v = 1.\ 10^{-15}$ m^2
$S_{crack} = 26$ cm^2	$S_{crack} = 238.5$ cm^2	$S_{crack} = 326.5$ cm^2

Figure 1.10. *Three-dimensional tomography scans after one shock (left), three shocks (middle) and nine shocks (right). Tests under high confinement. For a color version of the figure, see www.iste.co.uk/pijaudier/drystone.zip*

1.6.4. *Evolution of the pore size distribution*

On top of the development of cracking, the electrohydraulic shocks also affect the pore size distribution of the material. The above study has been complemented with additional measurements of the evolution of the pore size distribution of small specimens cored in the permeability specimens in order to determine whether there were any correlations. Mercury intrusion porosimetry has been used for this purpose. It is a routine technique with some drawbacks:

– It only characterizes the connected porosity which is accessible from the outer surface of the specimen. We do not intend, however, to consider the entire pore population, but rather the connected porous space that is at stake in the gas transfer process governing permeability. This drawback is therefore not important to us.

– The analysis is based on the assumption that pores are cylindrical with monotonically decreasing radius as mercury is injected into the specimen. The “ink bottle effect” [DIA 00] may be important, i.e. small pores connected to large pores in the direction of the flow of mercury. This is avoided by performing several cycles of

injection (upon cycles, mercury in such large pores remains trapped and is no longer accounted for in the calculation of pore size distribution).

– Finally, mercury intrusion porosimetry is destructive. For large pressures where small pores in the order of 10 nanometers or less become accessible, the issue of breakage of the pore walls may arise. This is the reason why the pore size distribution is restricted to the range between 20 and 30 nanometers and several micrometers.

The sample preparation consisted of coring, sawing and curing (24 h at 80°C) each specimen from larger specimens that had been subjected to electrical shock fracturing before and whose permeability had been already measured. Only specimens with high confinement corresponding to the data on permeability showed in Figure 1.6 are considered [KHA 15].

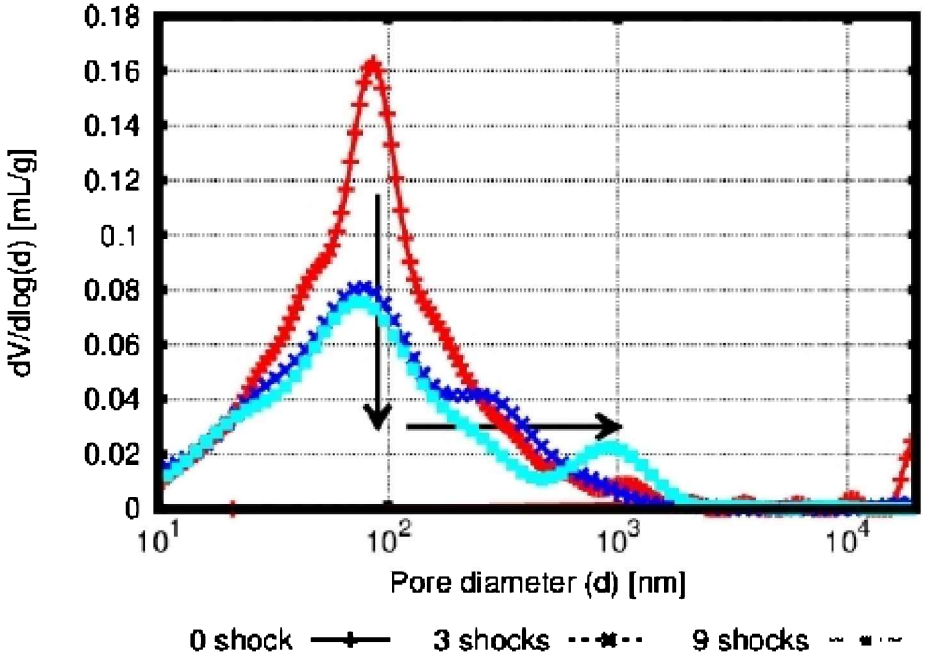

Figure 1.11. *Evolution of pore size distribution with the number of shocks. For a color version of the figure, see www.iste.co.uk/pijaudier/drystone.zip*

Three cylindrical samples for each specimen tested

mechanically (8 mm in diameter and 10 mm in height) were prepared. The pore size distributions were further averaged. Figure 1.11 shows how the pore size distribution of the material evolved upon mechanical damage due to 0, 3 and 9 electrical shocks. The fraction of small pores (diameter of 100 nm) decreased, as did the fraction of larger pores (diameter of 500 nm). This effect was clearly related to the increase in permeability, on which large pores have a predominant influence.

1.7. Summary of the results on sandstone

Single shock tests were carried out under high confinement and with injected electrical energy of up to 14 kJ. The permeability of each specimen was measured before and after each test and is shown in Figure 1.12. Again, two distinct zones were observed. If the injected energy was below 4.2 kJ, no significant difference in permeability was observed. Then, the permeability increased almost linearly in a semi-log plot when the injected energy E_b increased from 4.2 to 14 kJ. This growth in permeability with injected electrical energy followed the same trend as for the mortar specimens.

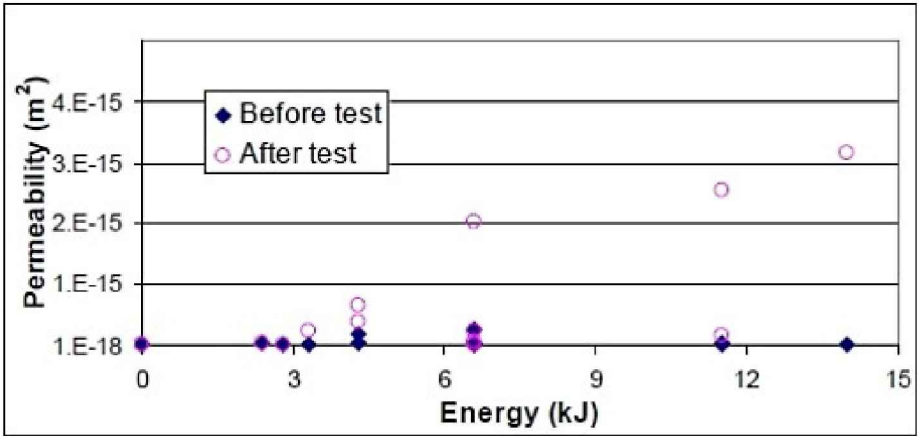

Figure 1.12. *Evolution of the permeability of sandstone specimens with injected energy before and after the shock test*

For the tests under repeated shocks, high confinement was

also considered. The number of shocks varied from 2 to 8 (2, 3, 4, 5, 6 and 8 shocks) under a constant injected energy equal to 2.2 kJ. This energy corresponded to 80% of the energy injected at the onset of damage. The time delay between two shocks was long enough to avoid interaction between shock waves. The relative increase in the permeability of each specimen with the number of shocks is shown in Figure 1.12. If the number of shocks was less than 4, no significant changes were observed in the permeability. If the number of shocks was above 4, the relative variation in permeability increased almost linearly with number of shocks, which is the same as for the mortar specimens.

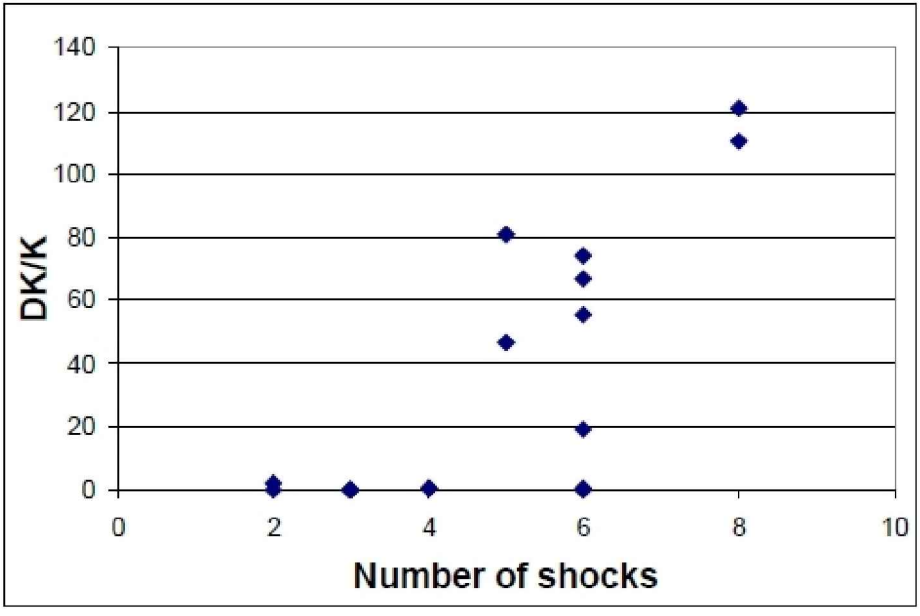

Figure 1.13. *Evolution of the ratio of the permeability of sandstone specimens with the number of shocks, under an injected energy equal to 2.2 kJ and high confinement*

1.8. Discussion

For both mortar and sandstone specimens, similar trends are observed. Above an energy threshold, test data on a single shock reveal a significant increase in permeability whatever the confinement applied on the specimen. The fact that the load level should be increased in order to reach the

fracture threshold with increasing confinement is a very classical result according to fracture mechanics analyses of hydraulic cracking [PAP 06, CHA 91].

As mentioned by Lopez and Jimeno [LOP 95], the pressure wave created by the blasting induces intense radial compression in the material, along with a tangent tensile stress. The radial fracturing of the specimen is obtained when the tangent stress exceeds the dynamic strength of the material. It is this radial fracturing which is at the origin of the increase in permeability. The experimental cracking patterns (vertical cracks), illustrated by X-ray scans, are in good agreement with existing numerical results in the literature [WAN 09].

The results obtained for repeated loads may also be compared with those obtained by Sanchidirian *et al.* [SAN 07] who measured an increase in damage of approximately 50% in rocks after 33 repeated blast rounds. Even if the damage created by a single shock cannot be measured in terms of permeability, the pore size distribution of the material should be affected by the loading. Note that there is also an endurance level below which microcracking never occurs, which is the same as in fatigue (see [CHK 09, BAZ 98]).

Finally, the increase in permeability due to microcracking is consistent with the data in the literature, e.g. on concrete specimens with a similar geometry [CHO 07]. This similarity is going to guide us in the development of theoretical models that should be able to provide a numerical simulation of the electrohydraulic fracture process.

2
Computational Modeling of the Process: Principles

In this chapter, we are going to describe the various ingredients that will be put together in order to achieve numerical simulations of the electrohydraulic fracturing process in the context of hydrocarbon production. Three items will be discussed, as they require special attention:

– the theoretical model from which the pressure generated by the pulsed area electric discharge (PAED) can be derived;

– the mechanical modeling of the material under dynamic loads;

– the coupled effects between the growth of damage due to microfracturing and the growth of permeability.

These models have been folded into a single computer code, EUROPLEXUS co-developed by the Combustion Engineering Association (CEN Saclay, DMT) and the European Commission (JRC-Ispra and the Institute of Systems Information and Safety) since 1999. This code is based on the finite element method and uses an explicit time integration algorithm [ROB 03, ROB 04, ROB 05]. At each time step, the conservation of mass, the conservation of energy, the constitutive laws and the conservation of momentum are computed successively. The entire set-up (fluid and solid) is modeled with a single finite element mesh and an arbitrary Lagrangien Eulerian (ALE) description is implemented in order to achieve a proper description of the fluid solid interface [CAS 04].

Damping is very important in such simulations. Damping is introduced in order to attenuate high-frequency oscillations generated by the discretization. On the other side, damping should not attenuate the pressure waves, and therefore

should be as small as possible. A quadratic damping function has been used with two parameters: the reduced damping coefficient for high frequencies, which is equal to zero by default and should always be very small (<0.05); a constant for the quadratic damping which is adapted in the computation of shockwaves. In the following calculation, the reduced damping coefficient is equal to 0.005 and the constant varies from 8 to 12 in order to keep the computation stable. We have checked that it has little effect on the results of the computations.

2.1. Pressure generated by the pulsed arc electrical discharge

The simulation of shockwave generation in water by electrical discharges has been the subject of several studies over recent years, in the context of the safety of sodium –water nuclear reactors. For instance, Madhavan *et al.* [MAD 05] performed one-dimensional and two-dimensional hydrodynamic simulations for studying shock production in water. Here, a simplified model is developed, which is capable of providing a correct characterization of shockwave propagation in water. The hydrodynamic pressure wave results from the rapid injection of energy into water, as an augmentation of enthalpy: high-pressure bubbles are formed and expand very quickly. This motion of the boundaries between the liquid and the gas phase at high velocity generates the wave.

The underwater electrical discharge is assumed to occur within a two-phase mixture, liquid water and water vapor, each phase being in thermodynamic equilibrium. The electrical discharge is represented by a time-dependent insertion of energy in a small region located in between the electrodes. Once the pressure wave is generated (due to phase changes), it travels into water, reaches the solid specimen eventually, and is converted into an elastic wave that travels further in the solid phase.

The thermodynamic properties of liquid and vapor follow from tabulated values. Each finite element has a single

Gauss point at which these properties are calculated. The thermodynamic properties of water depend on two variables: the temperature and the pressure. The liquid and vapor phases are separated by the saturation curve denoted as Sat (P, T) = 0, which is shown in Figure 2.1. In the case of a liquid–vapor mixture, equilibrium requires that the saturation curve be followed, therefore the saturation curve relates the pressure to the temperature [LEP 00].

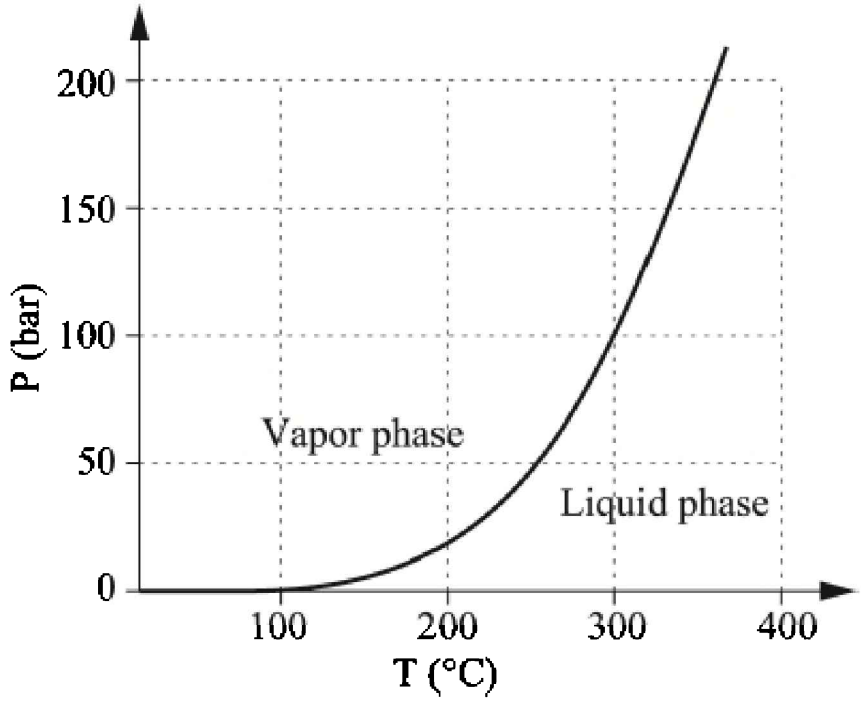

Figure 2.1. *Saturation curve of water*

The mass fraction of vapor χ is defined as:

$$\chi = \frac{m_g}{m} \qquad [2.1]$$

where m_g is the mass of vapor and m is the total mass of fluid. m_l is the total mass of liquid. The coefficient χ characterizes the concentration of vapor. When $\chi = 1$, the mixture is vapor only, and when $\chi = 0$, the mixture is made of liquid only. When $0 < \chi < 1$, the fluid is diphasic and the incremental mass per unit volume dm and the increment of

enthalpy per unit mass dh are given by:

$$dm = (m_g - m_l)d\chi + \left[\chi\left(\frac{\partial m_g}{\partial P}\right)_{Sat(T,P)=0} + (1-\chi)\left(\frac{\partial m_l}{\partial P}\right)_{Sat(T,P)=0}\right]dP \quad [2.2]$$

$$dh = (h_g - h_l)d\chi + \left[\chi\left(\frac{\partial h_g}{\partial P}\right)_{Sat(T,P)=0} + (1-\chi)\left(\frac{\partial h_l}{\partial P}\right)_{Sat(T,P)=0}\right]dP \quad [2.3]$$

where h_g and h_l are the enthalpy of the vapor and liquid, respectively. The partial derivatives are computed such that the pressure and temperature are constrained to follow the saturation curve:

$$dT = \left(\frac{\partial T}{\partial P}\right)_{Sat(T,P)=0} dP \quad [2.4]$$

The electrical discharge is considered to be a sudden surge of energy to be inserted in the system. This electrical energy is injected locally into water as a function of time during the calculations. The region in which the energy is injected is located between the electrodes. The total injected energy is distributed in the finite elements located between the electrodes:

$$W = \int_0^{\infty} \sum_{e=1}^{N} m_e^c \dot{q}_e \, dt \quad [2.5]$$

m_e^c is the mass of water in the element where the energy is injected (and is assumed to be constant during the application of energy). N is the number of elements in the area where the energy is inserted. The injected mass power in one element q_e is calculated as follows:

$$\dot{q}_e = \alpha_m \times f(t) \quad [2.6]$$

Function $f(t)$ describes the evolution of energy injected in the fluid during the discharge. The coefficient α_m is dimensionless and is calibrated from experiments.

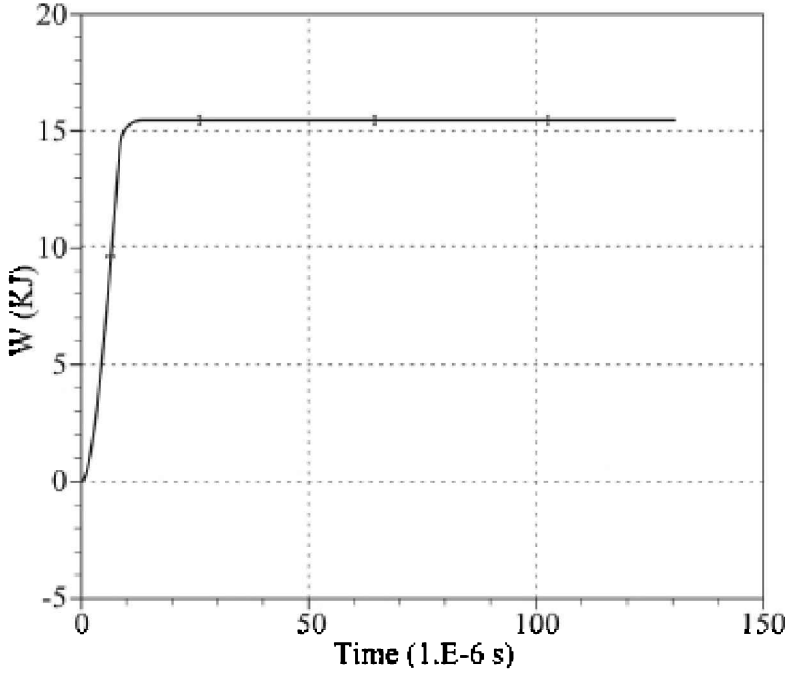

Figure 2.2. *Example of the evolution of injected energy with time*

Figure 2.2 shows a typical form of the function $f(t)$. Within 10 microseconds, the entire amount of energy is inserted in the calculation. As we will see next, this typical form provides a rather accurate description of the pressure wave generated in the liquid phase at a sufficient distance from the electrodes.

In order to check the validity of the computational model, several experiments were carried out. The setup (Figure 2.3) consists of the generation of an electrical arc between two electrodes placed in a water tank. It is similar to the set-up described in the Introduction, except that no specimen is placed in the tank. Instead, a dynamic pressure transducer located at several distances perpendicularly to the interelectrode space records the incoming pressure wave and comparisons with computations can be performed in

order to calibrate the various parameters involved in the computational scheme.

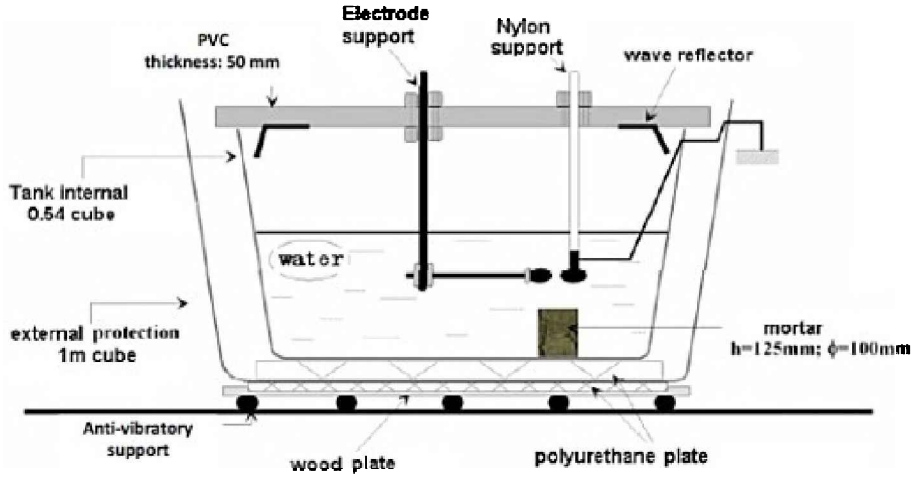

Figure 2.3. *Test configuration for the calibration of the model which simulates pressure wave generation*

Figure 2.4 shows the numerical model. The interelectrode space is located at the center of a cylinder filled with water. The upper and lower boundaries are free of displacement and displacements are fixed on the outer surface. These boundary conditions, however, do not influence the comparisons since the impact of the incoming wave on the pressure transducer is considered, prior to any reflection.

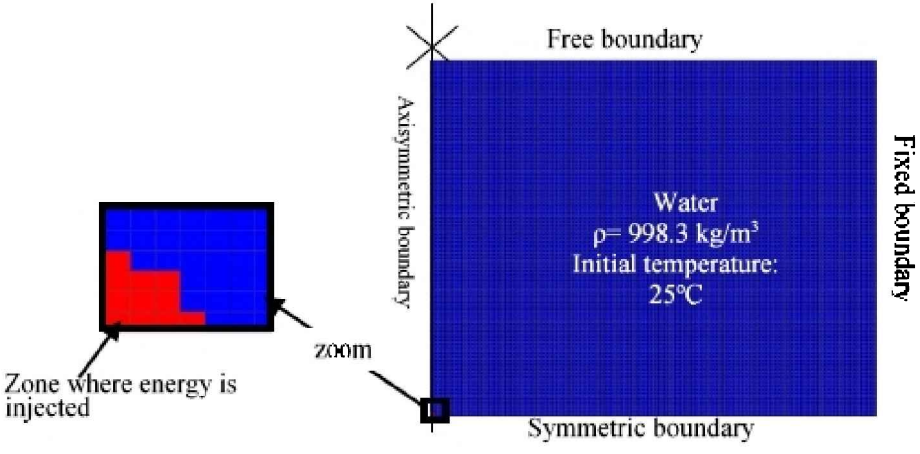

Figure 2.4. *Boundary condition and the numerical mesh of the simulation*

The interelectrode space where energy is inserted is assumed to be spherical. The diameter of this sphere is the distance between the two electrodes. Note that the electrodes are not described in the mesh, but they are considered to be small with respect to the finite element size.

The finite element grid is a Euler-type one. The mesh density has an influence on the results. It has been set to constant, after calibration between the experimental and measured pressure peaks on a low-energy configuration (energy = 3.3 kJ, distance between the electrodes and the transducer = 17.5 cm measured along the symmetric boundary in Figure 2.4). A comparison between the experimental and numerical results is shown in Figure 2.5 for an injected energy that is 10 times that used for the fit. The distance between the transducer and the electrodes is measured along the symmetric boundary.

Figure 2.6 shows, for the highest energy level considered, the computation of the evolution of the pressure wave with increasing distance from the interelectrode space. A sharp decrease in the amplitude is observed and is also expected, considering that the pressure wave is spherical with a constant energy (at best if there is no attenuation). A more detailed analysis [MAU 14] has shown that this decrease compares quite well with experimental data, except when very close to the electrodes (a distance of less than 5 cm) for the present setup.

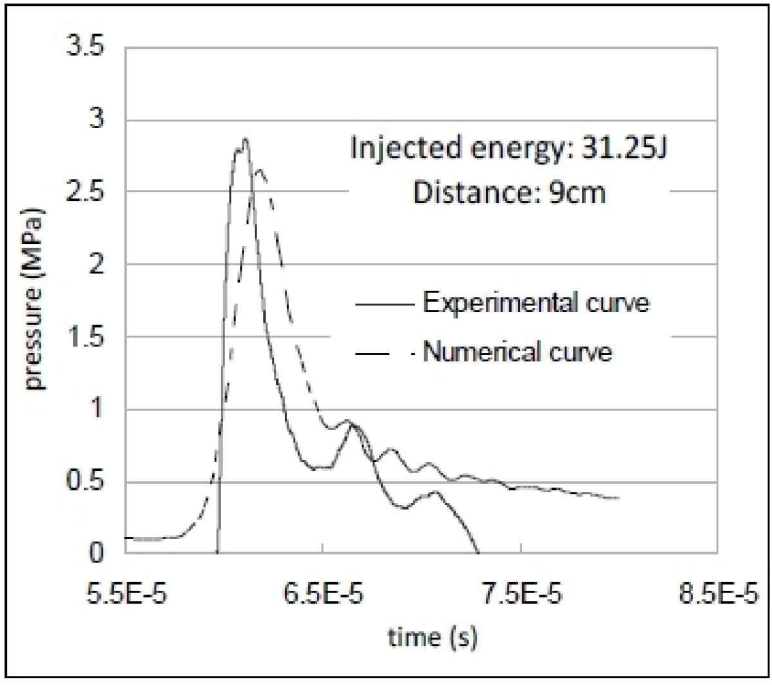

Figure 2.5. *Comparison of the experimental and the numerical pressure*

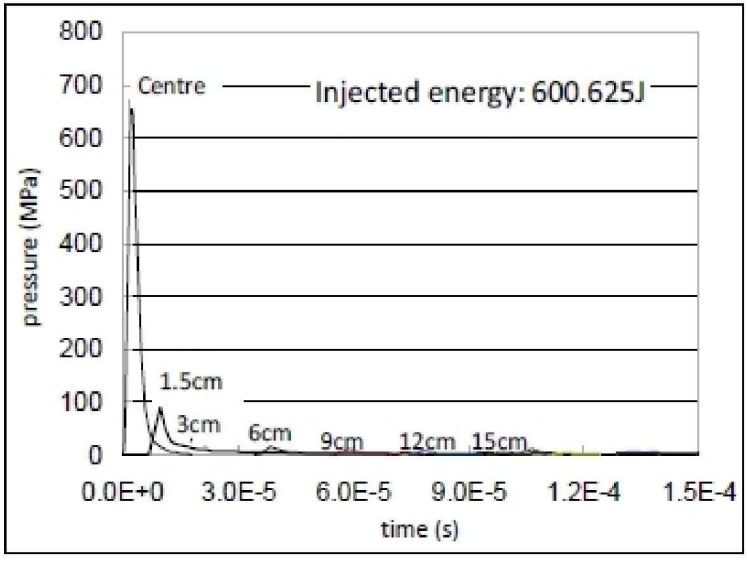

Figure 2.6. *Propagation of the pressure wave at different distances from the interelectrode space*

Figure 2.7 shows the evolution of the peak pressures with the distance between the electrodes and the pressure

transducer. The curves were fitted by the empirical formula and the numerical results are quite close to each other. The two curves are increasingly close to each other and superpose for distances larger than 12 cm.

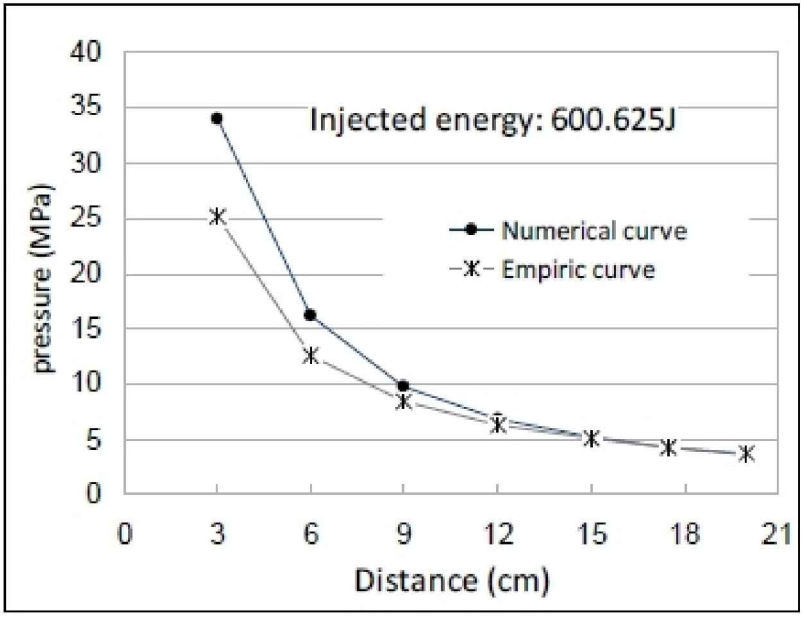

Figure 2.7. *Comparison between the numerical peak pressures and equation [2.6]*

This empirical formula may serve to provide a first estimate of the pressure generated by electrohydraulic fracturing and be useful in a design phase.

2.2. Mechanical modeling of rocks under dynamic loads

From among many constitutive models for concrete and geo-materials (soils and rocks) devised in the literature, we have chosen to implement a continuum damage-based model for several reasons. The first reason is the simplicity of the constitutive relations, both from a theoretical point of view and a computational point of view. The nonlinear response of the material is controlled by a small set of parameters, which are computed directly as a function of the applied strains. Hence, the finite element

implementation is explicit, which fits quite well with the overall computational scheme. A second reason for this choice is that the relationship between material damage (microcracking) and intrinsic permeability has some theoretical motivation [CHA 05], whereas relationships between strain and permeability do not, except in the case of Poiseuille flow in fully developed macrocracks (see, for example, [PIJ 09, YUA 04, MOO 10]), which is only the final stage of cracking considered here.

The compression and tension responses of quasi-brittle materials such as concrete and rocks are different. Mazars *et al.* (see, for example, [MAZ 86]), have used a single-damage variable approach, and extended it to crack closure effects later on [MAZ 90]. Based on this later approach, Dubé *et al.* [DUB 96] have derived an elastic damage formulation for concrete, which incorporates strain-rate effects. Gatuingt and Pijaudier-Cabot extended such models to plastic damage constitutive relations and applied those to the transient dynamic case [GAT 02]. The above models rely on scalar approaches to the degradation of elastic properties due to microcracking and neglect damage-induced anisotropy. Desmorat *et al.* [DES 07] introduced a second-order tensor in order to capture the directional effects of material damage and at the same time represent compression and tension responses according to experiments. The directionality induced by damage is an asset of this model, which will be quite useful when dealing with extension to damage–permeability coupled effects.

The constitutive relations used here are an extension of Desmorat's model, fulfilling the conservation of fracture energy upon quasi-static failure. This later aspect is required in order to cope with the difficulties coming from the strain softening response of the material [BAZ 02]. Without this feature, the model would yield zero energy dissipation upon failure that remains localized into a zone of infinitely small width. More sophisticated approaches relying on non-local models or second gradient models would certainly be feasible, although at the price of very fine meshes, which is not within the scope of developing a

computational technique suited for large-scale problems. A new expression of the equivalent strain, the variable that controls the growth of damage, is proposed to better account for the tension–compression non-symmetric response of the material. Strain-rate effects on damage growth are implemented too. The rate-dependent approach ensures the initial value problems in the presence of strain softening are well posed. It does not prevent convergence toward zero energy dissipation upon failure, as discussed by Wen *et al.* [WEN 14]. Rate dependency here is meant to describe the increase in material strength with the strain rate in the absence of localization of damage, whereas the energy dissipated upon fracture (corresponding to a completely damaged material) is set as being independent of the finite element size in quasi-static fracture propagation.

In continuum damage models, an effective stress is introduced. The effective stress, which is understood roughly as the stress supported by the material locally, differs from the apparent stress applied to the material. The difference is due to damage, i.e. to the presence of microcracks in the material. The relation between the effective stress tensor, denoted as $\tilde{\sigma}$, and the total strain tensor of the material, denoted as ε, is given as follows:

$$\varepsilon = \frac{1+\nu}{E}\tilde{\sigma} - \frac{\nu}{E} tr\left(\tilde{\sigma}\right) I \qquad [2.7]$$

with E being the Young's modulus, and ν the Poisson's ratio. The effective stress $\tilde{\sigma}$ is defined as a function of the applied stress σ on the material as:

$$\tilde{\sigma} = \left[(1-D)^{-1/2}\,\sigma^{d}\,(1-D)^{-1/2}\right]^{d} + \frac{1}{3}\left[\frac{\langle tr(\sigma)\rangle_{+}}{1-tr(D)} + \langle tr(\sigma)\rangle_{-}\right] I \qquad [2.8]$$

where σ^d denotes the deviatoric part of the stress tensor σ, D is a second-order damage tensor, $tr(\bullet)$ is the first invariant of the tensor $\bullet$ and $\langle tr(\sigma)\rangle_+$ is the positive part of the first

invariant of the stress tensor. Practically, equation [2.7] is not used in the numerical calculation but it is replaced by the inverse relationship expressing the stress as a function of effective stress:

$$\sigma = H^{-1}\tilde{\sigma}H^{-1} - \frac{(1-D)\tilde{\sigma}}{3-tr(D)}(1-D) + \frac{1}{3}\left[(1-Tr(D))\langle tr(\sigma)\rangle_+ - \langle -tr(\sigma)\rangle_+\right] \quad [2.9]$$

$$\text{with } H = (1-D)^{-1/2} \quad [2.10]$$

Note that the model accommodates crack closure in a partial way only. Crack closure effects result from the positive part of the first invariant of the effective stress. The hydrostatic term in equation [2.8] takes into account the crack closure, whereas the deviatoric term does not. Consequently, the model does not allow us to recover the initial compression stiffness upon tensile damage growth and load reversal from tension to compression. According to Desmorat *et al.*, this is prevented for the sake of the thermodynamic consistency of the formulation.

In this elastic-damage model, the domain of reversible response is defined by introducing a loading function *f*. A classical expression of this loading function is provided in equation [2.11]:

$$f = \hat{\varepsilon} - K(D) \quad [2.11]$$

with $\hat{\varepsilon}$ being the elastic equivalent strain and $\kappa(D)$ the history function related to damage growth (the equivalent of the hardening function in elasto-plasticity). In the present model, this history function and the elastic equivalent strain are defined as:

$$f = \hat{\varepsilon} - \frac{\varepsilon_0 \varepsilon_r}{\left(1 - Tr(D)\right)\left(\varepsilon_r - \varepsilon_0\right) + \varepsilon_0} \qquad [2.12]$$

$$\text{with } \hat{\varepsilon} = \sqrt{a\langle\varepsilon\rangle_+ : \langle\varepsilon\rangle_+ + \frac{1-a}{(1-2\nu)^2}\langle tr(\varepsilon)\rangle_+^2} \qquad [2.13]$$

$$\text{and } \langle\varepsilon\rangle_+ : \langle\varepsilon\rangle_+ = \sum_{i=1}^{3}\langle\varepsilon_i\rangle^2 \qquad [2.14]$$

where $\langle\varepsilon_i\rangle$ is the positive extension of the ith principal strain ε_i . ε_O is the threshold of damage in tension. Parameter a is introduced in order to adjust the ratio between the tensile and the compressive strength. The threshold of damage in tension usually corresponds to the tensile strength, whereas the threshold of damage in compression does not correspond to the compression strength. In compression, a hardening regime upon the growth of damage is observed prior to the peak stress. Hence, parameter α is fitted from a full calculation of the uniaxial response of the material.

2.2.1. *Rate-independent damage growth*

In the rate-independent case, damage growth is defined by:

$$dD_{ij} = d\lambda \frac{\varepsilon_{ij}^+}{\varepsilon_I} \qquad [2.15]$$

where dD_{ij} is the incremental growth of the component *(i,j)* of the damage tensor, $d\lambda$ is the damage multiplier and ε_I is the maximal eigen value of the strain tensor.

For the sake of illustration, let us consider a simple monotonic uniaxial load. In the rate independent case, $f < O$ describes the reversible domain. If $f = O$ and $d\dot{\lambda}f = 0$, damage evolves. For a tension loading in direction 1, the damage tensor is given by:

$$D = \begin{bmatrix} D_{11} & 0 & 0 \\ 0 & 0 & 0 \\ 0 & 0 & 0 \end{bmatrix} \quad [2.16]$$

D_{11} defines the degradation of the elastic response in the loading direction and $tr(D) = D_{11}$ The growth of damage follows from equations [2.11] and [2.12] with $f = 0$. Three stages can be observed, with functions of equivalent strain $\hat{\varepsilon}$:

If $\hat{\varepsilon} < \varepsilon_0$, $D_{11} = 0$ and the material behaves elastically.

$$\text{If } \hat{\varepsilon} > \varepsilon_0, \text{ then } D_{11} = tr(D) = 1 - \frac{\varepsilon_0\left(\varepsilon_r - \hat{\varepsilon}\right)}{\hat{\varepsilon}\left(\varepsilon_r - \varepsilon_0\right)} \quad [2.17]$$

If $\hat{\varepsilon} > \varepsilon_r$, then $D_{11} = 1$ and the material is entirely damaged.

In the general case of triaxial states of stress, the first invariant of the damage tensor may be greater than 1. Each principal value of the damage tensor is bounded by 1. Figure 2.8 shows this evolution of damage.

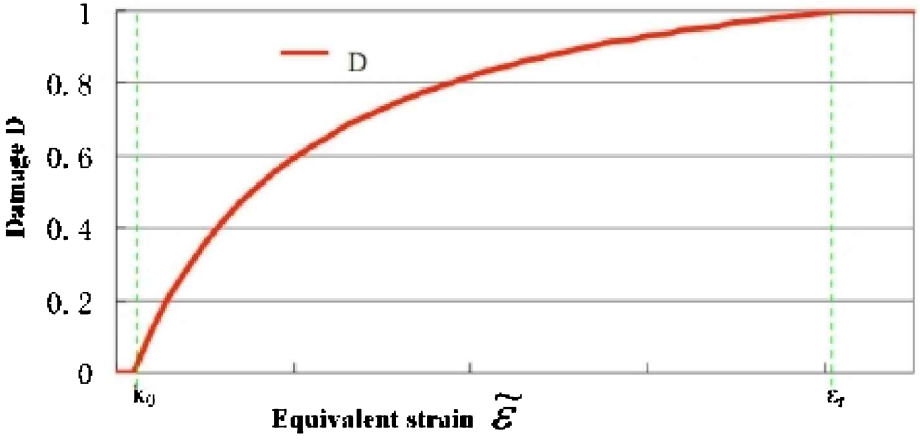

Figure 2.8. *Evolution of damage as a function of $\hat{\varepsilon}$ under uniaxial tension loading*

The elastic domain in the stress space under plane stress is shown in Figure 2.9. For comparison purposes, we have also plotted the elastic domain given by classical isotropic damage model [MAZ 86]. Although the two domains are quite similar in the tensile quadrant, the tension/ compression domain and the bi-compression domains are quite different. This is essentially due to the fact that we are dealing here with damage-induced anisotropy, whereas the scalar damage model preserves the elastic isotropy of the material upon microcrack growth. Since most of the micro- and macrocracks are directionally oriented in practice, the isotropic damage model should be regarded as a simplified constitutive relation and it is well known that it may not be adequate in the cases of biaxial and triaxial loads.

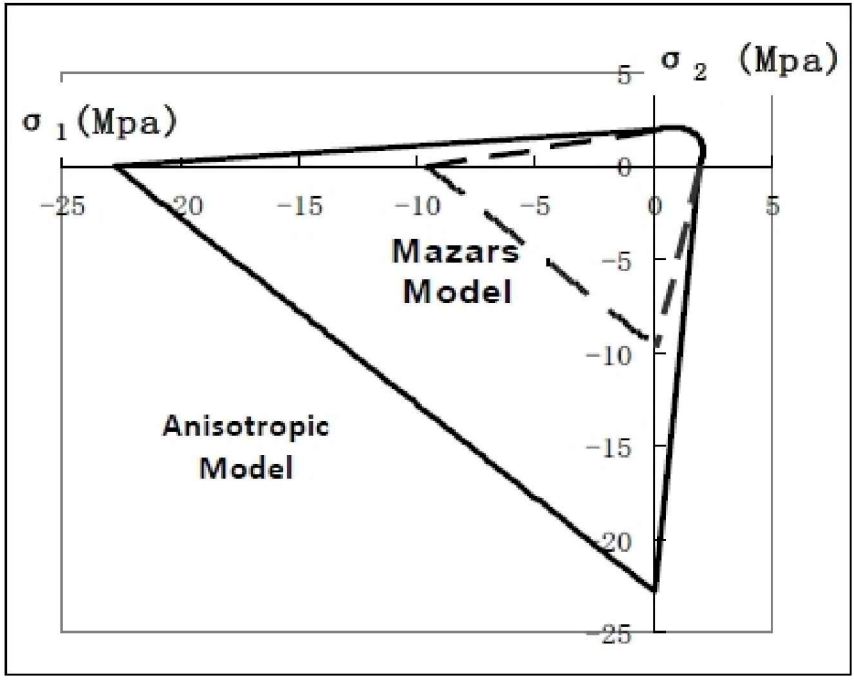

Figure 2.9. *Elastic domains in the case of plane stress*

2.2.2. *Rate-dependent damage growth*

In the case of dynamic load, which applies here in electrohydraulic fracturing, it is essential to account for the time-dependent response of the material. For instance, it is well known that the compressive strength of mortar

increases with the loading rate and if we intend to validate the constitutive models on the experiments performed on mortar, it is important to capture this effect. Rate dependency will be inserted in the expressions for damage growth. Doing this, we assume that the elastic response of the material is rate-independent. This is a simplifying assumption which avoids the implementation of viscoelasticity.

Following classical approaches used in viscoplasticity, the rate-dependent damage model starts from the same equations as the rate-independent one, except for the damage multiplier. Equation [2.16] is replaced by:

$$\dot{D}_{ij} = \dot{\lambda} \frac{\varepsilon_{ij}^{+}}{\varepsilon_I} \qquad [2.18]$$

in which the rate of damage and the damage multiplier replace their incremental values. The damage multiplier rate is defined according to a format that is similar to Perzyna's viscoplasticity (see [DUB 96]):

$$\dot{\lambda} = \frac{1}{M} \left\langle \frac{f}{\varepsilon_0} \right\rangle^n \qquad [2.19]$$

The material parameters M and n are used to control the rate-dependant effect on damage growth.

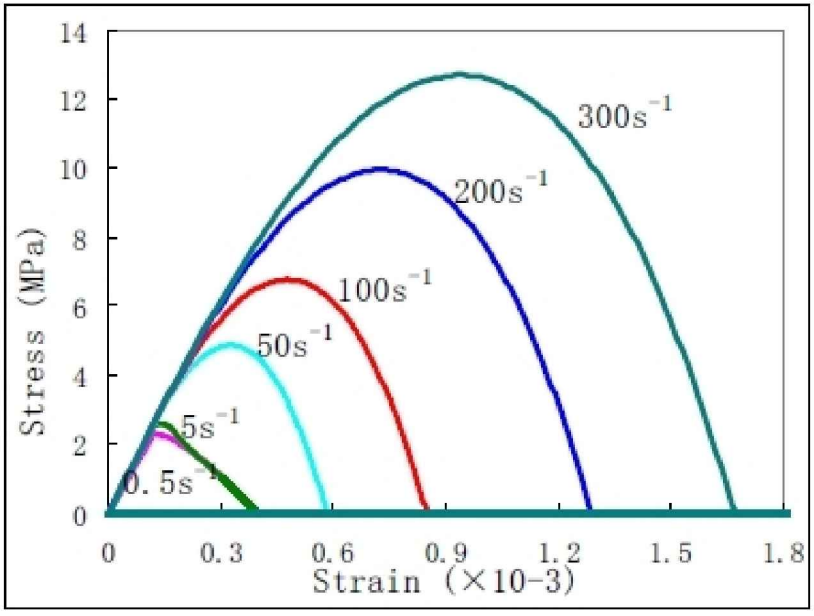

Figure 2.10. *Uniaxial tensile response of the rate-dependent model according to increasing strain rates*

Figure 2.10 shows the monotonic stress–strain curves for concrete in tension at different loading rates. The model parameters used for this calculation are: E =19.3 GPa, ν = 0.2, $\varepsilon_0 = 1\,10^{-4}$, $\varepsilon_r = 8\,10^{-4}$, $M = 1\,10^{-5}$ and $n = 0.4$. The higher the rate, the higher the strength. In practice, if the deformation rate is small (less than 1 s^{-1}), the rate-independent response is almost recovered.

Overall, the constitutive relations contain five parameters which define the static behavior: the Young's modulus E, the Poisson's ratio υ and the damage threshold ε_0; parameter a controls the strength in compression compared to the material response in uniaxial tension; the fracture strain ε_r is related to the fracture energy and the finite element size, as we will see next. The two parameters M and n are added into the elastic rate-dependent damage law to control the material response in dynamic loading. They should be calibrated such that the dependence of the material strength in tension with the strain rate corresponds to experimental data. Figure 2.11 shows a compilation of such data from the literature results.

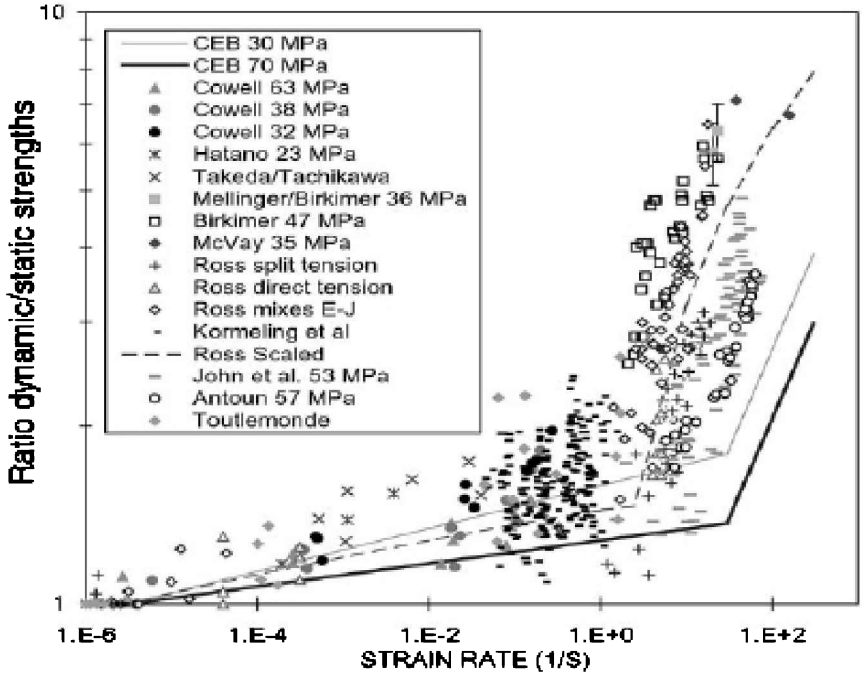

Figure 2.11. *Strain rate effect of the tension strength of concrete (after [MAL 98])*

2.2.3. *Failure and strain softening*

In the rate-independent format, the above constitutive relations exhibit strain softening and need to be regularized since in this case solving the equation of motion or the equilibrium equations is an ill-posed problem (see, for example, [PIJ 93]). As pointed out by Dubé *et al.* [DUB 96], the rate-dependent counterpart of this formulation does not exhibit this problem. The format of the rate-dependent constitutive equations ensures that the boundary/initial value problems are well posed. There is, however, a fundamental difference between rate-dependent (Perzyna type) plasticity and rate-dependent damage. In the plastic formulation, an internal time – or an internal length – appears explicitly in the governing equations. This is not the case in the rate-dependent damage model.

In order to clarify this point and following the discussion in [CHE 14], let us consider a simplified version of the above constitutive equations. For the sake of simplicity, crack

closure effects have been removed and damage is assumed to be isotropic. The stress–strain relation in the rate format reads:

$$\dot{\sigma} = \left(1 - d^0\right) \cdot C : \dot{\varepsilon} - \dot{d} \cdot C : \varepsilon^0 \qquad [2.20]$$

where d^0 and ε^0 are the initial states of damage and strain from which the perturbation of the state of deformation is computed, C is the initial elastic stiffness of the material $\dot{\sigma}$ and $\dot{\varepsilon}$ are the stress and strain rates, respectively. We may substitute the evolution of damage in this expression:

$$\dot{\lambda} = \frac{1}{M} \left\langle \frac{f\left(\varepsilon^0, \varepsilon_0\right)}{\varepsilon_0} \right\rangle^n \qquad [2.21]$$

Then, equations [2.20] and [2.21] are inserted into the wave equations:

$$div\left[\left(1 - d^0\right) \cdot C : \dot{\varepsilon} - \frac{1}{M} \left\langle \frac{f\left(\varepsilon^0, \varepsilon_0\right)}{\varepsilon_0} \right\rangle \cdot C : \varepsilon^0 \right] = \rho \frac{\partial^2 v}{\partial t^2} \qquad [2.22]$$

where v is the velocity field solution of the equation of motion. As in classic strain localization analyses, we will consider deviations from an initial state of homogeneous strain and damage. Hence, equation [2.22] reduces to:

$$div\left[\left(1 - d^0\right) \cdot C : \dot{\varepsilon} \right] = \rho \frac{\partial^2 v}{\partial t^2} \qquad [2.23]$$

This equation is the classical one for the propagation of elastic waves in a damage medium of stiffness $(1-d^0).C$. This is the reason why the equations of motion are well

posed. It is the (positive definite) unloading stiffness instead of the tangent (softening) stiffness that enters in the wave equation. As observed in [DUB 96], a third-order derivative appears in the equations of motion in the case of rate-dependent plasticity of Perzina's type. This is clearly not the case in the rate-dependent damage constitutive equations. On the one hand, the wave equations remain well posed, but on the other hand the perturbation travels with a lower speed as damage grows according to equation [2.23]. When complete failure has occurred in a single finite element, the perturbation can no longer propagate.

In dynamics, the specific form of wave equation [2.23] yields a propagation of strain waves depending on the current state of damage. It follows that the width of the localized damage profiles at failure is non-zero and depends on the history of damage. The profiles of localized strain exhibit a peak over a single finite element at complete failure, as observed by Dubé *et al.* [DUB 96].

In a quasi-static setting, the effects of inertia are neglected. The right-hand side term in equation [2.23] vanishes. It does not imply, however, that strain rate effects do not occur. Again, the differential equations of equilibrium remain well posed. When the strain rate decreases, results obtained with the rate-independent damage model should be recovered. In the limit of an infinitely slow strain rate, the constitutive response converges toward the underlying rate-independent model. The problem inherent to the local formulation of rate-independent damage, i.e. failure without energy dissipation, is recovered in this case. It follows that fracture energy, which is the total energy dissipated due to damage in the localization band, depends on the strain rate and on the parameters that control this effect. At the same time, fracture energy vanishes within the limit of vanishing strain rate. Fracture without energy dissipation occurs in this limit case.

At this point, it is important to notice that the parameters which control the strain rate effect on the constitutive response cannot be fitted at the same time in order to (1) provide the correct rate effect on the material strength in

dynamics and (2) provide the correct fracture energy in the quasi-static regime (with a non-zero strain rate). In addition, such a simultaneous fit would be impossible within the limit of a fracture energy measured under a vanishing strain rate since the energy dissipation provided with the model is zero. Hence, the energy dissipation in the quasi-static regime needs to be controlled independently from the rate effect on strength, even though the equations governing the problem remain well posed. One technique, which has been implemented in this chapter, is the classical crack band approach [BAZ 83]: conservation of the fracture energy upon mesh refinement is ensured by changing the softening response of the material with the finite element size.

The basic assumption is that the width of the crack band is equal to the size of a single element. The fracture energy G_f is given by:

$$\frac{G_f}{h} = \int_0^{+\infty} \sigma d\varepsilon \qquad [2.24]$$

where h is the finite element size. Since the fracture energy should be independent of the element size, the constitutive relations are adjusted so that equation [2.24] is satisfied whatever the finite element size in the case of uniaxial tension. More precisely, it is the fracture strain ε_r in the underlying time-independent response of the material which changes so that equation [2.24] is satisfied whatever h.

Note that because of the rate effect on the constitutive response, there will be a rate effect induced on the fracture energy in the dynamics. The results obtained with the above constitutive relations will, however, be consistent with respect to two criteria: the rate effect on material strength observed from experiments and the fracture energy measured in statics (for sufficiently small strain rates). The agreement with both considerations could not be reached without a combination of rate-dependent effect on the constitutive response and the crack band model (or any

other non-local/gradient formulation which introduces an internal length).

2.3. Coupled effects between damage and permeability

The relationship between damage and the intrinsic permeability of the material is motivated by the theoretical results obtained by Chatzigeorgiou *et al.* [CHA 05]. In this work, it was established that under the assumption of distributed microcracking, the permeability of the material should be related to the variation of the elastic stiffness of the material. Upon localization of microcracking into a macrocrack, a change of regime is expected, the material permeability being controlled by the aperture of a macrocrack, e.g. following Poiseuille flow [PIJ 09].

Experimentally, several data show the dependence of the intrinsic permeability of the material to damage, see, for instance, the experimental work by Choinska *et al.* [CHO 07] or Picandet *et al.* [PIC 01]. Figure 2.12 shows such a result obtained in compression by Choinska, on a geometry of specimens that is similar to the hollow cylinder used for the present study.

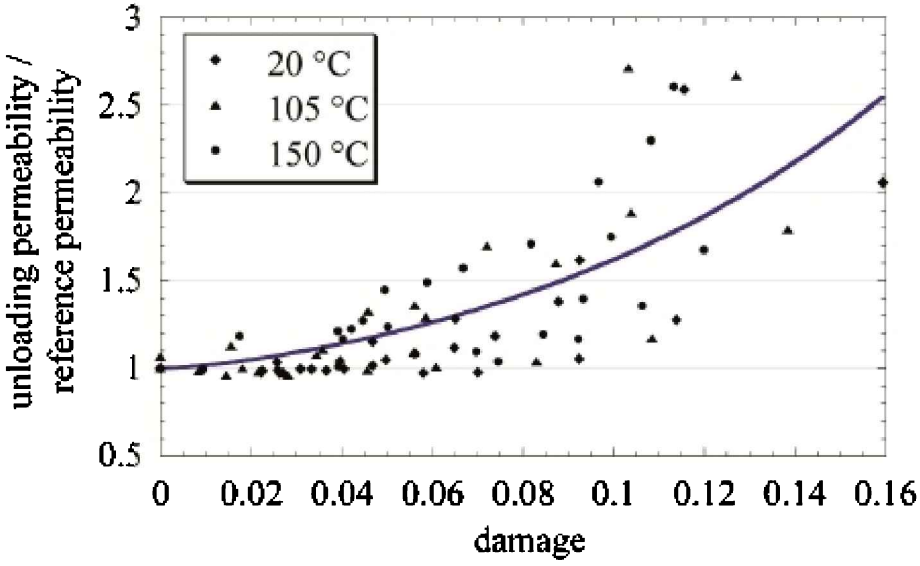

Figure 2.12. *Variation of the relative permeability of concrete with damage at various temperatures (after [CHO 07])*

A relationship between isotropic damage and intrinsic permeability [equation I.1]) has been proposed by Bary *et al.* [BAR 00] and has also been used by Schreffler *et al.* [SCH 02] and Jason [JAS 07]. The formulae implemented by Jason in the context of isotropic (scalar) damage read:

$$K = K_0 \text{ if } D < D_0 \text{ and } K = K_0 \cdot 10^{c(D-D_0)} \text{ if } D \geq D_0 \quad [2.25]$$

with K_0 being the intrinsic permeability of undamaged material, K the intrinsic permeability of damaged material, D_0 the damage threshold under which permeability is unaffected by damage and D the damage scalar in an isotropic model. c is a model parameter.

Figure 2.13 shows the fit of this equation with data in uniaxial compression obtained by Bary [BAR 96]. The dotted line on this plot corresponds to the model proposed by Choinska, which fitted the data in Figure 2.12 and which should hold in the case of low values of damage only, prior to any localized cracking. Equation [2.25] holds for a wide

range of damage values and is applicable in the context of the tightness assessment of concrete nuclear vessels [JAS 07].

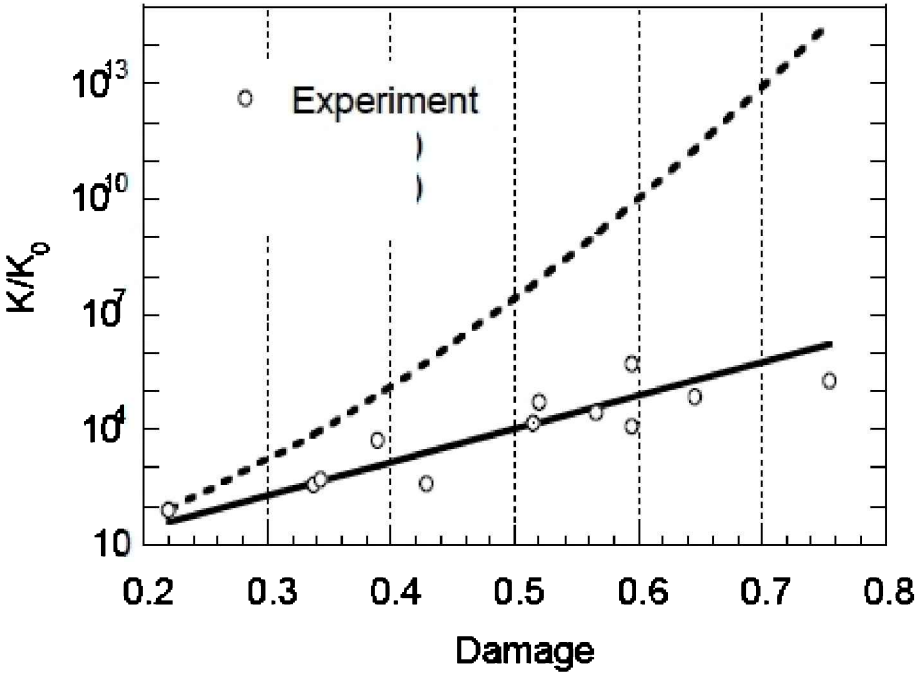

Figure 2.13. *Evolution of the intrinsic permeability with damage. The solid line corresponds to the fit of equation [2.25]. Experimental results from [BAR 96]*

In the present case, damage is represented by a second-order tensor. We will use the same type of relationship between damage and intrinsic permeability, and directional effects on the permeability will be inserted. The intrinsic permeability is a second-order tensor, under the same format as the damage tensor. In addition, we will assume that the principal directions of the damage tensor and the permeability tensor coincide.

In the 3D coordinate system corresponding to the principal axes of damage, damage in one direction is due to cracking in orthogonal directions. Hence, damage growth in one direction generates an increase in permeability in the two orthogonal directions. In other words, the augmentation of the permeability in one direction depends on the two perpendicular principal values of damage. Following this

principle, permeability in direction i is computed according to the maximum value of damage in the two orthogonal directions (j,k). Equation [2.25] is adapted to the anisotropic case accordingly:

$$K_i = K_0 \quad \text{if } Max\left(D_j, D_k\right) \leq D_0 \qquad [2.26]$$

$$K_i = K_0 \cdot 10^{c\left(Max\left(D_j, D_k\right) - D_0\right)} \quad \text{if } Max\left(D_j, D_k\right) > D_0$$

where K_i is the permeability in principal damage direction i. D_j and D_k are the values of damage in principal axes normal to axis i. Note that for the sake of simplicity, and in order to avoid additional calibration, the parameters (c = 8.65) and (D_0 = 0.035) are kept the same as those fitted in Figure 2.13 by Jason *et al.* throughout the study. If the material is completely damaged (Max(D_j, D_k) = 1), then the relative increase in permeability K_i/K_0 is set to $10^{-9}m^2$ approximately, which is a sufficiently high value for the present purposes.

2.4. Summary and conclusions

Several models needed to be developed in order to achieve the numerical simulation of electrohydraulic fracturing. We have chosen to start this process on the basis of an explicit finite element code capable of handling hydrodynamics and solid mechanics at the same time. The electrical discharge into water is captured by inserting energy locally, within the interelectrode space. This energy produces vapor explosion and the liquid–vapor interface moves so quickly that it generates a pressure wave. Macroscopically, this is handled by considering that liquid and vapor form a two-phase mixture and the pressure wave arises naturally from the conservation equations.

On the solid-phase side, an anisotropic rate-dependent

damage model is implemented. This constitutive relation is complemented with the growth of intrinsic permeability due to damage. The damage and intrinsic permeability second-order tensors possess the same principal directions.

In Chapter 3, we are first going to fit the model with the help of some of the experiments that have been performed and presented in the Introduction and Chapter 1. We will then look at the model predictions on the other experiments available. This stage should be seen as a prerequisite before calculation on the representative geometries of the reservoir can be envisioned.

3
Validation of the Computational Model

As a first step, we are going to perform the computation of the experiments involved in the feasibility analysis and described in the Introduction. Using this simple geometry, the computational model can be tested quite easily and comparisons with the evolution of permeability observed in the sample may be performed. Then, we will compare our results with the experiments performed in conditions representative of geological reservoirs (those discussed in Chapter 1).

3.1. Simulation of the experiments in uniaxial compression

Here we consider the specimens tested in the setup described in Figure I.1. The specimens are mortar cylinders (diameter 100 mm, and height 125 mm) with the average characteristics given in Table 3.1 (the Poisson coefficient was not measured and was taken to be equal to 0.2).

Table 3.1. *Average mechanics of the specimens tested in uniaxial compression*

Compression strength (MPa)	Tensile strength (MPa)	Young's modulus (MPa)	Intrinsic permeability (m^2)
19.6	4.9	17,300	4.10^{-17}

The finite element mesh used is shown in Figure 3.1. A quarter of the specimen is meshed using symmetrical conditions in order to reduce the computation time. The compressive pressure wave is applied to the top face of the specimen.

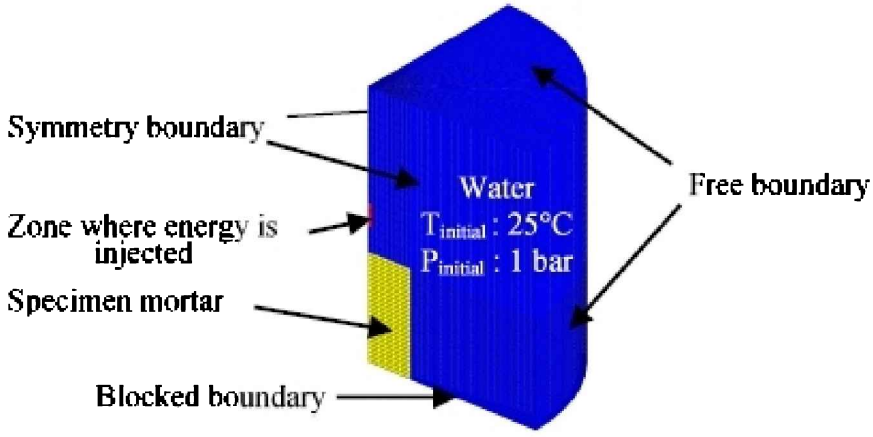

Figure 3.1. *Finite element mesh of the simulation*

The radial, tangential, vertical and principal damage computed for single shocks corresponding to increasing pressure levels are presented in Figures 3.2–3.4. Damage evolves with the peak pressure. The radial and orthoradial damage values are greater than the vertical damage, and are related to the transverse positive strains upon compression due to the Poisson effect.

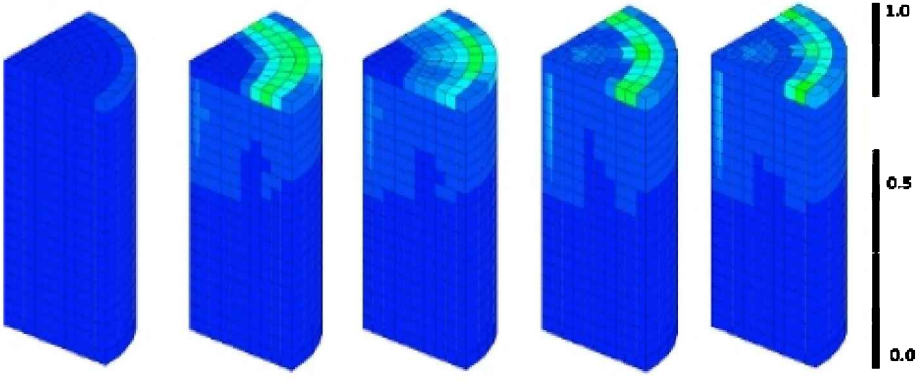

Figure 3.2. *Radial damage at different pressure levels for increasing peak pressure applied (from left to right: 28, 79, 105,193 and 216 MPa). For a color version of the figure, see www.iste.co.uk/pijaudier/drystone.zip*

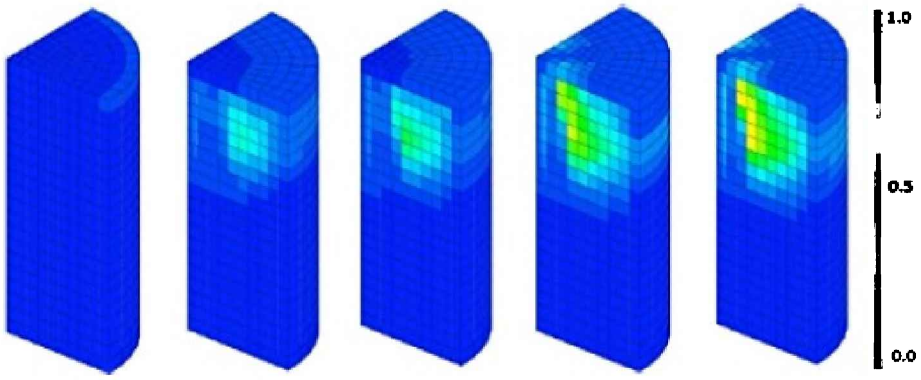

Figure 3.3. *Tangential damage at different pressure levels for increasing peak pressure applied (from left to right: 28, 79, 105,193 and 216 MPa). For a color version of the figure, see www.iste.co.uk/pijaudier/drystone.zip*

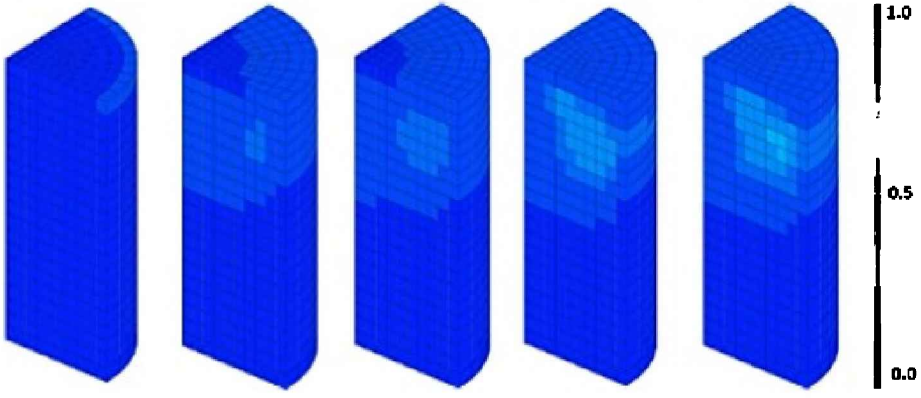

Figure 3.4. *Vertical damage at different pressure levels for increasing peak pressure applied (from left to right: 28, 79, 105,193 and 216 MPa). For a color version of the figure, see www.iste.co.uk/pijaudier/drystone.zip*

In order to better visualize the overall intensity of the damage, Figure 3.5 shows the distribution of the largest principal value of damage. We can see that the major damage develops near the upper surface of the specimen, where the pressure waves impact the cylinder. With increasing peak pressure, damage penetrates the specimen.

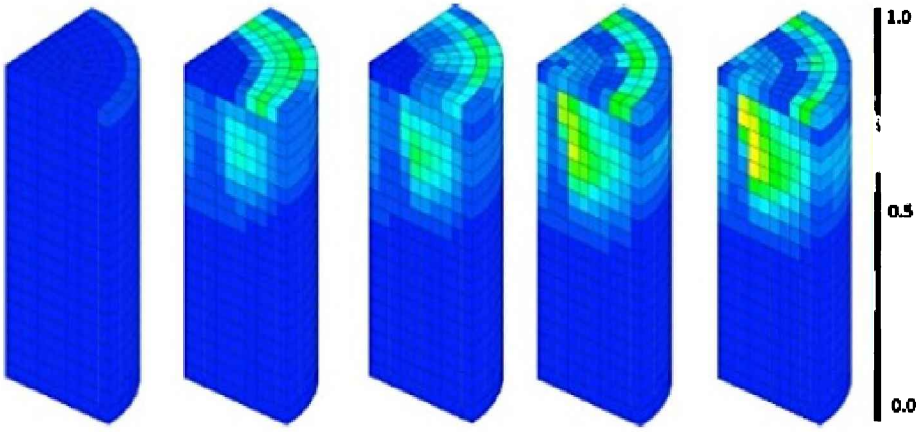

Figure 3.5. *Largest principle damage at different pressure levels for increasing peak pressure applied (from left to right: 28, 79, 105,193 and 216 MPa). For a color version of the figure, see www.iste.co.uk/pijaudier/drystone.zip*

Figure 3.6 presents the comparison between X-ray tomography scans and the distribution of principal numerical damage, which is the same in a plane perpendicular to the direction of loading. In the X-ray scans, the higher the density, the darker the grey. Therefore, light zones correspond to damage zones.

In the calculations, damage appears symmetrically at the top part of the specimen. It forms two symmetric zones delimited by a conical surface inside. This distribution seems to correlate, qualitatively at least, with the experiments.

As in the experimental measurements of permeability to nitrogen, the calculation of an apparent permeability was carried out on cylindrical specimens extracted from the top of the numerical model from the computational model. Only the upper part of the model, where damage develops, was kept for further calculations. Since the distribution of damage was quite heterogeneous, it was necessary to perform a hydraulic calculation in order to obtain the overall apparent permeability. Such a calculation, similar to stationary heat calculation, is very simple and a standard (linear) finite element code can be used for this purpose. It

relies on Darcy's equation, with a heterogeneous distribution of permeability. In the computation, the intrinsic permeability was entered at each Gauss point according to the constitutive model [2.27]. The outcome of the calculation was a fluid flux, given a pressure gradient. The relation was linear and the coefficient of proportion was the average intrinsic permeability of the damaged specimen.

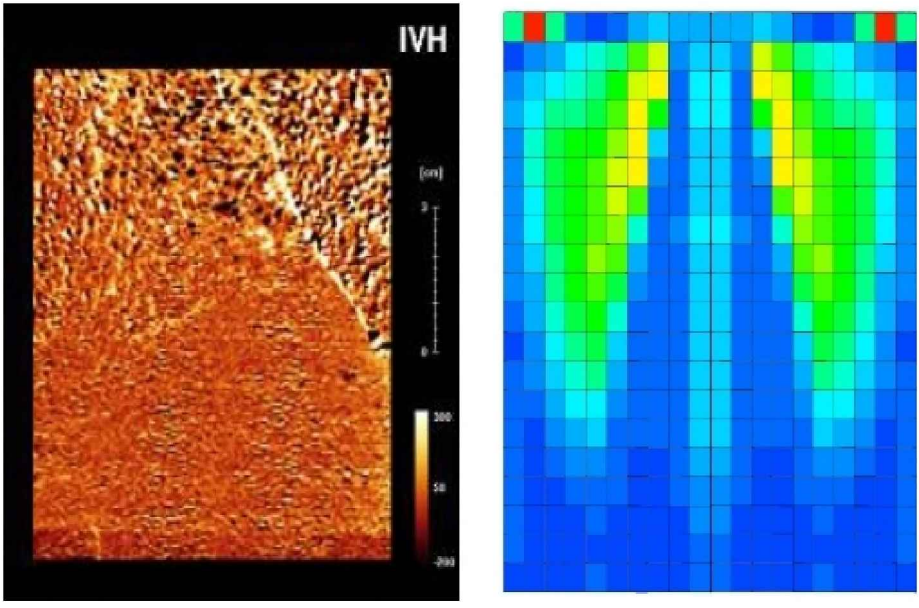

Figure 3.6. *a) Vertical cross tomography scans of a specimen submitted to one shock under 250 MPa; b) principal damage distribution computed under 216 MPa. For a color version of the figure, see www.iste.co.uk/pijaudier/drystone.zip*

Figure 3.7 shows the variations in permeability according to the numerical and experimental results. We may observe a very good correlation.

Let us underline that we are not performing a predictive calculation here. The model parameters have been fitted so that the variations in permeability can be reproduced. Hence, this result shows that the computational model described in Chapter 2 provides consistent results for uniaxial compression tests. We now need to check if it is still the case on configurations that are more representative of

reservoir conditions. As we will see next, since we have data for several confinement levels, we will use some for fitting the model parameters and the others for the purpose of checking the ability of the model to provide results that are close to the experimental data.

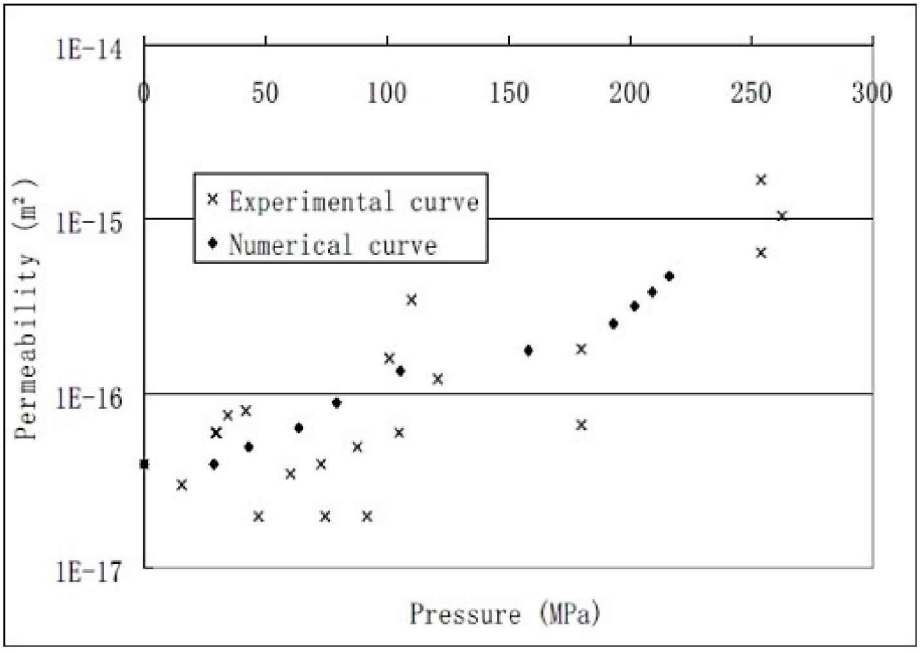

Figure 3.7. *Comparison of the experimental and numerical permeability as a function of the amplitude of the pressure wave*

3.2. Confined tests on hollow cylinders

We now consider the configuration reported in Chapter 1, where a hollow cylinder is placed in a stress environment that is representative of reservoir conditions. The electrical discharge occurs inside the hollow cylinder, which is filled with water at ambient pressure. In this section, only the tests on the mortar specimen will be considered. The geometry of the 3D finite element model and the boundary conditions are shown in Figure 3.8.

The specimen, water inside the hollow cylinder, and the concrete blocks used to produce the confinement are represented in a 3D finite element mesh made up of eight

node finite elements with a single Gauss point. Only a quarter of the specimen is represented, taking advantage symmetry in order to reduce the computation time. The electrodes, the hydraulic jack and the steel rings are not represented in the finite element model.

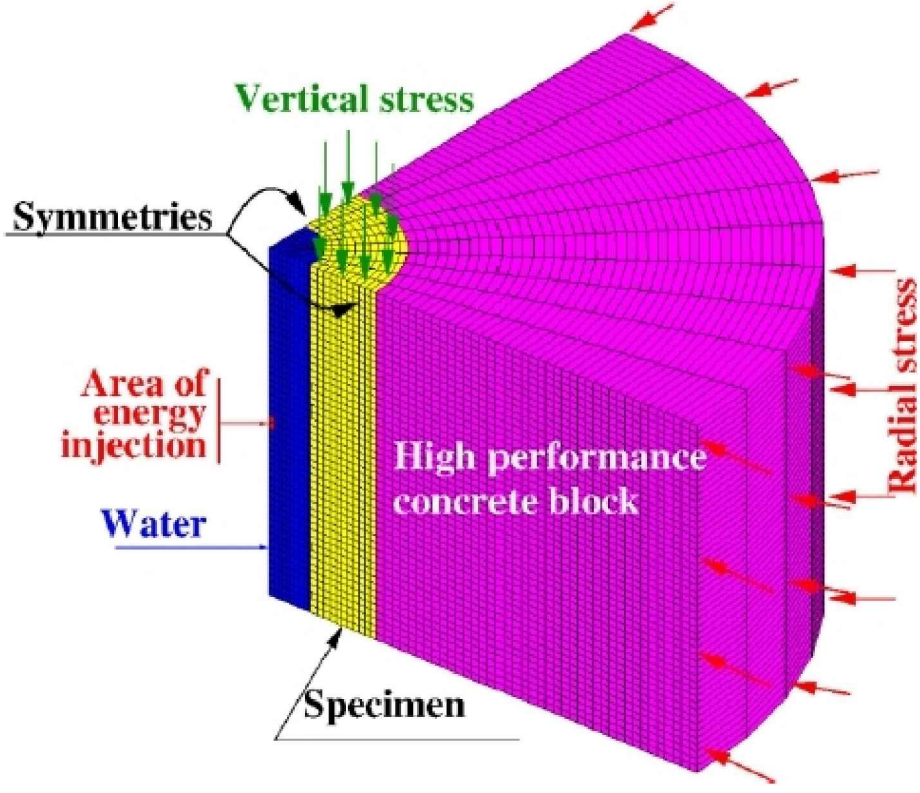

Figure 3.8. *Finite element model of the simulation of tests on hollow cylinders*

Energy is inserted at the centre of the hollow cylinder in the water in order to generate the shock wave. In the course of the calculation, part of this wave is reflected at the water –concrete interface, and another part is transmitted to the specimen. Multiple reflections occur, which means that the effective load applied on the specimen is rather complex and it is more accurate to consider a full finite element model instead of applying to the mortar the pressure history that results from the electrical discharge specimen. Note also that water cannot leave the specimen. The upper and lower boundary conditions are impervious, which again induces

some reflection.

The geometry of the specimen is as follows: external diameter = 125 mm, internal diameter = 50 mm and height = 180 mm. The average compressive and tensile strengths, the elastic modulus and the intrinsic permeability of the mortar are provided in Table 3.2. The compressive and tensile strengths have been determined from tests on 40 × 40 × 40 mm cubic specimens and on 40 × 40 × 160 mm specimens, respectively. The tensile strength is obtained from 3-point bending tests. The Poisson's ratio has not been measured and the same value as in the previous section was used ($\upsilon = 0.2$).

Table 3.2. *Average mechanical properties of mortar*

Compression strength (MPa)	Tensile strength (MPa)	Young's modulus (MPa)	Initial permeability (m^2)
19.6	4.9	19,300	$1.\ 10^{-17}$

The vertical load and lateral confinement correspond to the three depth levels defined in Chapter 1 (Table 1.1).

What is aimed at is a proper description of the evolution of permeability after electrohydraulic fracturing. Once the mechanical calculation is performed, the distributions of damage are converted into distributions of intrinsic permeability. Hydraulic calculations with the same boundary conditions as in the experiments (see Figure 1.4) are performed. From the total radial flow of gas through the specimen, the average intrinsic permeability is obtained. In the following comparisons, it is this permeability that is going to be related to the amount of energy injected for the generation of the shock wave.

3.2.1. *Numerical results under low confinement*

The low confinement corresponds to a hydrostatic state of stress providing tightness to the water of the borehole (2 MPa).

It is so moderate that the vertical and radial stresses have been assumed to be zero in the computations (for the sake of simplicity). The electrical discharge generates shock waves in the central zone of the hollow cylindrical specimens in water. Figure 3.9 shows a typical time evolution of the pressure wave in the finite element model.

The pressure wave hits the mortar specimen at about 22 μ and the confining blocks after 40 μ. Multiple reflections can be observed in water with time.

Figure 3.10 shows the evolution of damage in the model. The calculations have been carried out for a single shock with increasing energy levels. For the sake of readability, water has been removed from the model in the figure.

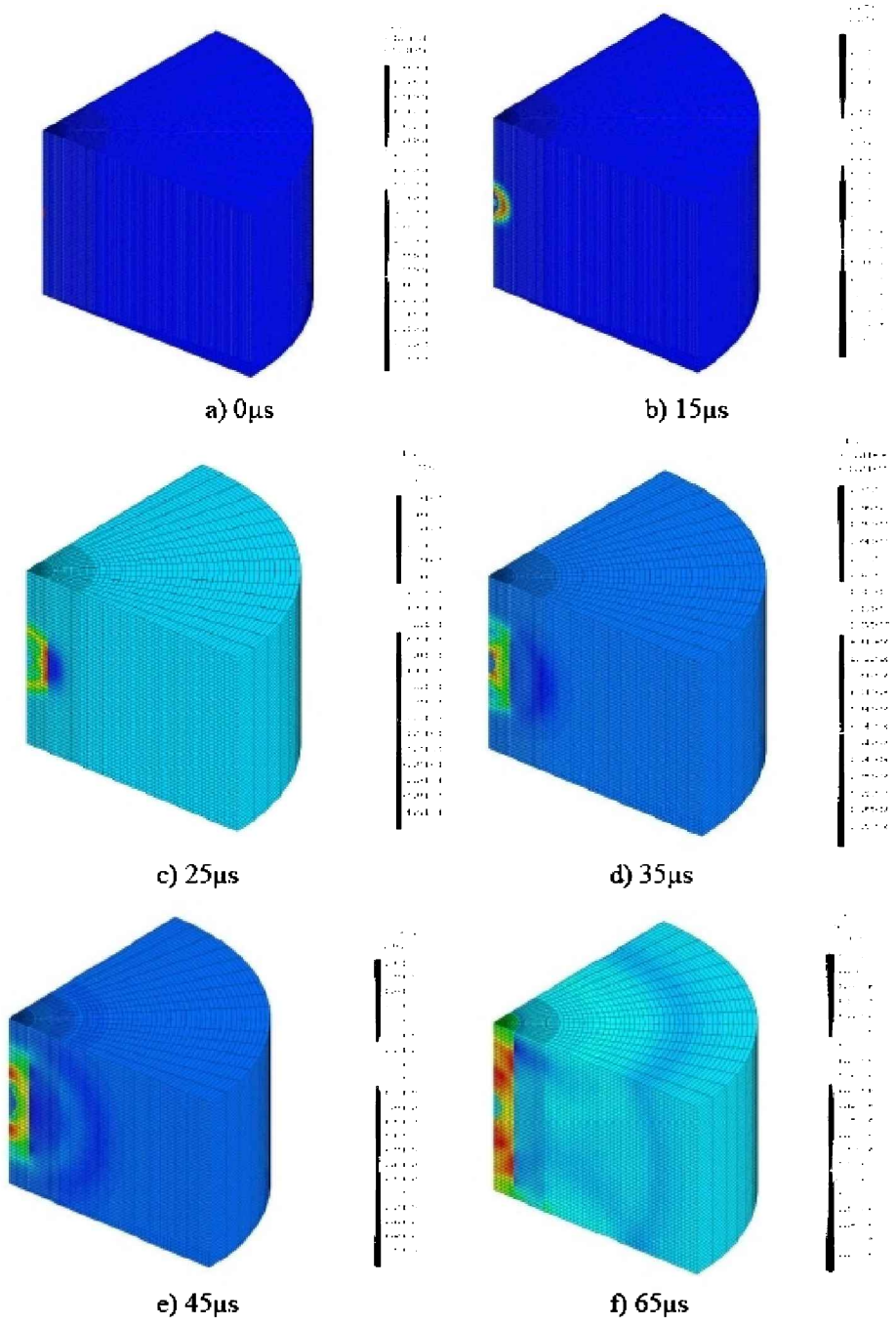

Figure 3.9. *Typical evolution of the pressure overtime during the calculation for low confinement. For a color version of the figure, see www.iste.co.uk/pijaudier/drystone.zip*

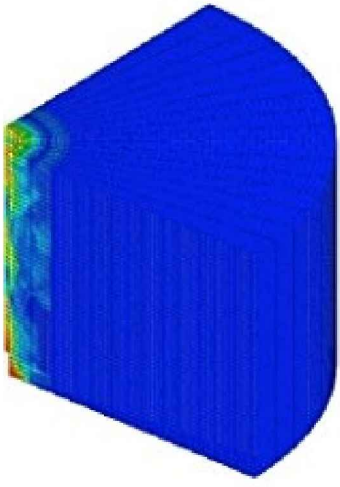

a) 188J

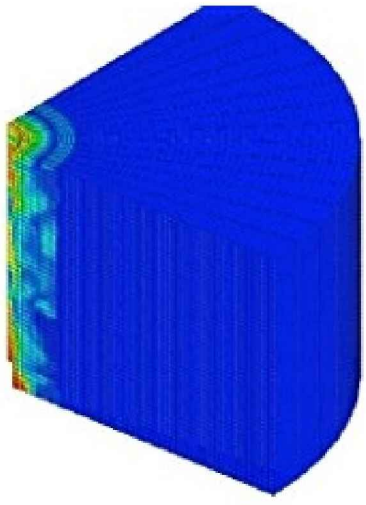

b) 245J

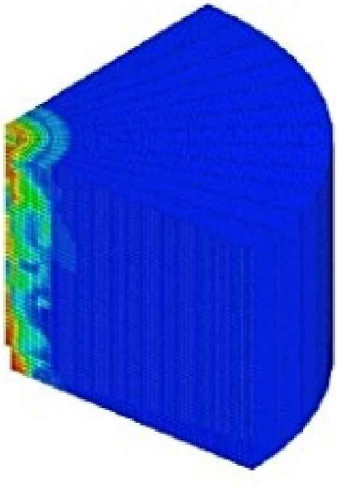

c) 330J

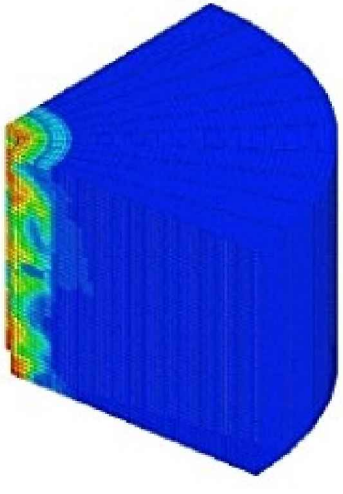

d) 470J

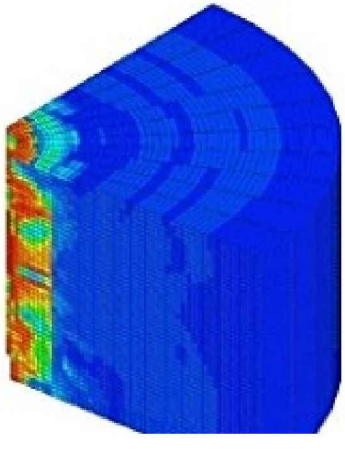

d) 1,35kJ

Figure 3.10. *Evolution of damage in the model with injected energy for low confinement. For a color version of the figure, see www.iste.co.uk/pijaudier/drystone.zip*

Figure 3.11 shows the distributions of tangential damage for two levels of injected electrical energy. Based on the coupling between anisotropic damage and permeability, the flux vector computed in the hydraulic calculation is also plotted. Note that for the sake of illustration, different scales have been used for the flux vector (otherwise the flow would not be distinguished in the case of small energy). The flux orientations provide an illustration of the effects of the microcracks generated by shock waves that are neither unidirectional nor distributed homogeneously over the specimens. More microcracks are generated with 1.35 kJ of injected energy than with 188 J.

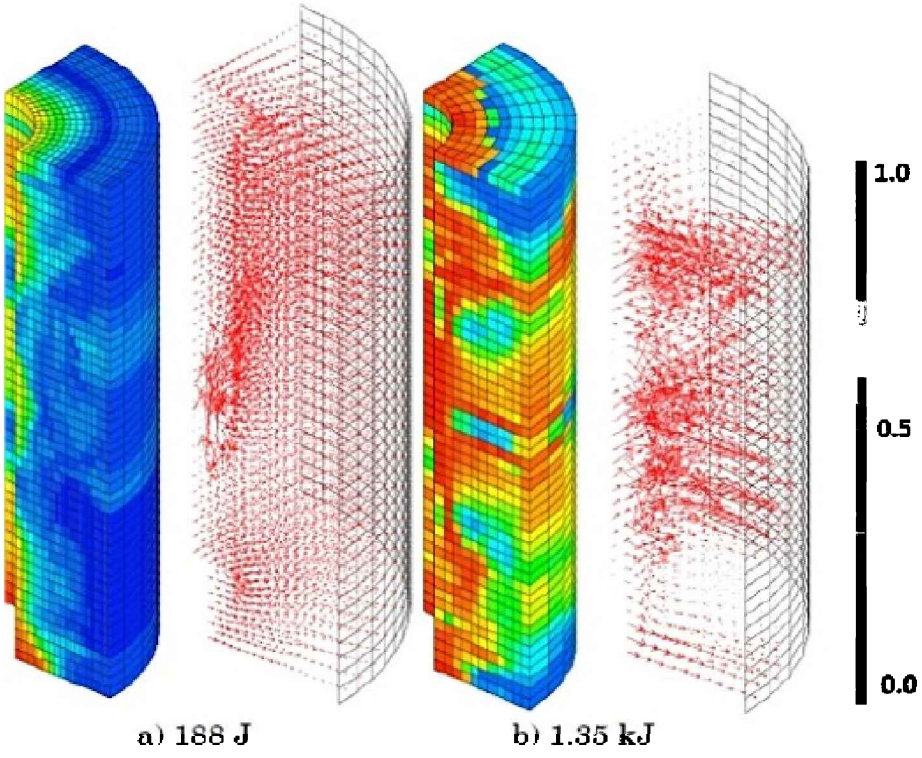

Figure 3.11. *Evolution of damage and the flux vector with different levels of injected energy under low confinement. For a color version of the figure, see www.iste.co.uk/pijaudier/drystone.zip*

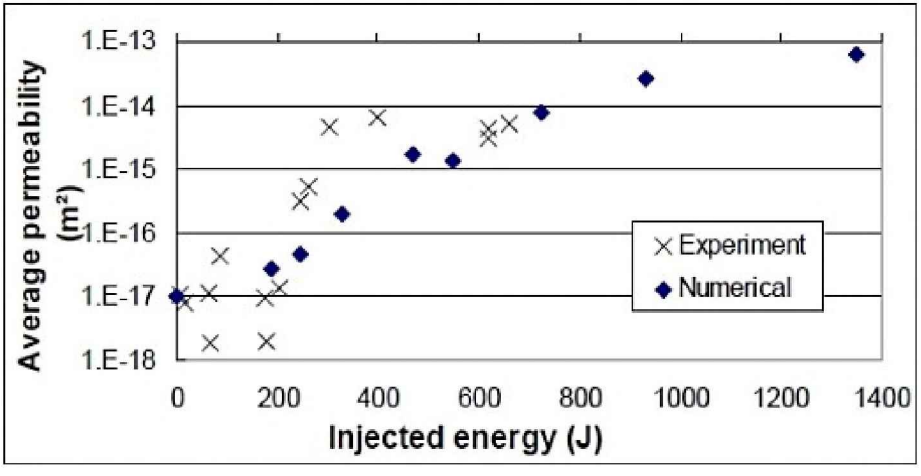

Figure 3.12. *Comparison of the experimental and the numerical average permeability under low confinement*

The evolution of the average permeability of the specimen with the energy injected is shown in Figure 3.12. A very good fit is observed in this figure and therefore it is important at this point to underline the process of calibration of the model parameters:

– The static response of the material has been used in order to calibrate all the coefficients in the mechanical constitutive relations, except the coefficients entering in the rate effect on damage. From the data in Table 3.2, the Young's modulus E, the damage threshold ε_0 governing the elastic behavior, parameter α which controls the strength in compression compared to the strength in uniaxial tension were fitted. In quasi-static tension, there is no prepeak hardening so the value of ε_0 can be directly deduced from the Young's modulus and the tension strength. Then, α is fitted in order to have the correct compression strength. In the absence of data, the Poisson's ratio υ was set to a usual value and the fracture energy of the material was set to 100 N/m, which provides the fracture strain ε_r given a finite element size. The size of the element is taken as the root of its volume, since the mesh is nearly isotropic.

– The two parameters M and n entering into the elastic delay-damage law were calibrated so that the evolution of the intrinsic permeability of the specimen shown in Figure 3.12 fits the experimental data. The parameters entered in the relationship between damage and permeability were those from the literature [JAS 07], and correspond to the fit in Figure 2.12.

The model parameters resulting from this fit are provided in Table 3.3.

Table 3.3. *Calibrated parameters in the damage constitutive model*

ε_0	α	ε_r	υ	M	n
$1.13\ 10^{-4}$	0.2	$2\ 10^{-3}$	0.2	$1\ 10^{-5}$	0.4

Hence, Figure 3.12 ought to be seen as the result of the fit of

the anisotropic damage model against the hydraulic experiments.

It is noticeable that the numerical results exhibit some local irregularity nearby at an injected electrical energy of 500 J. Similar local irregularities are also found under high confinement at a higher energy level. Two concurrent processes are involved: the increase in material damage and the directionality of damage. The slight drop in permeability at about 500 J is due to the increase in ortho-radial damage without an increase in the zone where it develops. The damage zone does not connect the inner and outer faces of the cylinder as shown in Figure 3.11. Therefore, the permeability does not increase a lot and it generated a plateau on the curve in Figure 3.12.

3.2.2. *Numerical results under medium confinement*

Under medium confinement, the specimens are loaded with a vertical stress of 19.5 MPa and a radial stress of 9.1 MPa. This corresponds to an underground depth of approximately 1,500 m for usual tight rocks.

Figure 3.13 shows the distribution of radial damage with the injected energy. This time, and compared to the tests without confinement, large zones with values of damage close to 1 (which correspond to material failure) are observed. These zones are not localized and no macrocracking is observed. Instead, damage seems to be quite well distributed. This is a fundamental difference with static loading in which damage localizes within a small set of macrocracks.

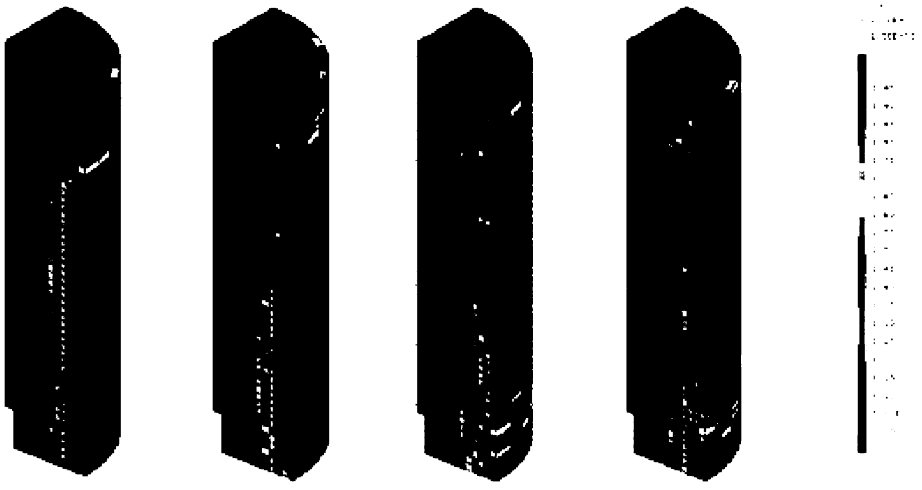

Figure 3.13. *Radial damage upon an increase in injected energy (from left to right: 470 J, 2.24 kJ, 7.1 kJ, 11.4 kJ) under medium confinement. For a color version of the figure, see www.iste.co.uk/pijaudier/drystone.zip*

Figure 3.14 shows the evolution of the maximum principal damage value upon an increase in energy injected. At the highest energy, the specimen seems to be completely damaged (this could not be seen in Figure 3.13 since it represents the principal values of damage separately).

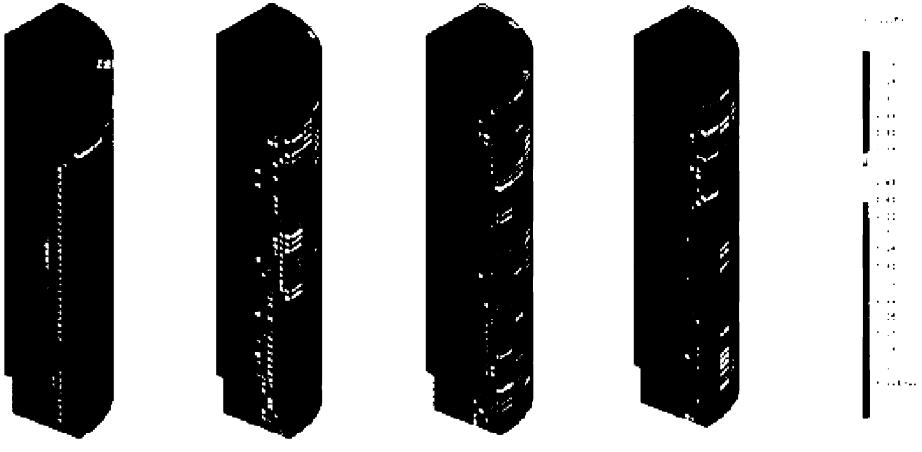

Figure 3.14. *Maximum principal damage upon the increase in injected energy (from left to right: 470 J, 2.24 kJ, 7.1 kJ, 11.4 kJ) under medium confinement. For a color version of the figure, see www.iste.co.uk/pijaudier/drystone.zip*

In most of the calculations, some boundary effect is observed at the top of the specimen. This is probably due to the reflection of the pressure wave in the water, which generates some local amplification of the loading applied to the specimen. Some restraint of the cylinder due to friction with the hydraulic jack on the top might also be responsible for this.

Figure 3.15 shows, for the highest value of injected energy, the development of damage with time. Again, we see the boundary effect as damage initiates near the top surface of the specimen. Then, it propagates at mid height and further expands with time.

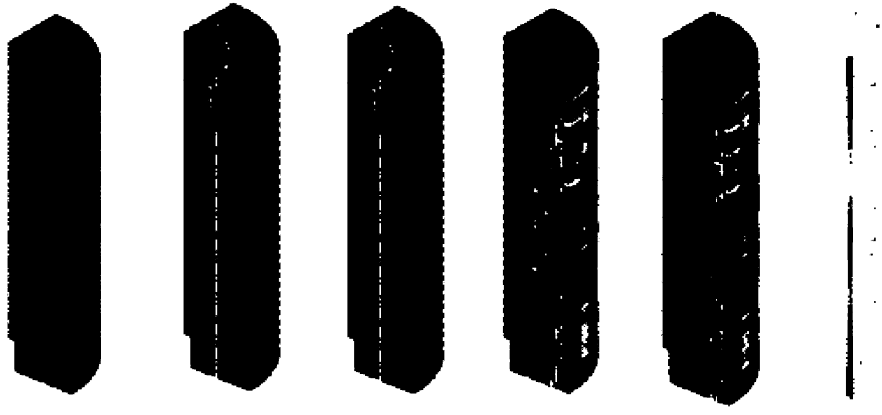

Figure 3.15. *Evolution of the principal value of damage with time under an injected energy of 11.4 kJ (from left to right: 0, 15, 35, 55 and 140 μs) under medium confinement. For a color version of the figure, see www.iste.co.uk/pijaudier/drystone.zip*

The evolution of the permeability of the specimens with injected energy is shown in Figure 3.16.

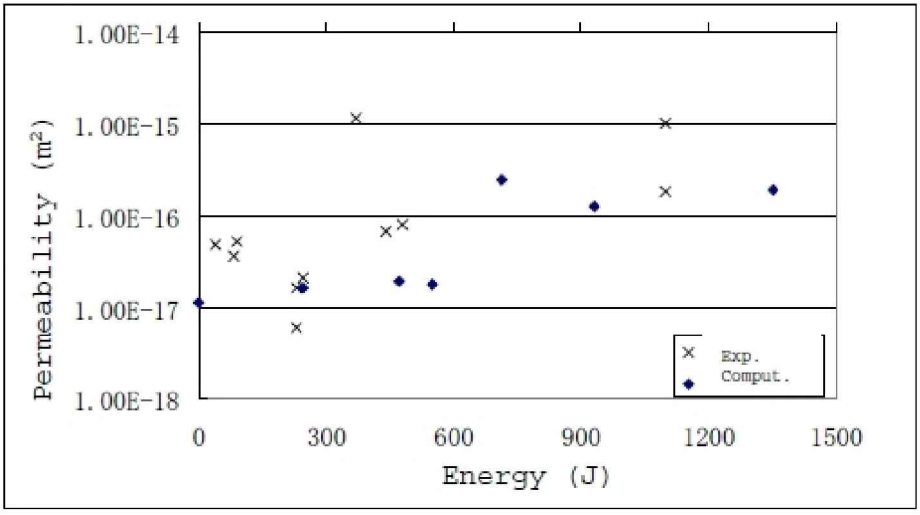

Figure 3.16. *Evolution of the permeability as a function of the injected energy in the case of medium confinement*

Although the experimental data are quite scattered, the calculation falls close to the experimental data. This result is no longer a fit between experimental and numerical data. It is a true prediction, on the basis of the fit obtained without confining stresses.

3.2.3. *Numerical results under high confinement*

Under high confinement, the specimens are loaded with a vertical stress of 40 MPa and a radial stress of 25 MPa. It corresponds to an underground depth of 2,000 m.

Figure 3.17 shows the distribution of radial damage with the injected energy. The distribution of tangential damage is shown in Figure 3.18. This time, tangential and radial damage grow at the same time. Radial damage appears in the central zone mainly and orthoradial damage is located close to the upper face. Again, the boundary effect on top of the specimen is observed; it is the part of the specimen that is the damaged to the greatest extent.

It is easier to consider the largest principal value of damage in order to visualize the damage process. This principal value of damage is shown in Figure 3.19, along with the results of the hydraulic calculation (flux vector). The path of

the flow represents the microcracks and also illustrates their orientation.

It is interesting to see that at some point inside the specimen, the flow becomes vertical and moves upward in order to reach zones of intense damage at the extremity of the specimen. These zones are the result of a complex wave reflection on the upper boundary. Experimentally, it was also observed during the permeability tests that gas leakage (detected using soaped water) was more important near the upper and lower parts of the specimen than in the middle.

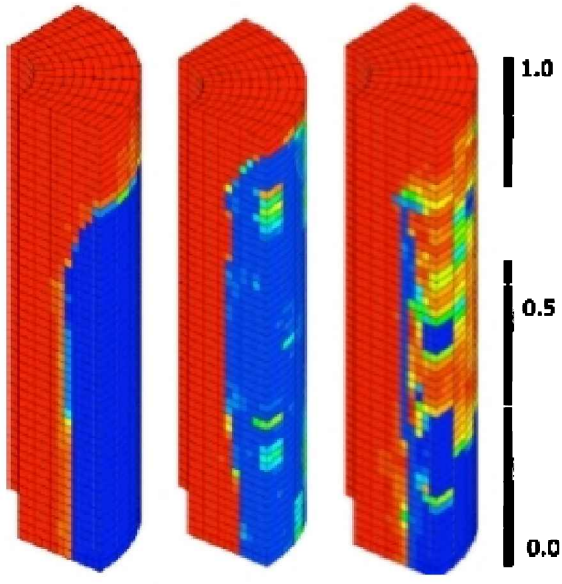

Figure 3.17. *Evolution of radial damage with different levels of injected energy under high confinement (from left to right: 470 J, 5.11 kJ, 11.4 kJ). For a color version of the figure, see www.iste.co.uk/pijaudier/drystone.zip*

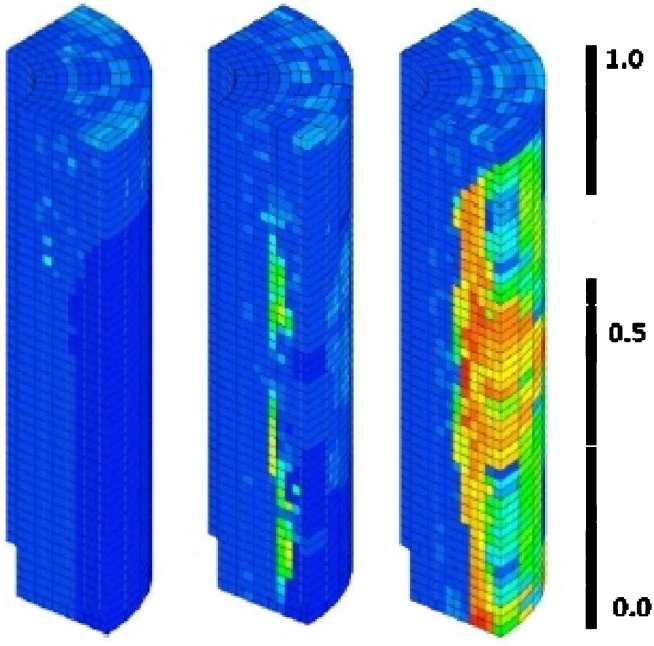

Figure 3.18. *Evolution of tangential damage with different levels of injected energy under high confinement (from left to right: 470 J, 5.11 kJ, 11.4 kJ). For a color version of the figure, see www.iste.co.uk/pijaudier/drystone.zip*

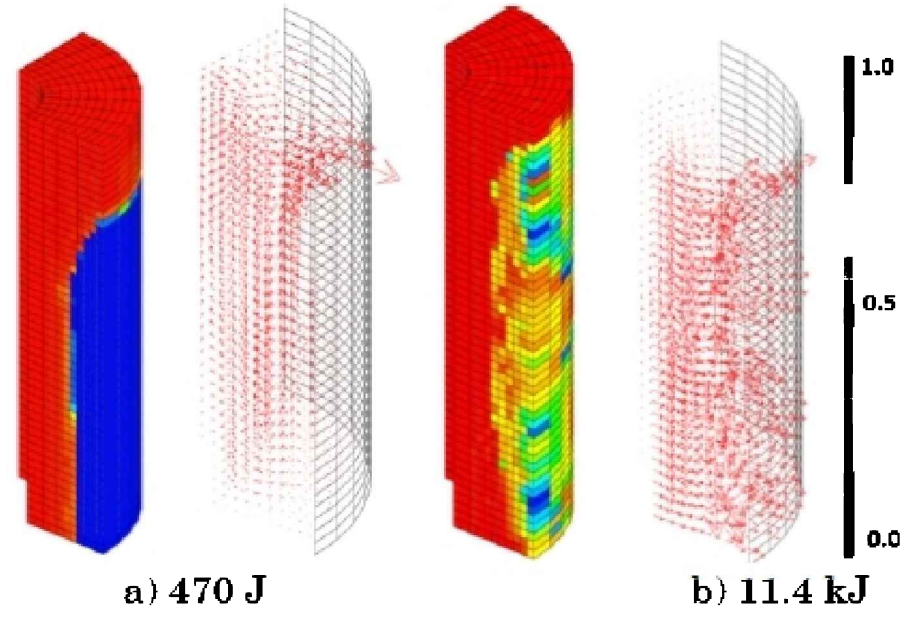

Figure 3.19. *Evolution of damage and flow under different levels of injected energy under high confinement. For a color version of the figure, see www.iste.co.uk/pijaudier/drystone.zip*

The evolution of the average permeability with injected energy is shown in Figure 3.20.

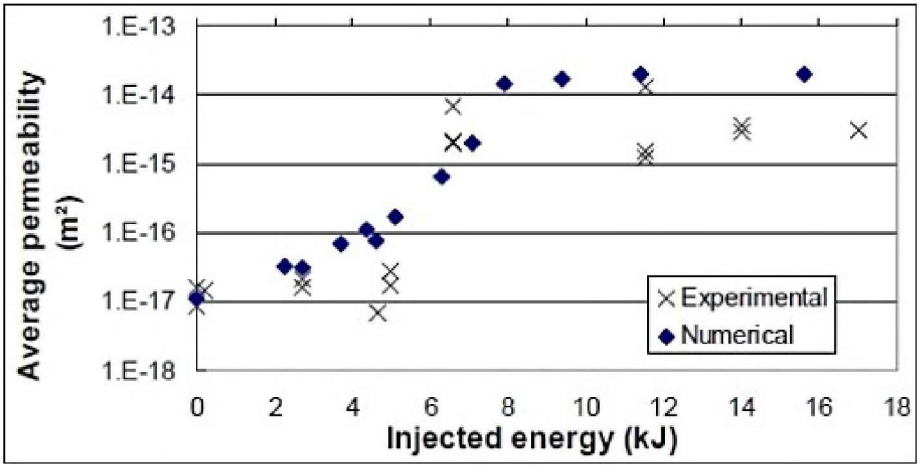

Figure 3.20. *Comparison of the experimental and the numerical average permeability under high confinement with variable injected energy*

A quite good agreement between the calculations and the

experiments is observed. Let us recall that the model parameters have been calibrated based on separate, low confinement tests only.

3.3. Isotropic versus anisotropic permeability

In most approaches in the literature, permeability is isotropic and it is calculated according to the maximum principal damage (or scalar damage, if it is isotropic). Microcracking is, however, directional most of the time and it is interesting to evaluate the simplification induced by considering that permeability is isotropic. Typically, the above distributions of damage exhibit a directional fluid path that cannot easily be represented by isotropic permeability. Hence, noticeable differences between the isotropic and anisotropic descriptions of permeability should be expected.

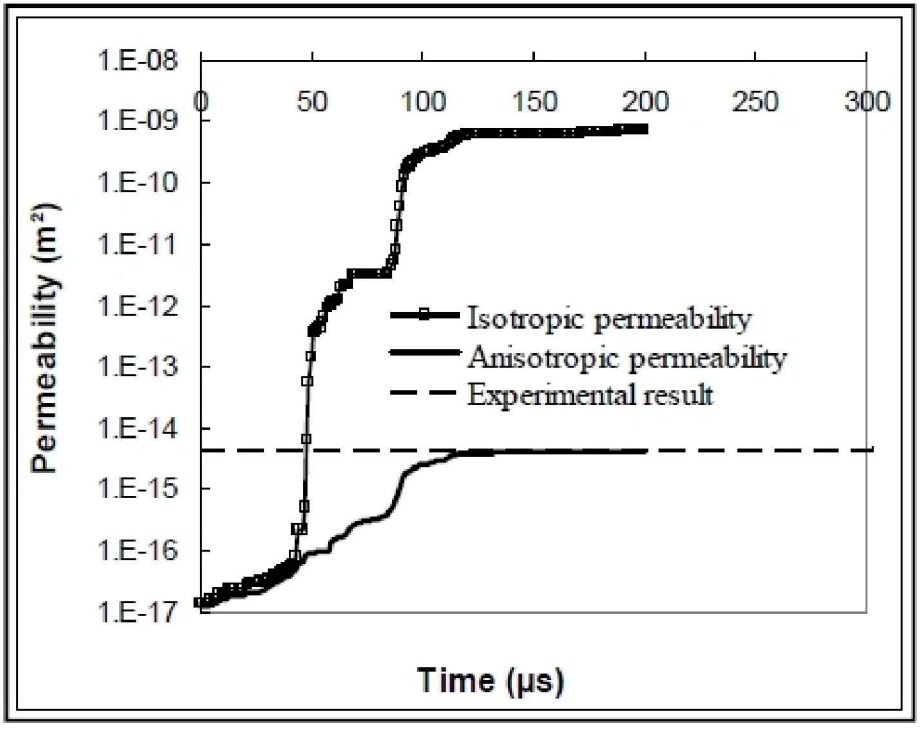

Figure 3.21. *Variations in average isotropic and anisotropic permeability of the specimen over time while under transient load*

Let us consider the case of one shock with an injected energy of 11.4 kJ under high confinement. In the isotropic case, the material's permeability is computed according to equation [2.26]. It is calculated from the maximal eigenvalue of the damage tensor. In the anisotropic case, the permeability is computed from the eigenvalues of the damage tensor according to equation [2.27]. Note that the parameters used in the calibration of the damage–permeability relationship, which are those in the literature, correspond to a permeability measured in the axial direction of uniaxial compression specimens. This is the permeability measured in planes parallel to the microcracks. In this specific case, the isotropic and anisotropic approaches provide exactly the same variation in permeability in the direction of the uniaxial load.

The average permeability of the specimen is overestimated in the isotropic case compared to the anisotropic case

(Figure 3.21). In the calculation with anisotropic damage, the central zone of the mortar specimen is affected by radial damage, whereas the rest of the specimen is affected by orthoradial damage. In the isotropic case, these two systems damage of are equivalent and radially connected to each other, since directionality is lost. The case of high confinement maximizes this difference: the fluid flow predicted by the anisotropic case is not radial, whereas it is assumed to be radial in the isotropic case. Therefore, the flows calculated using the isotropic and anisotropic methods are very different. Losing the effect of the directionality of damage on the permeability yields a severe overestimation of the overall permeability.

3.4. Conclusions

In this chapter, uniaxial experiments and tests on hollow cylinders have been compared to computations. The major purpose was to evaluate the capacity of the computational model to capture the main features of the experiments, that is the growth of permeability with increasing electrical energy inserted into the system. The model calibration has been carried out using a small set of experiments and comparisons with further simulations on the rest of the data provided some evaluation of the quality of the finite element model.

Although the model provides rather detailed damage maps, they could hardly be compared to any experimental data. They are highly heterogeneous and agree, in some instances, with some X-ray data qualitatively. The most demonstrative and quantitative evaluation has been provided by the evolution of permeability with increasing electrical energy. The model predictions turn out to be quite representative of what is observed experimentally. Such an agreement opens the way toward further computations, including those on repeated shocks that seemed to be quite effective as far as the increase in permeability could be observed experimentally. These computations, along with some others based on representative reservoir geometries, are going to be discussed in Chapter 4.

4
Computations on Representative Reservoir Geometries

Before we examine the capabilities of electrohydraulic fracturing on representative geometries, we will start with the investigation of the effect of repetitive shocks. The increase in permeability with the number of shocks of moderate amplitude of pressure (below the damage threshold) is a feature that could be considered unexpected. Indeed, the process looks experimentally to demonstrate some fatigue with very few cycles below or at the damage initiation amplitude, whereas the numerical model – and the constitutive relationship used for the solid material, does not incorporate fatigue at all.

Then, we will turn toward simulations using representative reservoir geometries. Here, we will look at the extent of the damage zones only. We will not perform calculations of the evolution of permeability of the reservoir. Let us recall that a small increase in damage, e.g. 20%, yields an increase in permeability over a decade.

After an evaluation of the range of propagation of damage in the context of single shocks, we will look at an optimization of the process, essentially at the effect of guided pressure waves. Finally, we will investigate the influence of the shape of the pressure wave on the extent of the damage. The idea is to optimize the form of the pressure wave to be generated.

4.1. Effect of repeated shocks

In order to investigate the effect of repeated shocks, we considered the experiments on hollow cylinders under high confinement. We are going to use the same numerical model as in Chapter 3, with the same material parameters, and consider the case of high confinement.

In the continuum damage relations used for the solid phase, if the threshold of damage is not reached, then microcracking cannot appear. This is similar to an endurance limit in fatigue. The tests reported in Chapter 1 exhibit a growth of damage and permeability in the specimens, even if the pressure wave yields some variation of damage and permeability that cannot be detected. We are going to use the same conditions: the energy injected in the computation is 2.7 kJ, slightly above the threshold of damage.

Figure 4.1 shows the cumulated history of energy injection. Sufficient time is left in between each injection of energy to prevent the successive pressure waves interacting with each other. Each pressure wave is attenuated upon several reflections and the amplitude is so small that it does not interfere with the next one.

The analysis is performed by looking at the variation in the permeability of the specimen after each shock. Figure 4.2 shows the evolution obtained numerically. Only three shocks have been applied. Compared to the experiments, the increase in permeability is larger according to the numerical simulations (see Figure 1.7). Note that the numerical data for a single shock already overestimated the variation of permeability (Figure 3.20). Therefore, it is not surprising that for repeated shocks the increase in permeability becomes greater than in the experiments.

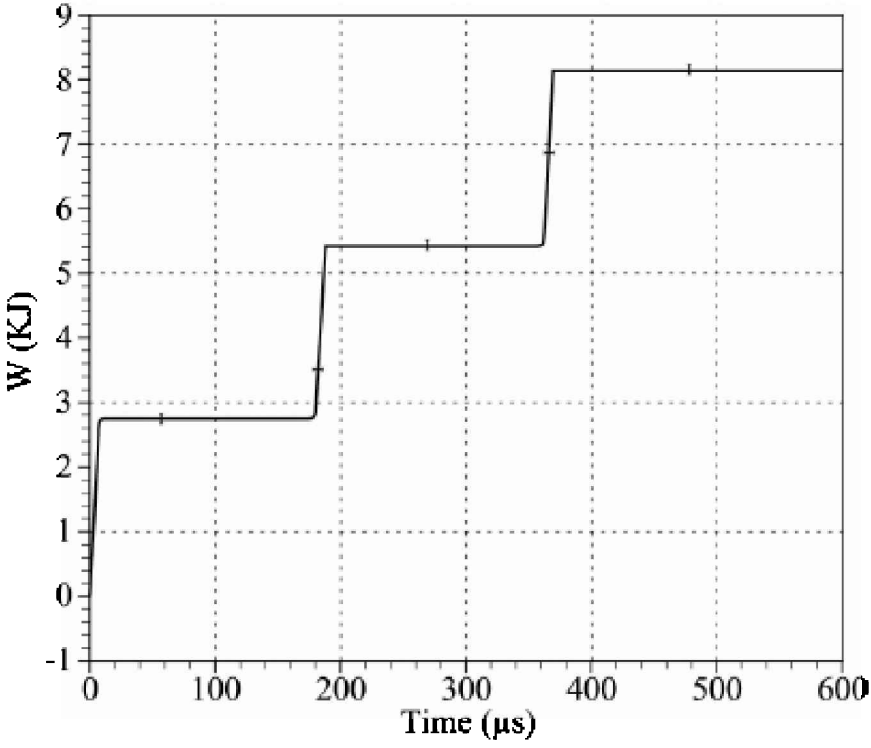

Figure 4.1. *The cumulative effect of energy injections over time*

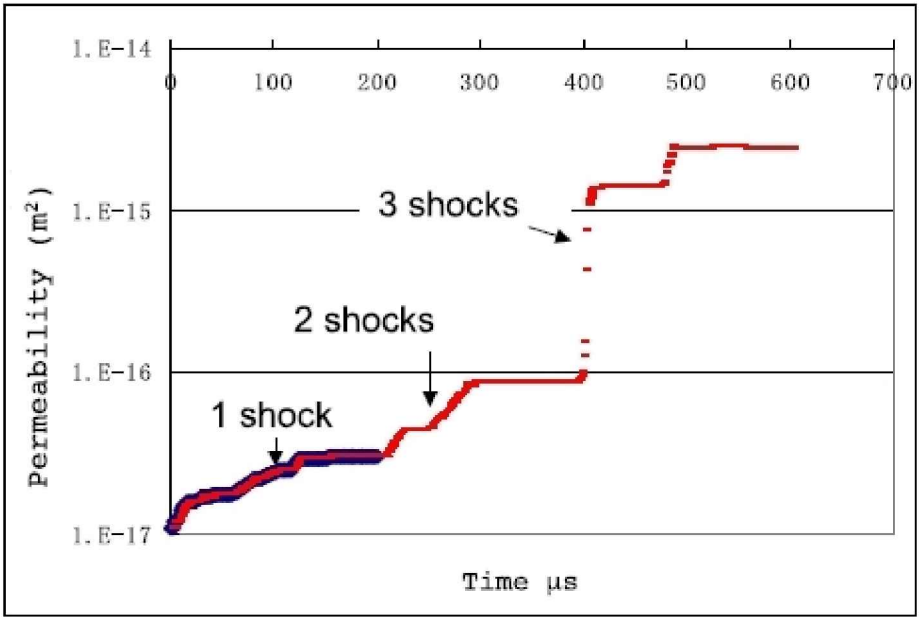

Figure 4.2. *Evolution of damage with the number of shocks under high confinement*

A feature that is recovered according to the numerical model is the increase in permeability upon repeated shocks. In the context of time-independent or rate-dependent damage and without interactions in between the successive pressure waves, the maximum damage would be reached after the first wave is applied. Indeed, if we expect the strain history to be exactly the same for each shock, the subsequent waves should propagate elastically and the domain of reversibility should not change, yielding a linear response of throughout the material.

According to the calculations in Chapter 3, radial damage occurs when this level of energy is injected. Tangential damage is almost negligible. Once a first shock has occurred, the second one induces a compression wave in the damaged material. Due to the closure of microcracking that is implemented in the constitutive relationships, damage has no effect on compression and the second wave may propagate whatever the state of damage, as if it was the first loading the specimen has been under. Then, wave interaction (e.g. between waves in water and in the specimen) develops and damage increases. This growth of

damage is rather a complex process over time and it is difficult to figure out but there is one feature in the constitutive model without which an increase in damage with repeated shocks could not occur: without taking into account the stiffening of the material upon crack closure, compressive waves would not be efficiently transmitted in the specimen, the decrease in stiffness inducing a decrease in the velocity of the pressure waves.

It follows from this calculation that the computational model seems to be capable of capturing the effect of repeated shocks. It is this process which seems to be more adequate in practice. Damage and permeability increase after each shock and therefore can be controlled as opposed to the case of a single shock with a much larger amount of energy. Besides, this methodology would optimize the process. Because the electrical energy at stake is much lower, smaller electrical capacities would be needed. Since we would probably be required to place some of these capacities near the electrodes, down in the well to be stimulated, the design of such capacities should be more convenient in the context of a severe and constrained environment.

4.2. Simulation on a typical reservoir geometry

We are going to turn now to simulations on a geometry that is representative of a reservoir with a vertical well. In order to minimize the size of the finite element model, we only represent one horizontal layer of the rock mass: it is a circular zone 16 m in diameter and 2.5 m thick. The borehole diameter is 10 cm.

Figure 4.3 shows the finite element mesh used, the dark zone being the borehole filled with water at ambient pressure. For reasons symmetry, only a quarter of the model is represented.

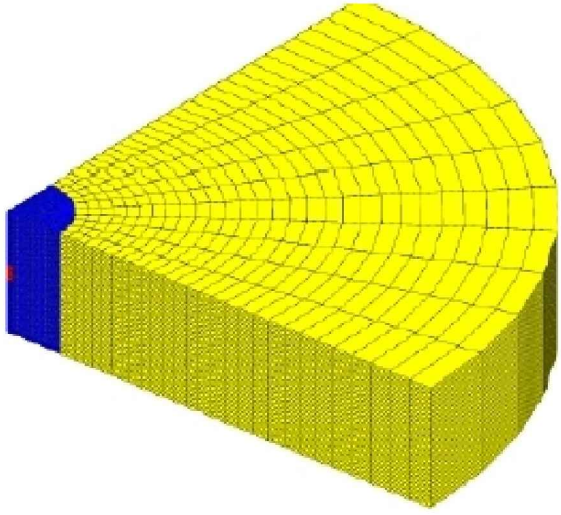

Figure 4.3. *Finite element mesh for the analysis of a representative reservoir geometry*

Medium confinement corresponding to a reservoir depth of 1,500 m is applied and considered constant throughout the thickness of the model. The pressures corresponding to the vertical stress are applied on the top and bottom faces and the horizontal confinement stress is obtained by applying pressure on the outer surface of the cylindrical zone. The electrodes are so small that they are not explicitly described. Energy is inserted in a small region at the center and mid-height of the borehole, filled with water and remains tight during wave generation. For the sake of simplicity and comparisons with the previous results discussed in this book, the material parameters entered in the constitutive relations for the solid and liquid are kept the same as in Chapter 3 (see Table 3.3).

Computations were first performed in the case of a single of energy shock 450 kJ repeated several times. This is 40 times the energy used in the experiments. Figure 4.4 shows the distribution of damage after a single shock. For the sake of readability, the damaged elements have been extracted from the mesh and are shown in Figure 4.4 (b).

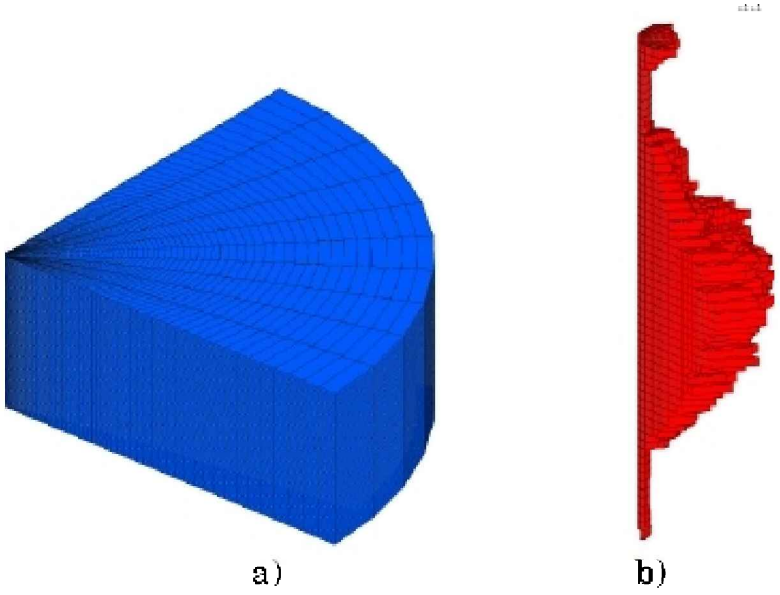

Figure 4.4. *Damage due to a single shock under medium confinement*

Figure 4.5 shows the radial depth of penetration of damage inside the reservoir as a function of the energy injected. These calculations have been performed for increasing levels of energy. From a practical point of view, electrical engineers believe the energy that could be transported inside the borehole at a depth of about 1,500 m should be in the range of a few MJ. Consequently, for this energy, the depth of penetration should be slightly above 50 cm for a single shock.

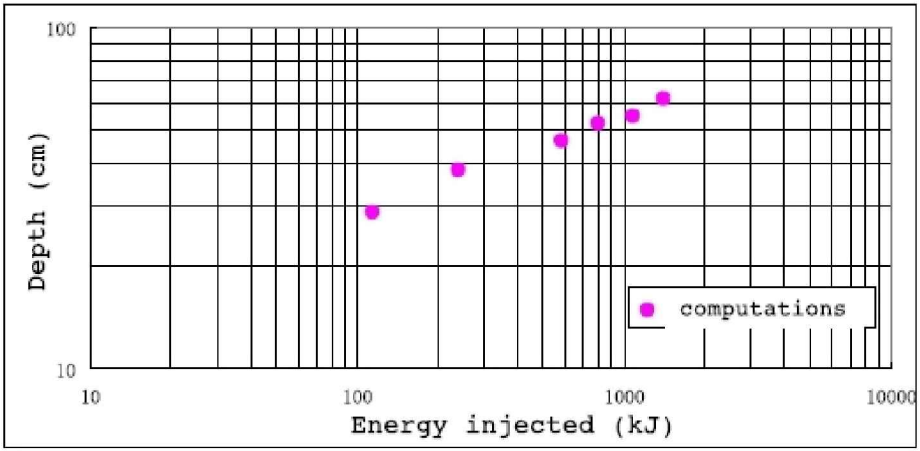

Figure 4.5. *Radial depth of penetration of damage in the reservoir as a function of the injected energy for a single shock*

Repeating the shocks should extend the damage zone and increase the radial depth of penetration of damage. This is shown in Figure 4.6 in the case of two successive shocks 450 kJ amplitude. We may observe that the depth increases by 40% after the second shock. Subsequent calculations reveal, however, that the radial depth of damage inside the reservoir tends to stabilize after a small number of shocks In the present case, after three shocks it becomes almost constant, at less than 1 m.

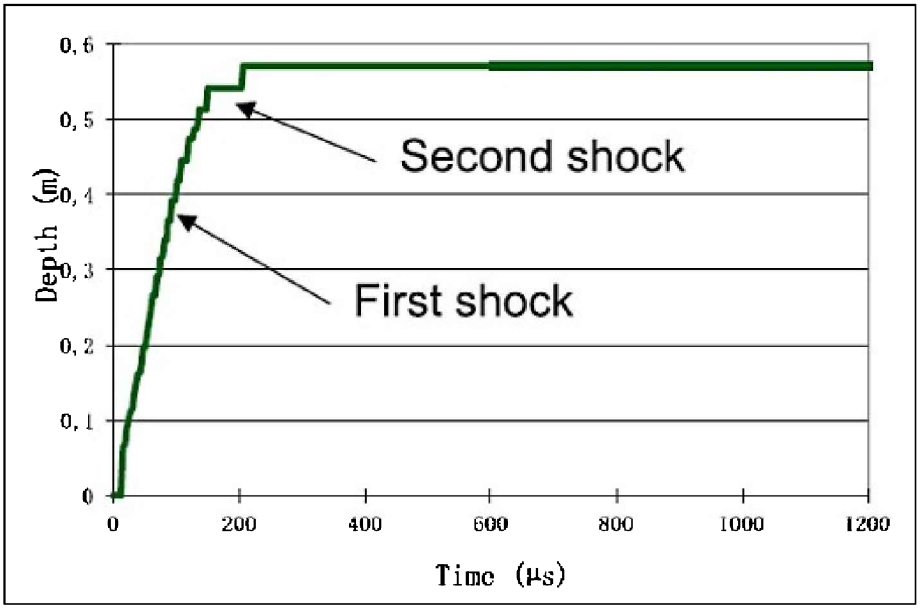

Figure 4.6. *Influence of a second shock on the radial depth of penetration of damage*

These calculations demonstrate that in spite of the efficiency of the process at increasing damage around the borehole, the damaged zone remains rather small. If we compare this with classical hydraulic fracturing in which cracks may propagate over several hundreds of meters, the stimulated volume in the case of electrohydraulic fracture is two orders of magnitude less in terms of distance from the borehole. We should note, however, that the distribution of fractures is totally different in electrohydraulic fracturing compared to hydraulic fracturing. In electrohydraulic fracturing, damage is distributed and it is the entire volume around the borehole that experiences an increase in permeability. This is not the case in hydraulic fracturing, where only a small set of cracks propagates. Even if these cracks are long, they propagate in a region whose permeability is not much changed.

In terms of surfaces of exchange for hydrocarbon extraction with sufficient permeability, electrohydraulic fracturing induces a gradient of permeability that increases toward the borehole. It is difficult to figure out the total surface of exchange (i.e. the microcrack surfaces) generated

dynamically, but a rule-of-thumb approximation would be that they should be comparable to those generated under hydraulic fracturing if the energy at stake in the fracturing process is comparable. This estimate relies on the condition of propagation of a Griffith's crack. The connection of these surfaces with the non-stimulated part of the reservoir, however, is much smaller than with hydraulic fracturing. Increasing this surface means that the depth of penetration of the damage zone around the borehole should be increased, say by one order of magnitude, before this process can be implemented in practice. Therefore, it needs to be optimized, and it is the purpose of the next section to consider several possible methods.

4.3. Optimization of the process

Two methods for the of optimization of electrohydraulic fracturing are going to be considered: the first one deals with the nature of the pressure waves and aims to decrease the attenuation of the pressure amplitude during the propagation. In the second one, we will look at the influence of the shape of the pressure wave.

4.3.1. *Decreasing the attenuation*

The rather limited extension of the damage zone could have been foreseen as we have not set up the best possible conditions for the optimum propagation of energy in the reservoir. Although the pressure wave is not spherical in water confined in the borehole, it is almost spherical in the reservoir under the assumption that the reservoir is large enough (which is not really the case in our calculations over a layer of finite thickness with reflection of the wave on the top and bottom faces of the model). The elastic energy carried by the pressure wave is distributed in a growing volume as it propagates. The volume increases with the distance to the centre of the borehole by a power of 3. Therefore, the amplitude of the pressure decays rapidly, and the pressure quickly becomes too low to generate any damage.

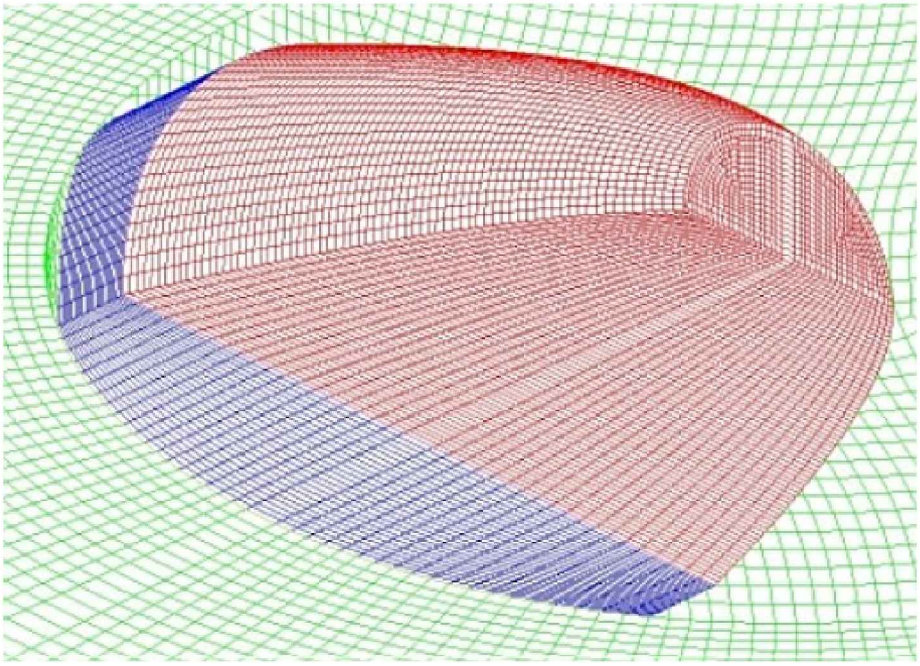

Figure 4.7. *Wave reflector – parabola with a symmetry of revolution. For a color version of the figure, see www.iste.co.uk/pijaudier/drystone.zip*

One way of avoiding such a decay is to transform the spherical wave into a quasi-planar wave. This is feasible, at least in a computational setting, and should be done before any practical issue can be tackled.

A rigid reflector is placed in the borehole. The shape of the reflector is a parabola with a symmetry of revolution around the axis of propagation of the pressure wave. Energy is inserted at the focal point of the parabola and therefore the pressure wave generated is converted into a planar wave upon reflection. Figure 4.7 shows the shape of this reflector, placed inside the borehole.

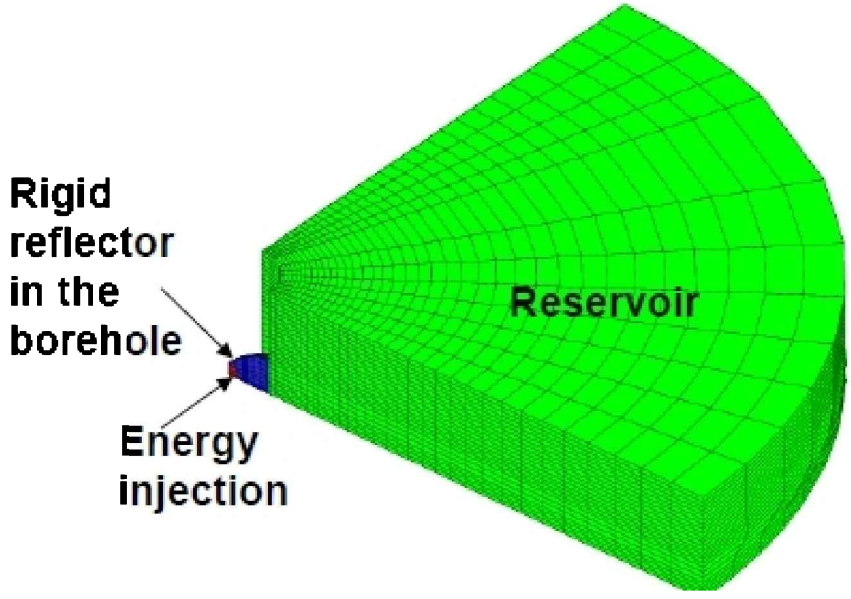

Figure 4.8. *Finite element mesh with a reflector*

In order to carry out the calculations, the reflector is added in the finite element mesh as shown in Figure 4.8. Water is placed inside the reflector, which is again treated as being infinitely rigid, as a first approximation.

Figure 4.9 shows the distribution of damage obtained after a shock with 400 kJ energy. In this example, the confinement is zero (no external stresses are applied on the model).

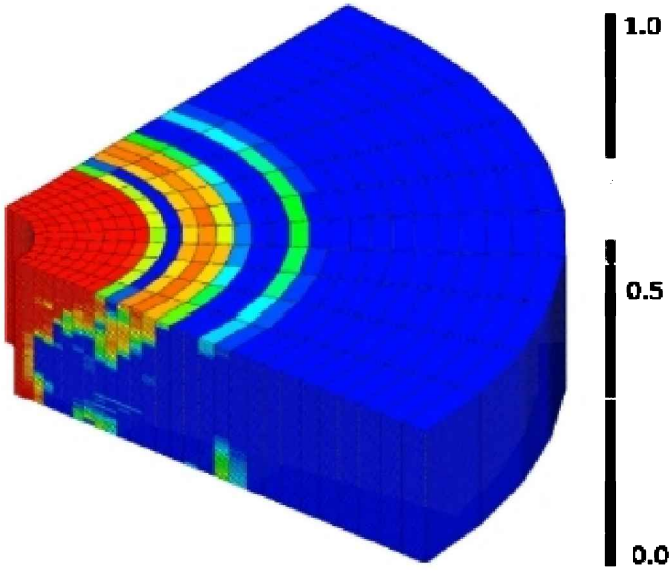

Figure 4.9. *Distribution of damage (maximum principal damage) for an injected energy equal to 400 kJ. For a color version of the figure, see www.iste.co.uk/pijaudier/drystone.zip*

Large damage values (dark gray) are observed within a 50 cm radius of the borehole. Figure 4.10 shows the same calculation performed with a reflector.

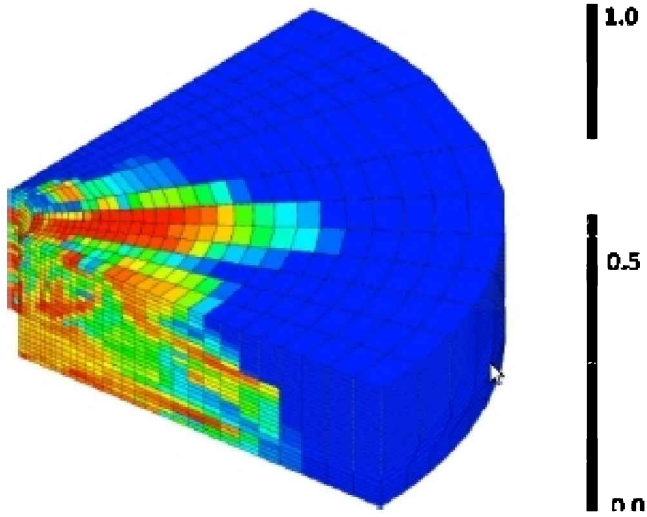

Figure 4.10. *Distribution of damage (maximum principal damage) for an injected energy equal to 400 kJ with a wave reflector. For a color version of the figure, see www.iste.co.uk/pijaudier/drystone.zip*

The comparison between Figures 4.9 and 4.10 shows that the radial extent of the damage zone is multiplied by approximately two, if a wave reflector is placed in the borehole. In these calculations, the diameter of the borehole has been increased from 10 to 50 cm in order to place the reflector in the mesh. This should not be seen as limitation: the larger the diameter of the borehole, the easier it would be to place. In comparison with the calculation in the previous section, increasing the diameter of the borehole by a factor of five decreases the efficiency of the process in terms of extent of the damage zone in the reservoir by 36%.

4.3.2. *Influence of the wave form*

Up to now, the form of the pressure wave has been generated by inserting energy in the interelectrode space. Depending on the time-history of injection, the interelectrode space and the shape of the electrodes, the waveform changes. Therefore, it is interesting to analyze what the main factors in the waveform would be that may yield a better efficiency.

In order to do this, we will consider the parametric

description of the waveform depicted in Figure 4.11. It is a trilinear function of time, with a linear increasing ramp, a plateau and a linear decrease. The maximum pressure is P_0.

This parametric function is defined with three characteristic time durations:

$$p(t) = tP_0 if t < T_r p(t) = P_0 if T_r \le t \le T_w \quad [4.1]$$

$$p(t) = P_0 \frac{T_f - t}{T_f - T_w} if T_w \le t \le T_f \text{, and } p(t) = 0 if t > T_f$$

T_r is the ramp time, $(T_w - T_r)$ is the duration of the pressure plateau and T_f is the total duration of the waveform.

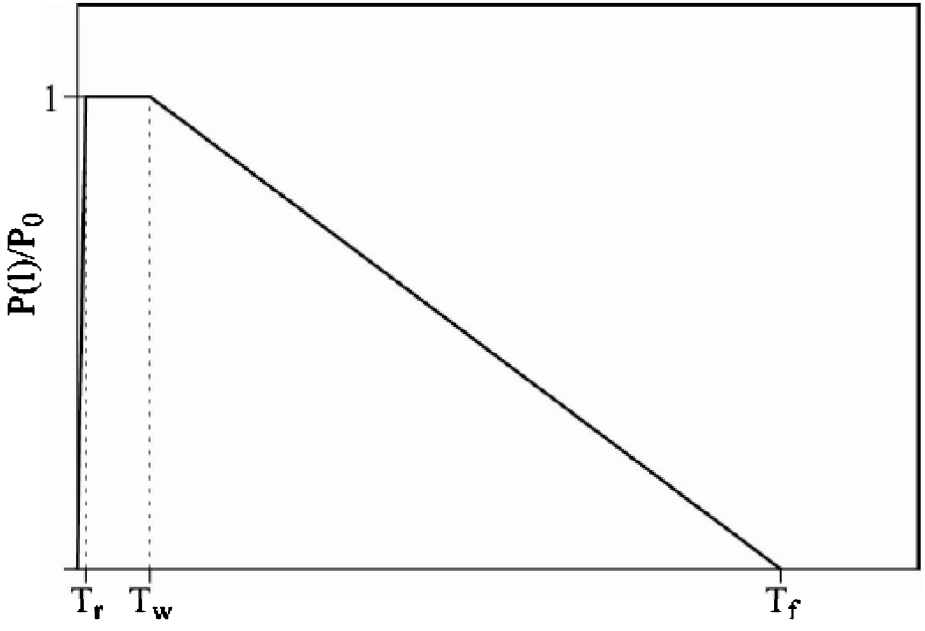

Figure 4.11. *Parametric waveform generated on the surface of the borehole*

Parametric calculations have been conducted on a simplified finite element model shown in Figure 4.12. It is a plate 10 cm thick, with a diameter of 10.1 m (the borehole diameter is 10 cm). The pressure waveform is applied directly onto

the inner surface of the borehole. The amplitude of the pressure wave P_0 is set such that the diameter of the damage zone is in the range of 50 cm. We are going to analyze the results in terms of extent of damage, i.e. the largest distance from the borehole center to a finite element which has encountered damage.

Table 4.1 gives the various values of the characteristic times considered for this parametric study. These times fall within the range of what can be expected to be technically feasible through the process of arc electrical discharge in water.

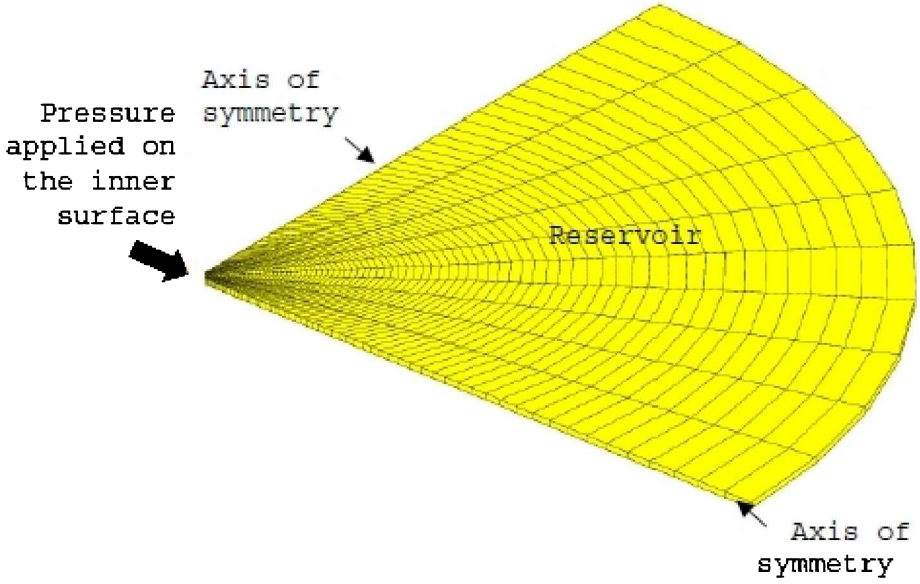

Figure 4.12. *Finite element mesh used for the study of the influence of the waveform*

Table 4.1.*Characteristic times considered for the parametric study*

T_r	$T_w - T_r$	$T_f - T_w$
100 ns	1 µs	10 µs
1 µs	10 µs	100 µs
10 µs	100 µs	1 ms

Let us start with the influence of the ramp with a duration of T_r . Figure 4.13 shows the calculations performed for several

values of T_r , keeping the two other characteristic times constant ($T_w - T_r$ = 100 µs, and $T_f - T_w$ = 10 µs). The trend is that the shorter the time it takes to reach the pressure plateau, the greater the extent of damage is.

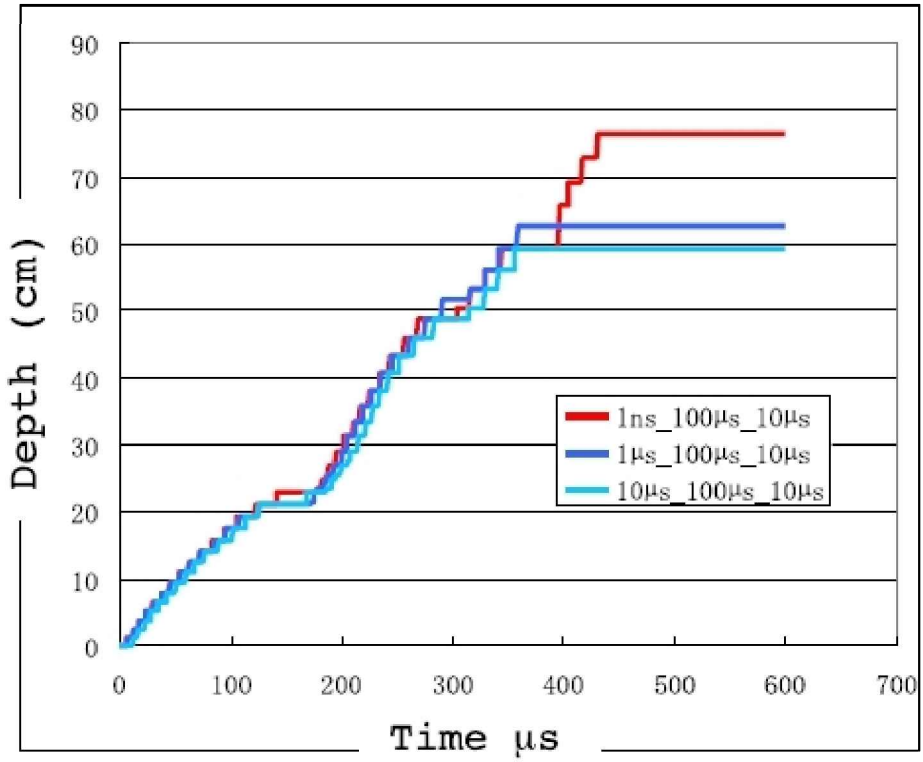

Figure 4.13. *Influence of the rising time in the waveform on the extent of damage. The curve with the higher plateau corresponds to the shortest rising time and the curve with the lower plateau corresponds to the longest rising time*

Figure 4.14 shows the influence of the duration of the pressure plateau. The rising time is kept constant (T_r = 1µs) and the decaying time lapse is also constant ($T_f - T_w$ = 10 µs). The duration of the plateau spans from 1µs to 10µs. We may observe that the duration of the plateau has a very large influence on the extent of damage. When the duration is decreased, the extent of damage decreases by a factor of three within the time range considered.

Figure 4.15 shows the influence of the decaying time of the

waveform. The rising time is set constant (T_r = 100μs) and the duration of the plateau is also constant (100 μs).

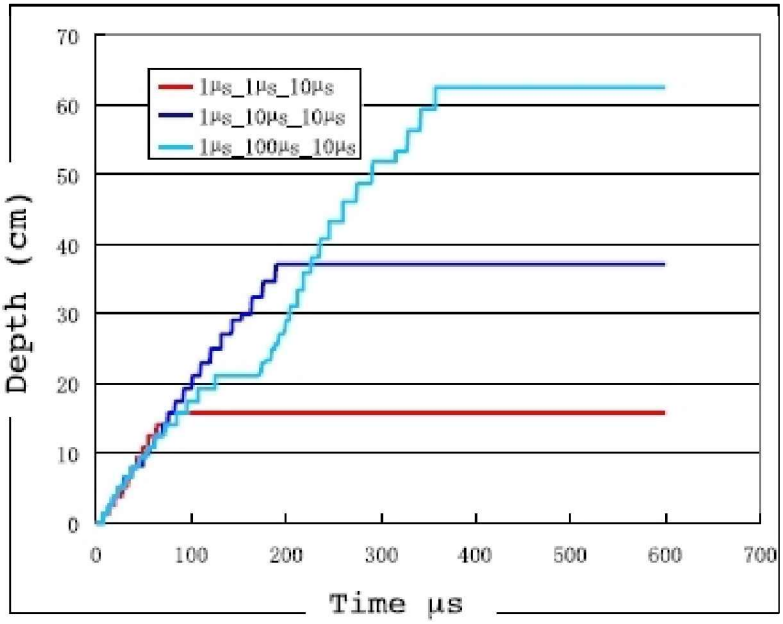

Figure 4.14. *Influence of the duration of the plateau in the waveform on the extent of damage. The curve with the higher plateau corresponds to the longest duration and the curve with the lower plateau corresponds to the shortest duration*

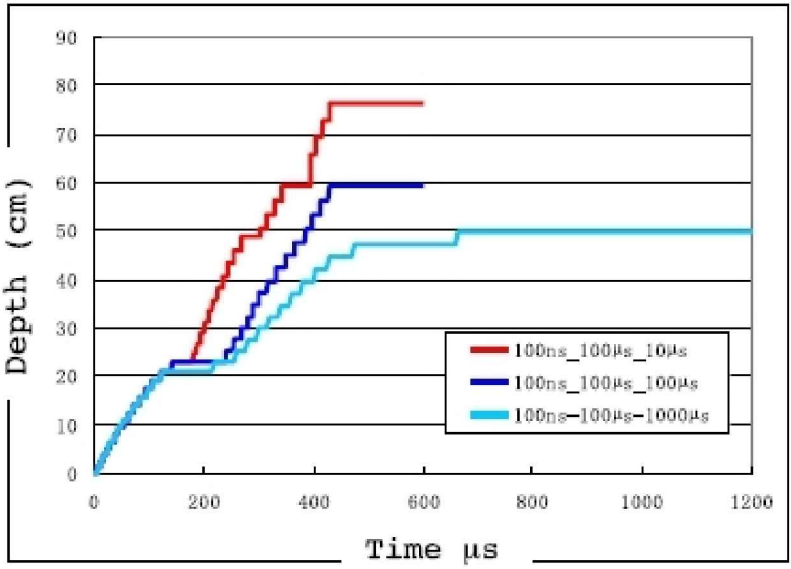

Figure 4.15. *Influence of the decaying duration of the waveform on the extent of damage. The curve with the higher plateau corresponds to the shortest duration and the curve with the lower plateau corresponds to the longest duration*

We may observe that this time the extent of damage increases as the decaying time becomes shorter.

Table 4.2. *Parametric study of the influence of the waveform on the extent of damage*

Rising time (µs)	Duration of plateau (µs)	Decaying time (µs)	Extent of damage (cm)
		Reference values	
1	10	100	50.29
		Parametric study	
0.1	1	10	15.42
0.1	10	10	34.61
0.1	100	10	65.79
0.1	1	100	44.75

0.1	10	100	50.29
0.1	100	100	59.31
0.1	1	1,000	49.92
0.1	10	1,000	47.21
0.1	100	1,000	49.92
1	1	10	15.75
1	10	10	37.03
1	100	10	62.49
1	1	100	44.75
1	100	100	56.29
1	1	1,000	41.21
1	10	1,000	41.21
1	100	1,000	49.92
10	1	10	25.54
10	10	10	44.75
10	100	10	59.29
10	1	100	48.78
10	10	100	56.19
10	100	100	62.49
10	1	1,000	39.46
10	10	1,000	41.99
10	100	1,000	49.92

To summarize this parametric analysis, the most efficient waveform is the one that has a very short rising time followed by a long plateau of constant pressure and then a short decaying time, although the precise influence of this duration is not very clear in each calculation. This is illustrated in Table 4.2, where the extent of the damage zone for each set of data is provided. Furthermore, this is consistent with existing results from Cho and Kaneko [CHO 04].

On the basis of this parametric study, specific developments should be expected on the electrical part of the set-up in order to optimize the efficiency of the electrohydraulic process.

Concluding Remarks and Future Outlook

This book has reported on a study aimed at developing what could be a potential alternative to hydraulic fracturing. The principle of this technique relies on the effect of dynamic loading on quasi-brittle materials such as rocks: in dynamics, there is seldom a single fracture and multiple cracking or fragmentation of the material should be expected. It is on the basis of this physical property that we started to design the electrohydraulic fracturing of rocks. Instead of using blasting and explosives, we turned toward dynamic loads generated by a PAED in between two electrodes placed in a borehole filled with water. This technique provides some control of the dynamic load to be applied, and at the same time loads can be repeated as many times as necessary, quite easily.

After a feasibility study on a very simple set-up, experiments were conducted using a geometry that is close to the surrounding of a borehole and various confinement levels corresponding to various depths have been tested. Each specimen, made of a mortar which has similar properties to tight rocks and sandstone cores, followed a workflow composed of X-ray scanning, measurement of permeability, application of dynamics loads, and then X-ray scanning and remeasurement of permeability in order to characterize differential properties (before and after the shock). Tests using dynamic loads with increasing maximum pressure and repeated loads at moderate pressure levels were conducted and they exhibited the same trends:

– Tests with single shocks and variable energy levels show that there are thresholds of injected energy wave above which damage and increase in permeability are observed. This threshold increases with the confinement stress on the specimen.

– Results from repeated shock tests show that the

permeability increases with the number of shocks, even if a moderate electrical energy corresponding to the damage threshold has been used. An accumulation of damage as a function of the number of shocks is observed.

– In both types of tests, the permeability measured on unloaded specimens increases by two orders of magnitude, at least.

– X-ray tomography shows that the surface area of cracks induced by the dynamic loads increases both with injected electrical energy and with the number of shocks. X-ray tomography also shows that many cracks develop in the course of the experiments. Most specimens did not exhibit visible cracking at the end of the tests; only those carried out at high energy levels or larger number of repeated shocks exhibited some visible macrocracking.

– Mercury intrusion porosimetry also provided some information about the evolution of pore size distributions. The proportion of small pores decreases while that of large pores increases upon damage, which is consistent with measurements of permeability as shown later by Khaddour *et al.* [KHA 15].

Since this experimental study, attention has been focused on the development of a numerical simulation technique of this process. It relies on the implementation of several ingredients in an explicit finite element code:

– First, the pressure wave generation is simulated by the injection of energy in water, in between the two electrodes. This method is rather simple to implement in a hydrodynamic computational scheme. Energy induces a phase change of water from liquid to vapor. The fluid is modeled in the numerical technique as two-phase mixture, and follows the saturation curve in the thermodynamic table of water. It is this sudden phase change that induces a pressure wave, which propagates further into liquid water.

– The constitutive relations for the solid phase of the

model (mortar in the experiments and rocks) rely on a continuum damage-based approach. The influence of microcracking is captured by a second-order tensor with principal values ranging from zero for a virgin material to 1 for a completely cracked material. This variable degrades the stiffness of the material. Damage, being directional, induces elastic anisotropy. The stiffness recovery of the material upon closure of microcracks is also captured. Finally, the loading being dynamic, rate effect on damage growth is also implemented. The model parameters can be fitted using standard properties of the material (elastic constants, tensile and compressive strength in the quasi-static regime, and fracture energy), and from data available in the literature, as far as the increase in the material strength with the strain rate is concerned.

– Finally, the evolution of permeability is coupled to the growth of damage. The damage and permeability variables are second-order tensors with the same principal directions. The intrinsic permeability of the material in one direction is a function of the maximum damage parameters in the plane orthogonal to this direction. The model parameters entered in the formula controlling the growth of permeability with damage have been taken from the literature.

Once these features were folded in a finite element code, we were able to reproduce the experiments reported previously. Fitted on tests carried out without confinement, the extrapolation to two confinement levels exhibits a good agreement between the experimental and numerical evolution of the average permeability of the specimens with the level of injected electrical energy. Furthermore, the effect of repeated dynamic loads at moderate levels (i.e. slightly above the threshold of damage) provides the same qualitative trends as in the experiments.

Considering this result, we decided that the numerical model could be accurate enough to start computations on representative reservoir geometries. These computations quickly exhibited the limit of electrohydraulic fracturing: the

damage zone around the borehole is confined to within a meter or so if the electrical energy to be injected stays in a range where on-site implementation is technically feasible. This is due to the important attenuation of the propagating wave.

Several directions of optimization have been considered. The first one is to focus the wave and to transform it into a quasi-planar wave. Attenuation is reduced and the extent of the damage zone can be almost doubled according to the computations. The second one relies on a parametric study of the form of the pressure wave to be generated by PAED. It turns out that the gratest efficiency is reached for a waveform with short rising time, a long plateau at maximum pressure, and a sharp decrease in pressure. Again, within the bounds of what would be expected to be feasible in practical cases, the extent of the damage zone could be increased by as much as 20 or 30%.

These optimization directions require some experimental validation. Still, if the extent of the damage zone is expected to be in the order of 10 m before the process can be considered to be of some practical interest, some efforts are needed as, being optimistic, today the extent of damage around the borehole is in the 2–4 m in range.

Some other directions of optimization could also be considered, such as the generation of several waves that may interact and produce a very high pressure locally. What is probably the most effective direction, however, would be to combine electrohydraulic fracturing with hydraulic fracturing. This combination has been the subject of an international patent in the context of gas production from shales. By increasing the fluid pressure in the reservoir, we might expect a local relief of confinement stresses on the solid phase. Experiments under low confinement show that the efficiency of the process increases a lot as the confining stresses decrease. Therefore, the part of the energy used for stress relief in confined conditions is used for the fracturing process.

Then, the issue would be to design an electrical system

capable of generating the pressure wave in a fluid at high pressure. It is expected that under such conditions, the liquid–vapor transition requires more energy and therefore the energy saved for the relief of the confinement stress may serve to generate the electrical discharge. There is a compromise to be sought.

There is one issue, however, which we did not tackle and which seems to be some intrinsic limit of the technique: in the presence of faults and joints, wave propagation is modified. Joints or faults reflect part of the pressure wave (the rest being transmitted) and therefore should act as filters. Such a reflection may decrease the efficiency of the process by decreasing the extent of damage. Obviously, it depends on the precise geometry of the reservoir.

Stimulation of hydrocarbon reservoirs with dynamic loads is still among the potential alternatives to hydraulic fracturing. Research efforts directed at the implementation of blast loads and explosives (which are often used prior to hydraulic fracturing for perforation of the steel casing) are being carried out in China [ZHA 10, HUA 11, ZHU 13], Europe [BAS 12] and in the United States [WHI 14], for instance. It is a lively scientific topic in spite of the modest efficiency reported in this book. Whatever the technique to be implemented in order to generate dynamic loads, we believe that "*in silico*" research efforts are reaching their limits. Even though several optimization directions can be imagined, a pilot phase, *in situ* or in a calibration chamber, is required before scientific research may proceed in directions where maximum efficiency is to be expected. We hope that such a pilot phase will be possible in the future.

Bibliography

[BAR 96] BARY B., Etude du couplage hydraulique – mécanique dans le béton endommagé, PhD Thesis, LMT ENS Cachan, France, 1996.

[BAR 00] BARY B., BOURNAZEL J.P., BOURDAROT E., "Poro-damage approach applied to hydro-mechanical fracture analysis of concrete", *Journal of Engineering Mechanics ASCE*, vol. 126, pp. 937–943, 2000.

[BAS 12] BASTANTE F.G., ALEJANO L., GONZALEZ-CAO J., "Predicting the extent of blast-induced damage in rock masses", *International Journal of Rock Mechanics & Mining Sciences*, vol. 56, pp. 44–53, 2012.

[BAŽ 83] BAŽANT Z.P., OH B., "Crack band theory for fracture of concrete", *Materials and structures, RILEM*, vol. 16, pp. 155– 177, 1983.

[BAŽ 98] BAŽANT Z.P., PLANAS J., *Fracture and Size Effect in Concrete and Other Quasi-Brittle Materials*, CRC Press, p. 616, 1998.

[BAŽ 02] BAŽANT Z.P., JIRASEK M., "Non local integral formulations for plasticity and damage, survey of progress", *Journal of Engineering Mechanics ASCE*, vol. 128, pp. 1119–1149, 2002.

[CAO 01a] CAO J., CHUNG D.D.L, "Defect dynamics and damage of concrete under repeated compression, studied by electrical resistance measurement", *Cement and Concrete Research*, vol. 31, pp. 1639–1642, 2001.

[CAO 01b] CAO J., CHUNG D.D.L., "Minor damage of cement mortar during cyclic compression, monitored by electrical resistivity measurement", *Cement and Concrete Research*, vol. 32, pp. 1656–1662, 2001.

[CAS 04] CASADEI F., POTAPOV S., "Permanent fluid-

structure interaction with non-conforming interfaces in fast transient dynamics", *Computer methods in applied mechanics and engineering*, vol. 193, pp. 4157–4194, 2004.

[CHA 91] CHARLEZ P.A., *Rock Mechanics: Theoretical Fundamentals*, Technip, Paris, p. 360, 1991.

[CHA 05] CHATZIGEORGIOU G., PICANDET V., KHELIDJ A. *et al.*, "Coupling between progressive damage and permeability of concrete: analysis with a discrete model", *International Journal of Numerical and Analytical Methods in Geomechanics*, vol. 29, pp. 1005–1018, 2005.

[CHE 11] CHEN W., MAUREL O., REESS T. *et al.*, "Modelling anisotropic damage and permeability of mortar under dynamic loads", *European Journal of Environmental and Civil Engineering*, vol. 15, pp. 727–742, 2011.

[CHE 12] CHEN W., MAUREL O., REESS T. *et al.*, "Experimental study on an alternative stimulation technique for tight gas reservoirs based on dynamic shock waves generated by pulsed arc electrohydraulic discharges", *Journal of Petroleum Sciences and Engineering*, vol. 88–89, pp. 67–74, 2012.

[CHE 14a] CHEN W., LA BORDERIE C., MAUREL O. *et al.*, "Simulation of damage–permeability coupling for mortar under dynamic loads", *Int. J. Num. Anal. Meths. in Geomechanics*, vol. 38, pp. 457–474, 2014.

[CHE 14b] CHEN W., MAUREL O., REESS T. *et al.*, "Experimental and numerical study of shock wave propagation in water generated by pulsed arc electrohydraulic discharges", *International Journal Heat and Mass transfer*, vol. 50, pp. 673– 684, 2014.

[CHO 04] CHO S.H., KANEKO K., "Influence of the applied pressure waveform on the dynamic fracture process in rock", *International Journal of Rock Mechanics & Mining Sciences*, vol. 41, pp. 771–784, 2004.

[CHO 07] CHOINSKA M., KHELIDJ A., CHATZIGEORGIOU G. *et al.*, "Effects and interactions of

temperature and stress-level related damage on permeability of concrete", *Cement and Concrete Research*, vol. 37, pp. 79–88, 2007.

[CHK 09] CHKIR R., BODIN D., PIJAUDIER-CABOT G. *et al.*, "An inverse analysis approach to determine fatigue performance of bituminous mixes", *Mechanics of time dependent Materials*, vol. 13, pp. 357–373, 2009.

[DEN 02] DENOUAL C., HILD F., "Dynamic fragmentation of brittle solids: a multi-scale model", *European Journal of Mechanics, A/Solids*, vol. 21, pp. 105–120, 2002.

[DES 07] DESMORAT R., GATUINGT F., RAGUENEAU F., "Nonlocal anisotropic damage model and related computational aspects for quasi-brittle materials", *Engineering Fracture Mechanics*, vol. 74, pp. 1539–1560, 2007.

[DIA 00] DIAMOND S., "Mercury porosimetry, an inappropriate method for the measurement of pore size distributions in cement-based materials", *Cement and Concrete Research*, vol. 30, pp. 1517–1525, 2000.

[DUB 96] DUBÉ J.-F., PIJAUDIER-CABOT G., LA BORDERIE C., "A rate dependant damage model for concrete in dynamics", *Journal of Engineering Mechanics ASCE*, vol. 122, pp. 939–947, 1996.

[GAT 02] GATUINGT F., PIJAUDIER-CABOT G., "Coupled damage and plasticity modelling in transient dynamic analysis of concrete", *Int. J. Num. Anal. Meths. in Geomechanics*, vol. 26, pp. 1–24, 2002.

[HUA 11] HUANG B., LIU C., FU J. *et al.*, "Hydraulic fracturing after water pressure controlled blasting for increased fracturing", *International Journal of Rock Mechanics & Mining Sciences*, vol. 48, pp. 976–983, 2011.

[JAS 07] JASON L., PIJAUDIER-CABOT G., GHAVAMIAN S. *et al.*, "Hydraulic behaviour of a representative structural volume for containment buildings", *Nuclear Engineering and Design*, vol. 237, pp. 1259–1274, 2007.

[KHA 15] KHADDOUR F., GREGOIRE D., PIJAUDIER-CABOT G., "Capillary bundle model for the computation of the apparent permeability from pore size distributions", *Eur. J. Env. Civ. Engrg.*, vol. 19, pp. 168–183, 2015.

[KLI 41] KLINKENBERG L.J., "The permeability of porous media to liquids and gases, American Petroleum Institute", *Drilling and Production Practice*, pp. 200–213, 1941.

[LEP 00] LEPAREUX M., Explosions des mélanges de fluides, Cours IPSI, 2000.

[MAD 05] MADHAVAN S., DOIPHODE P.M., CHATUREDI S., "Modeling of shock-wave generation in water by electrical discharges", *IEEE Transactions on Plasma Science*, vol. 28, pp. 1552–1557, 2005.

[MAL 98] MALVAR L.J., ROSS J.E., "Review of the strain rate effect for concrete in tension", *ACI Material Journal*, vol. 95, pp. 735– 739, 1998.

[MAU 10] MAUREL O., REESS T., MATALLAH M. *et al.*, "Electrohydraulic shock wave generation as a mean to increase intrinsic permeability of mortar", *Cement and Concrete Research*, vol. 40, pp. 1631–1638, 2010.

[MAZ 86] MAZARS J., "A description of micro and macroscale damage of concrete structures", *Engineering of Fracture Mechanics*, vol. 25, pp. 729–737, 1986.

[MAZ 90] MAZARS J., BERTHAUD Y., RAMTANI S., "The unilateral behaviour of damaged concrete", *Engineering Fracture Mechanics*, vol. 35, pp. 629–635, 1990.

[MOO 10] MOONEN P., SLUYS L.J., CARMELIET J., "A continuous-discontinuous approach to simulate physical degradation processes in porous media", *Int. J. Num. Met. Engrg.*, vol. 84, pp. 1009–1037, 2010.

[PAP 06] PAPANASTASIOU P., "Hydraulic fracturing", *Revue Européenne de Génie Civil*, vol. 10, pp. 829–848, 2006.

[PIC 01] PICANDET V., KHELIDJ A., BASTIAN G., "Effect of axial compressive damage on gas permeability of ordinary and high-performance concrete", *Cement and Concrete Research*, vol. 31, pp. 1525–1532, 2001.

[PIJ 93] PIJAUDIER-CABOT G., BENALLAL A., "Strain localization and bifurcation in a nonlocal continuum", *International Journal Solids and Structures*, vol. 30, pp. 1761–1775, 1993.

[PIJ 09] PIJAUDIER-CABOT G., DUFOUR F., CHOINSKA M., "Permeability due to the increase of damage in concrete: from diffuse to localised damage distributions", *Journal of Engineering Mechanics ASCE*, vol. 135, pp. 1022–1028, 2009.

[REY XX] REY-BETHBEDER A., JACQUES J., MARTIN A.S. *et al.*, Electrical Reservoir Fracturing, Int. Pub. Number: WO2012/123458 A2, F.

[REY XX] REY-BETHBEDER A., JACQUES J., MARTIN A.S. *et al.*, Electrical and Static Fracturing of a Reservoir, Int. Pub. Number: WO2012/123461 A2, F.

[ROB 03] ROBBE M.F., LEPAREUX M., CARIOU Y., "Numerical interpretation of the MARA 8 experiment simulating a hypothetical core disruptive accident", *Nuclear Engineering and Design*, vol. 220, pp. 119–158, 2003.

[ROB 04] ROBBE M.F., CASADEI F., "Comparison of various models for the simulation of a core disruptive accident in the MARA 10 mock-up", *Nuclear Engineering and Design*, vol. 232, pp. 301– 326, 2004.

[ROB 05] ROBBE M.F., LEPAREUX M., SEINTURIER E., "Computation of a core disruptive accident in the MARS mock-up", *Nuclear Engineering and Design*, vol. 235, pp. 1403–1440, 2005.

[SAN 07] SANCHIDRIAN J., SEGARRA P., LOPEZ L., "Energy components in rock blasting", *International Journal of Rock Mechanics & Mining Sciences*, vol. 44, pp. 130–147, 2007.

[SCH 02] SCHREFFLER B., KHOURY G.A., GAWIN D. *et al.*, "Thermo-hydro-mechanical modelling of high performance concrete at high temperatures", *Engineering Computations*, vol. 19, pp. 787–819, 2002.

[TOU 06] TOUYA G., REESS T., PÉCASTAING L. *et al.*, "Development of subsonic electrical discharges in water and measurements of the associated pressure waves", *Journal of Physics: Applied Physics*, vol. 39, pp. 5236–5244, 2006.

[WAN 09] WANG Z.L., KONIETZKY H., "Modelling of blast-induced fractures in jointed rock masses", *Engineering Fracture Mechanics*, vol. 76, pp. 1945–1955, 2009.

[WHI 14] WHITE B.W., VOROBIEV O.Y., WALSH S.D.C., "Modeling dynamics stimulation of geological resources", *48th US Rock Mechanics/Geomechanics Symposium*, Minneapolis, p. 7129, American Rock Mechanics Association, June 2014.

[YUA 04] YUAN S.C., HARRISON J., "Numerical modelling of progressive damage and associated fluid flow using a hydro-mechanical local degradation approach", *International Journal of Rock Mechanics & Mining Sciences*, vol. 41, pp. 1–6, 2004.

[ZHA 10] ZHANG G.Q., CHEN M., "Dynamic fracture propagation in hydraulic re-fracturing", *J. Petrol. Sci. Eng.*, vol. 70, pp. 266– 272, 2010.

[ZHU 13] ZHU W.C., WEI C.H., LI S. *et al.*, "Numerical modeling on distress blasting in coal seam for enhancing gas drainage", *International Journal of Rock Mechanics & Mining Sciences*, vol. 59, pp. 179–190, 2013.

Index

A, B, C, D

E, F

G, H, I, K

L, M, N

O, P, R

S, V, W, X

Other titles from

in

Civil Engineering and Environmental Geomechanics

2015

AÏT-MOKHTAR Abdelkarim, MILLET Olivier

Structure Design and Degradation Mechanisms in Coastal Environments

MONNET Jacques

In Situ Tests in Geotechnical Engineering

2014

DAÏAN Jean-François

Equilibrium and Transfer in Porous Media – 3-volume series

Equilibrium States – Volume 1

Transfer Laws – Volume 2

Applications, Isothermal Transport, Coupled Transfers – Volume 3

2013

AMZIANE Sofiane, ARNAUD Laurent

Bio-aggregate-based Building Materials: Applications to Hemp Concretes

BONELLI Stéphane

Erosion in Geomechanics Applied to Dams and Levees

CASANDJIAN Charles, CHALLAMEL Noël, LANOS Christophe,

HELLESLAND Jostein

Reinforced Concrete Beams, Columns and Frames: Mechanics and Design

GUÉGUEN Philippe

Seismic Vulnerability of Structures

HELLESLAND Jostein, CHALLAMEL Noël, CASANDJIAN Charles,

LANOS Christophe

Reinforced Concrete Beams, Columns and Frames: Section and Slender

Member Analysis

LALOUI Lyesse, DI DONNA Alice

Energy Geostructures: Innovation in Underground Engineering

LEGCHENKO Anatoly

Magnetic Resonance Imaging for Groundwater

2012

BONELLI Stéphane

Erosion of Geomaterials

JACOB Bernard *et al.*

ICWIM6 Proceedings of the International Conference on Weigh-In-Motion

OLLIVIER Jean-Pierre, TORRENTI Jean-Marc, CARCASSES Myriam

Physical Properties of Concrete and Concrete Constituents

PIJAUDIER-CABOT Gilles, PEREIRA Jean-Michel

Geomechanics in CO_2 Storage Facilities

2011

BAROTH Julien, BREYSSE Denys, SCHOEFS Franck

Construction Reliability: Safety, Variability and Sustainability

CREMONA Christian

Structural Performance: Probability-based Assessment

HICHER Pierre-Yves

Multiscales Geomechanics: From Soil to Engineering Projects

IONESCU Ioan R. *et al.*

Plasticity of Crystalline Materials: from Dislocations to Continuum

LOUKILI Ahmed

Self Compacting Concrete

MOUTON Yves

Organic Materials for Sustainable Construction

NICOT François, LAMBERT Stéphane

Rockfall Engineering

PENSE-LHERITIER Anne-Marie

Formulation

PIJAUDIER-CABOT Gilles, DUFOUR Frédéric

Damage Mechanics of Cementitious Materials and Structures

RADJAI Farhang, DUBOIS Frédéric

Discrete-element Modeling of Granular Materials

RESPLENDINO Jacques, TOUTLEMONDE François

Designing and Building with UHPFRC

2010

ALSHIBLI A. Khalid

Advances in Computed Tomography for Geomechanics

BUZAUD Eric, IONESCU Ioan R., VOYIADJIS Georges

Materials under Extreme Loadings / Application to Penetration and Impact

LALOUI Lyesse

Mechanics of Unsaturated Geomechanics

NOVA Roberto

Soil Mechanics

SCHREFLER Bernard, DELAGE Pierre

Environmental Geomechanics

TORRENTI Jean-Michel, REYNOUARD Jean-Marie, PIJAUDIER-CABOT Gilles

Mechanical Behavior of Concrete

2009

AURIAULT Jean-Louis, BOUTIN Claude, GEINDREAU Christian

Homogenization of Coupled Phenomena in Heterogenous Media

CAMBOU Bernard, JEAN Michel, RADJAI Fahrang

Micromechanics of Granular Materials

MAZARS Jacky, MILLARD Alain

Dynamic Behavior of Concrete and Seismic Engineering

NICOT François, WAN Richard

Micromechanics of Failure in Granular Geomechanics

2008

BETBEDER-MATIBET Jacques

Seismic Engineering

CAZACU Oana

Multiscale Modeling of Heterogenous Materials

HICHER Pierre-Yves, SHAO Jian-Fu

Soil and Rock Elastoplasticity

JACOB Bernard *et al.*

HVTT 10

JACOB Bernard *et al.*

ICWIM 5

SHAO Jian-Fu, BURLION Nicolas

GeoProc2008

2006

DESRUES Jacques *et al.*

Advances in X-ray Tomography for Geomaterials

FSTT

Microtunneling and Horizontal Drilling

MOUTON Yves

Organic Materials in Civil Engineering

2005

PIJAUDIER-CABOT Gilles *et al.*

Creep Shrinkage and Durability of Concrete and Concrete Structures

CONCREEP – 7

WILEY END USER LICENSE AGREEMENT

Go to www.wiley.com/go/eula to access Wiley's ebook EULA.